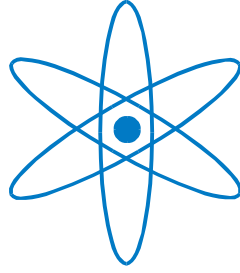# PHYSIK-DEPARTMENT

Decay properties of nuclei close to $Z = 108$ and
$N = 162$

Dissertation
von

Jan Dvořák

TECHNISCHE UNIVERSITÄT
MÜNCHEN

Fakultät für Physik der Technischen Universität München

Physik Department E12

Decay properties of nuclei close to $Z = 108$ and $N = 162$

Jan Dvořák

Vollständiger Abdruck der von der Fakultät für Physik
der Technischen Universität München zur Erlangung des akademischen Grades eines

Doktors der Naturwissenschaften (Dr. rer. nat.)

genehmigten Dissertation.

Vorsitzender:	Univ.-Prof. Dr. M. Ratz
Prüfer der Dissertation:	
	1. Univ.-Prof. Dr. R. Krücken
	2. Univ.-Prof. Dr. A. Türler

Die Dissertation wurde am 02.07.2007 bei der Technischen Universität München eingereicht
und durch die Fakultät für Physik am 12.07.2007 angenommen.

Abstract

The goal of the research conducted in the frame of this thesis was to investigate the decay properties of the nuclides $^{269-271}$Hs and their daughters using an improved chemical separation and detection system.

Shell stabilization was predicted in the region around $Z = 108$ and $N = 162$ in calculations, taking into account possible higher orders of deformations of the nuclei. The nucleus ^{270}Hs with a closed proton and a closed neutron deformed shell, was predicted to be "deformed doubly magic". Nuclei around ^{270}Hs can be produced only via fusion reactions at picobarn levels, resulting in a production rates of few atoms per day. Investigating short-lived nuclei using rapid chemical separation and subsequent on-line detection methods provides an independent and alternative means to electromagnetic on-line separators. Chemical separation of Hs in the form of HsO_4 provides an excellent tool to study the formation reactions and nuclear structure in this region of the chart of nuclides due to a high overall efficiency and a very high purification factor.

The goal was accomplished, as element 108, hassium, was produced in the reaction ^{248}Cm(^{26}Mg, xn)$^{274-x}$Hs and chemically isolated. After gas phase separation of HsO_4, 26 genetically linked decay chains have been observed. These were attributed to decays of three different Hs isotopes produced in the 3–5n evaporation channels. The known decay chain of ^{269}Hs, the 5n evaporation product, serves as an anchor point, thus allowing the unambiguous assignment of the observed decay chains to the 5n, 4n, and 3n channels, respectively.

Decay properties of five nuclei have been unambiguously established for the first time, including the one for the the doubly-magic nuclide ^{270}Hs. This hassium isotope is the next doubly magic nucleus after the well known ^{208}Pb and the first experimentally observed even-even nucleus on the predicted $N = 162$ neutron shell. The observed decay properties provide strong indications for enhanced nuclear stability in this area of the heaviest known elements and provide an important reference point for theoretical models.

The measurement of the production cross sections at five beam energies allowed the evaluation of excitation functions for the 3–5n evaporation channels at the few picobarn level. Experimental data indicate a surprising cross section enhancement at sub-barrier energies due to the deformation of the target nucleus. This opens prospects for the search for the 3n evaporation channel products in nuclear reactions with actinide targets, induced with light neutron rich projectiles.

Zusammenfassung

Das Ziel der Forschungsarbeit, die im Rahmen dieser Dissertation durchgeführt wurde, war es die Zerfallseigenschaften der Nuklide $^{269-271}$Hs und ihrer Töchter, mittels eines verbesserten chemischen Separations- und Nachweissystems, zu untersuchen.

Berechnungen sagen eine Schalenstabilisierung für die Region um $Z = 108$ und $N = 162$, unter Berücksichtigung möglicher Kerndeformationen höherer Ordnungen, voraus. Der Kern ^{270}Hs, mit abgeschlossenen Protonen und Neutronen Schalen, wurde als deformiert doppelt magisch vorhergesagt. Kerne um ^{270}Hs können nur mittels Fusionsreaktionen im picobarn Bereich erzeugt werden, was Produktionsraten von wenigen Atomen pro Tag zur Folge hat. Die Erforschung kurzlebiger Kerne mittels schneller chemischer Separation und anschließender on-line Detektionsmethode bietet eine unabhängige und alternative Möglichkeit zu elektromagnetischen on-line Separatoren. Die chemische Separation von Hs in Form von HsO_4 stellt, wegen ihrer hohen Gesamteffizienz und ihres sehr hohen Reinheitsgrades, ein exzellentes Werkzeug dar, Entstehungsmechanismen und Kernstruktur in dieser Region der Nuklidkarte zu studieren.

Das Ziel wurde erreicht da Element 108, Hassium, in der Reaktion ^{248}Cm(^{26}Mg, xn)$^{274-x}$Hs produziert und chemisch isoliert wurde. Nach der Separation von HsO_4 in der Gasphase wurden 26 genetisch verbundene Zerfallsketten beobachtet. Diese wurden dem Zerfall drei verschiedener Hs Isotope zugeordnet, welche aus den 3–5n Verdampfungskanälen hervorgingen. Die bekannte Zerfallskette von ^{269}Hs, dem 5n Verdampfungsprodukt, dient als Fixpunkt und erlaubt folglich die eindeutige Zuordnung der beobachteten Zerfallsketten zu den 5n, 4n und 3n Kanälen.

Zerfallseigenschaften von fünf Kernen wurden zum ersten Mal eindeutig festgestellt, insbesondere jene des doppelt magischen Nuklids ^{270}Hs. Dieses Hassium Isotop ist der nächste doppelt magische Kern nach dem bekannten ^{208}Pb und der erste experimentell beobachtete gerade-gerade Kern auf der vorhergesagten $N = 162$ Neutronenschale. Die beobachteten Zerfallseigenschaften liefern deutliche Hinweise auf eine erhöhte Kernstabilität in dieser Region der schwersten bekannten Elemente und einen wichtigen Referenzpunkt für theoretische Modelle.

Messungen der Produktionswirkungsquerschnitte bei fünf Bestrahlungsenergien erlaubten die Ermittlung von Anregungsfunktionen für die 3–5n Verdampfungskanäle im Bereich weniger picobarn. Die experimentellen Daten weisen auf eine überraschende Erhöhung des Wirkungsquerschnitts bei Energien unterhalb der Barriere hin, was auf die Deformation des Targetkerns zurückzuführen ist. Dies eröffnet neue Perspektiven für die Suche nach Produkten im 3n Verdampfungskanal in Kernreaktionen von leichten neutronenreichen Projektilen mit Aktinoiden Targets.

Acknowledgements

This thesis arose from the research conducted at the Institut für Radiochemie at TU München from May 2004 until June 2007 under the kind guidance of Prof. Dr. A. Türler and Prof. Dr. R. Krücken.

I am grateful to many people for help, both direct and indirect, in writing this thesis. I owe a great deal to colleagues, friends and members of my family who have helped me and who, through their own research, comments and questions have encouraged, supported and enlightened me.

First and foremost I offer my sincerest gratitude to my mentor, Dr. A. Yakushev. Without him this thesis would never come into existence. He made us (me and my wife Zuzana) an offer to come to München and took the full responsibility for us. During the years of our stay here he became like my second father - always ready to help, patiently answering my rudimentary questions, supporting me in every possible way. He taught me everything I know about "superheavies", passing a small part of his huge know-how to me. His truly scientist intuition has made him a constant oasis of ideas, which exceptionally inspire and enrich my growth as a researcher, as a scientist, and as a human being. I am indebted to him more that he knows.

I gratefully acknowledge Prof. A. Türler for his confidence to allow an unexperienced student to participate in such an important and exciting research project. His firm support helped me to make the first steps towards writing this thesis, as well as to make the last, the most important step. I deeply appreciate his kind cordiality, which allowed us to enjoy many interesting friendly discussions. One simply could not wish for a better and friendlier supervisor.

Prof. R. Krücken invaluably helped me with advices, which every time proved to be absolutely correct. I am much indebted for his responses to my needs, which came

x

Contents

"The strongest arguments prove nothing so long as the conclusions are not verified by experience. Experimental science is the queen of sciences and the goal of all speculation."

— Roger Bacon (1214–94)

Chapter 1

Introduction

"Essentially, all models are wrong, but some are useful."
      — George E. P. Box (1919 – present)

1.1   Motivation

The heaviest known element that occurs in macroscopic quantities in nature is uranium, element 92. This is the last element whose lifetime is comparable with the age of the earth. Elements beyond uranium are all man-made, the result of transmutation. Their nuclear properties make them especially important for mankind. In the 65 years following the discovery of the first transuranium elements, neptunium and plutonium, scientists synthesized and identified 24 new elements ($Z = 93 - 116, 118$). Due to relativistic velocities of electrons in heaviest atoms, their chemical properties often differ from those of their lighter homologs. Hence, the investigation of the chemical properties of the heaviest elements is an extremely interesting task for nuclear chemistry.

For a long time it was believed, that the practical limit to the periodic table would be reached at about element 108 (Figure 1.1). Short spontaneous fission (SF) half-lives expected for nuclei with $Z \geq 108$ would prohibit their identification. However, a number of theoretical calculations made between 1966 and 1972 have predicted a stabilization against spontaneous fission in the region of elements with proton number $Z = 114$ and neutron number $N = 184$. This stabilization is due to the complete filling of proton and
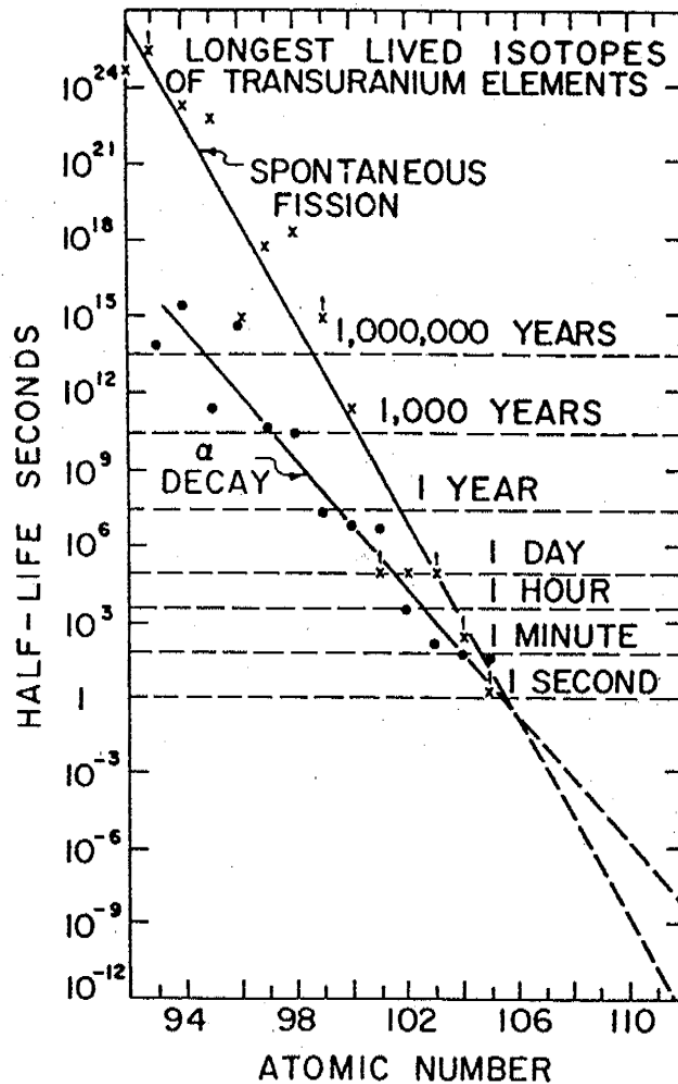
Figure 1.1: The half-life of the longest-lived isotope of a given element plotted against atomic number, as known in 1970. Adapted from [1].

neutron shells. The "superheavy" elements (SHE) were predicted to form an "Island of Stability" separated from the land of known nuclei by the "Sea of Instability". A worldwide effort was launched to reach this island, but it has proved to be a difficult task.

The definition of shell stabilized SHE was later expanded to all elements with $Z \geq 104$, as another shell appeared in the region around $Z = 108$ and $N = 162$ in calculations, which took into account possible deformation of nuclei. The nucleus ^{270}Hs was predicted to be "deformed doubly magic". This nuclide has not been unambiguously identified so far, only tentative evidence was reported [2,3]. The experimental observation of this

nuclide was the main goal of this research project. Confirmation of enhanced stability of this nucleus would prove the hypothesis of its magicity and give an important reference point for theoretical calculations.

1.2 Stability of SHE

As SHE are not present in nature, they have to be produced artificially at particle accelerators. Their stability essentially affects the possibility of their identification. Due to their large number of protons, SHE should have a very low nuclear stability against SF and also against α-decay. Most beta stable nuclei are characterized by a binding energy per nucleon of $\sim$ 7–8 MeV/A and an approximately constant density of ~ 0.17 nucleons/fm^3 [1]. The nucleons are held together by the strong nuclear force, but protons repel each other by the Coulomb force. Nuclei have a positive electric charge and to good approximation they can be treated as with finite size (thus having a surface).

1.2.1 Liquid drop model

The liquid-drop model (LDM) is a semi-classical model for estimating the mass of a nucleus. The main analogies between a nucleus and a liquid drop are the well-defined surface, incompressibility and attractive short-range force, holding the nucleons (molecules) together. In addition, protons in the nucleus interact via the Coulomb repulsion. Based on this model, a semiempirical formula for the calculation of the mass M of a nucleus was developed by Weizsäcker [4]. Later it was simplified by Bethe and Bacher [5] to the form known as "semi-empirical mass formula" (SEMF):

$$M = NM_n + ZM_p - \alpha A + \frac{\beta(N-Z)^2}{A} + \gamma A^{\frac{2}{3}} + \frac{3}{5}\frac{e^2}{4\pi\varepsilon_0 r_0}\frac{Z^2}{A^{\frac{1}{3}}} + \delta \ , \qquad (1.1)$$

where N, Z and A are the neutron, proton and mass number, respectively, r_0 is the radius factor ($r_0 = 1.2$ fm) and the constants α, β and γ are determined empirically. The first two terms in the SEMF represent the mass of the protons and neutrons. The third term is the "volume" term resulting from the increase in binding energy from the attractive force among all nucleons. The fourth term reflects the increased stability of nuclei with approximately equal numbers of protons and neutrons. The fifth term corrects for the loss of binding energy by surface nucleons. The sixth term represents

the Coulomb energy of the nucleus. The last term δ stands for the quantum mechanical pairing energy [6, 7] and is equal to:

$$\delta = \begin{cases} 0.036A^{-\frac{3}{4}} & \text{for even-odd nuclei,} \\ 0 & \text{for odd A nuclei,} \\ -0.036A^{-\frac{3}{4}} & \text{for even-even nuclei.} \end{cases} \tag{1.2}$$

In equation (1.1) nuclei are treated as spherical. For deformed nuclei, the Coulomb energy term and the pairing energy term vary with deformation.
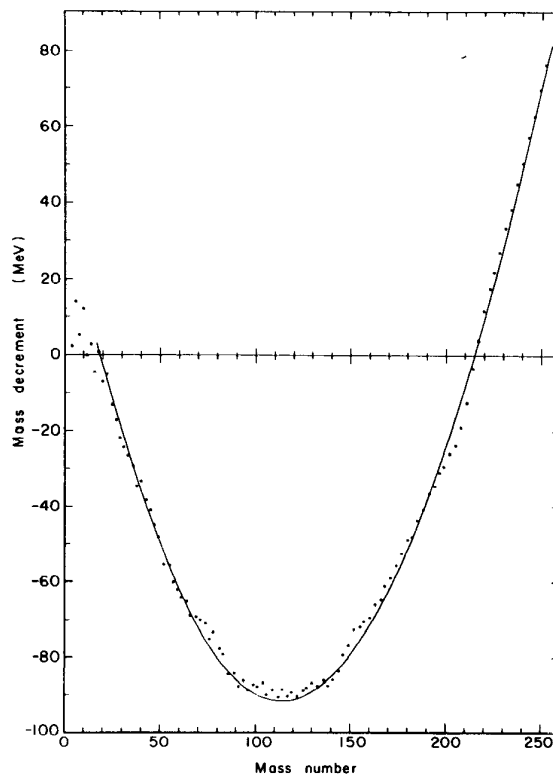
Figure 1.2: Comparison of liquid-drop model mass predictions with experimental data for beta-stable nuclei. The masses are plotted as a mass decrement in MeV. The deviations from the LDM are mostly due to shell effects. Adapted from [8].

1.2.2   Magic numbers

The general agreement of LDM results with experimental ground state masses is good (Figure 1.2). However, close inspection reveals, that the deviations from the predictions are not random, but follow definite trends (Figure 1.3). We observe an extra stability for nucleon numbers 2, 8, 20, 28, 50, 82 and 126, the so called magic numbers [7]. The special nuclear stability of nuclei with a magic number of protons or neutrons was later explained by the nuclear shell model.
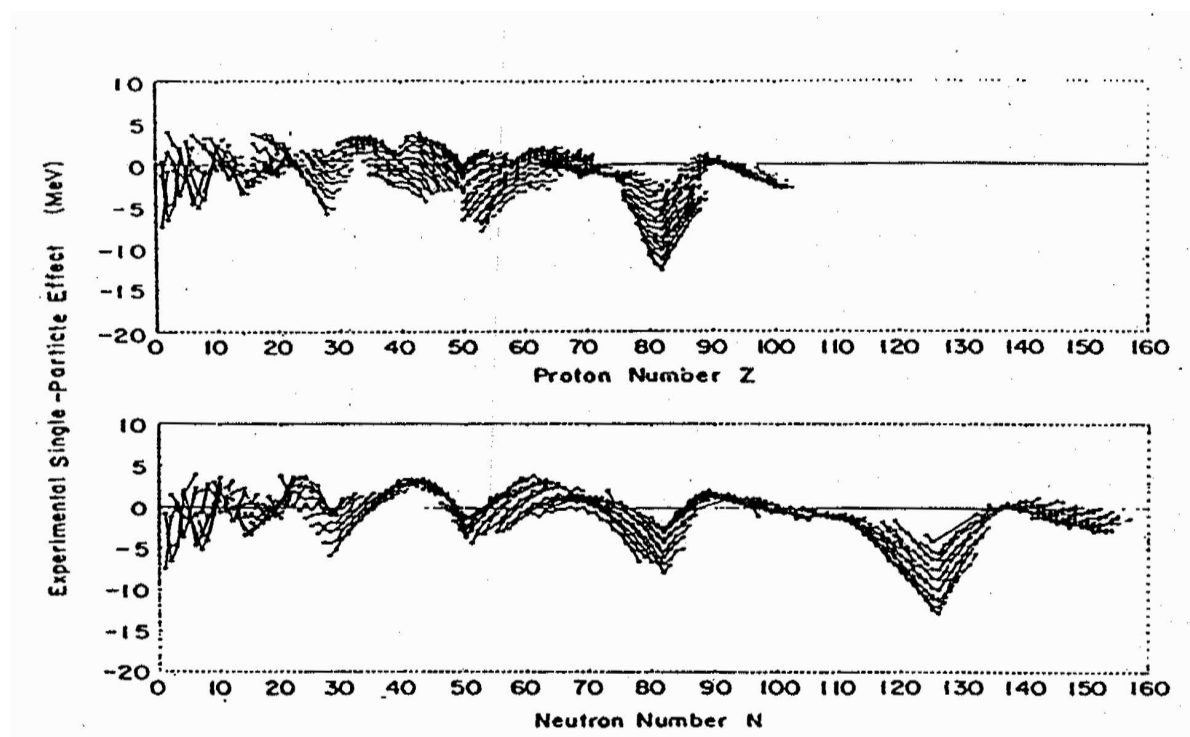
Figure 1.3: Difference in MeV between the experimental ground state mass and the mass given by a liquid drop semiempirical mass equation, uncorrected for shells. Note the extra stabilization energy at nucleon numbers 28, 50, 82, 126, mostly because of nuclear shell effects. Adapted from [9].

1.2.3   Nuclear shell model

In this model the nucleons are treated individually, in contrast to treating the nucleus as a whole in the LDM. The motion of each nucleon is governed by the average attractive force of all the other nucleons in this model. If two nucleons would collide, the energy required to excite one of them to a higher-lying orbit would be more than the nucleons are

likely to transfer. Therefore, it is assumed that there are no nucleon-nucleon collisions in the nucleus, and each nucleon moves in an unperturbed single particle orbit within the nucleus. Mayer [10, 11] explained the magic numbers by calculating the energies of "single particle spectra" using a square and harmonic-oscillator potential well. Energy levels resulting from the calculation with the harmonic-oscillator potential are presented in Figure 1.4. In order to reproduce the correct higher magic numbers, Mayer [12] and Haxel, Jensen and Suess [13] proposed independently that a spin-orbit interaction should be added to the centrally symmetric potential.

The magnitude of splitting increases with increasing angular momentum quantum number l, resulting in large energy gaps free of any particle states. Once all the levels below a major gap are occupied, the nucleus contains a filled shell comparable to the electronic shells known in chemistry. Addition of another particle would result in a substantial increase in total energy.

Although a filled shell clearly results in increased stability, the nuclei *near* closed shells exhibit enhanced stability as well. This is evident in Figure 1.3. Thus, shell gaps are not a sufficient explanation of the phenomenon.

1.2.4   Strutinski nuclear shell corrections

Strutinsky [14, 15] proposed a method to calculate the "shell corrections" (and also corrections for nuclear pairing) to the LDM. The shell correction energy is calculated using the density of single-particle states, from the Nilsson model for deformed nuclei [16].

Nilsson used the modified harmonic-oscillator potential for the investigation of the effect of deformation on the single-particle orbits. A schematic representation showing single-particle energy levels against deformation, also known as a Nilsson diagram, is shown in Figure 1.5. In the diagram, the areas of low density where few Nilsson states exist are visible not only at zero-deformation, but also at some other deformations. The total mass of the nucleus is given as an integral in energy over the occupied states. The Nilsson diagram of energy levels of the more realistic folded-Yukawa single-particle potential for nuclei close to ^{270}Hs reveals gaps at $Z = 108$ and $N = 162$ at non-zero deformation (see Figure 1.6), implying enhanced stability of this deformed nucleus.

The Strutinsky approach is also called a macroscopic-microscopic calculation, as the total energy E of a nucleus is the sum of two terms: the liquid drop model energy E_{LDM} (macroscopic part) and the shell (δS) and pairing (δP) corrections to this energy

Figure 1.4: Energy levels in a modified oscillator potential. The levels on the left are those for the harmonic-oscillator potential. These are split by the l^2 term to produce the second set of levels, and then again by the spin-orbit term to produce the experimentally observed shell gaps in the levels on the right.

(microscopic part):

$$E = \underbrace{E_{\text{LDM}}}_{\text{Macroscopic}} + \underbrace{\sum_{p,n}(\delta S + \delta P)}_{\text{Microscopic}} \qquad (1.3)$$

The shell correction energy tends to lower the ground state mass of nuclei with magic or near-magic numbers of neutrons and protons and thus reducing the discrepancy between calculated and experimental masses in Figure 1.3.

Figure 1.5: Energy levels of a harmonic-oscillator potential for prolate spheroidal deformations. The low density locations are present also at nonzero deformations, suggesting existence of stabilized deformed nuclei. Adapted from [17, 18].

1.2.5   SHE region

The description of the ability to undergo nuclear fission is closely related to the calculation of the masses of nuclei. The liquid-drop model of fission of heavy nuclei, which appeared immediately after the discovery of this phenomenon, predicted a rapid fall in the fission barrier height B_f with increasing fissility parameter Z^2/A [6]. This would
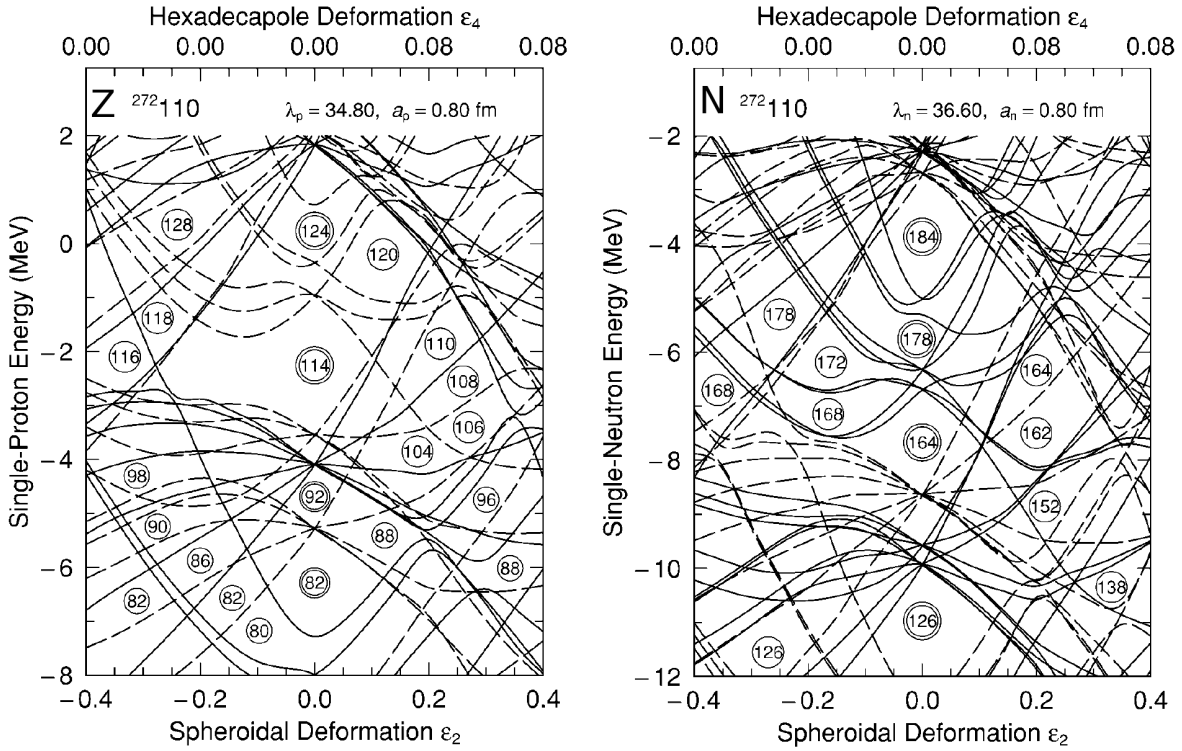
Figure 1.6: Proton and neutron folded-Yukawa single-particle level diagram for the nucleus ^{272}Ds plotted versus spheroidal and hexadecapole deformation. Gaps at $Z = 108$ and $N = 162$ suggest increased stability of deformed ^{270}Hs. Adapted from [19].

result in a decrease of the spontaneous fission half-lives below 1 second close to $Z = 100$. However, experimentally measured half-lives are up to fifteen orders of magnitude longer than those expected based on a simple smooth droplet-like potential energy surface (Figure 1.7). The lengthening of the spontaneous fission half-lives is due to shell effects. The microscopic theory of the nucleus showed, that closed shells of protons and neutrons stabilize nuclei beyond the limits defined by the LDM. Hence, SHE exist solely because of enhanced nuclear stability due to shell effects.

Theoretical predictions located the center of stability in this region close to the nucleus with $Z = 114$ and $N = 184$ [21, 22]. However, different locations of the shell closure were obtained from other approaches [23, 24]. For spherical nuclei the predicted shell closures are at $Z = 114, 120$ or 126 (dashed lines in Figure 1.8) and $N = 171, 184$. SHE were predicted to form an "island" of relative stability surrounded by nuclei with very short half-lives.

The knowledge of ground-state binding energies, however, is not sufficient for the
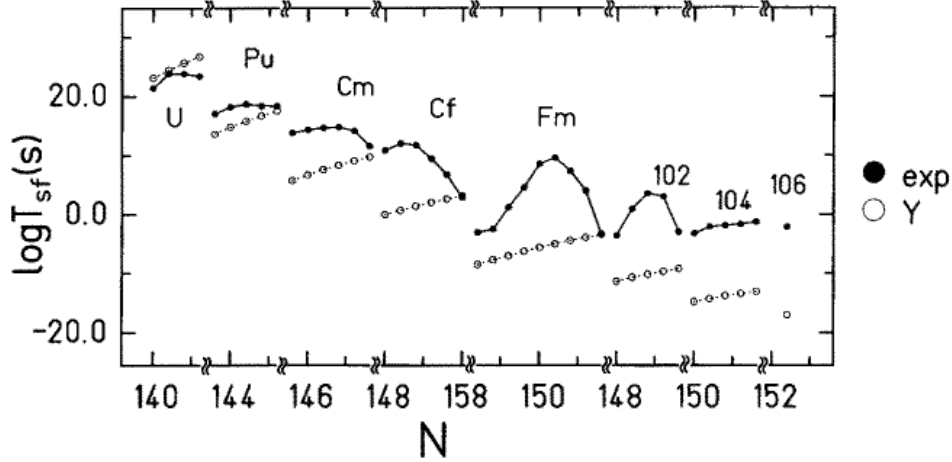
Figure 1.7: Comparison of the measured spontaneous fission half lives for even-even nuclei with those expected in a simple droplet model approach. Adapted from [20].

calculation of partial SF half-lives. It is necessary to determine the shape of the fission barrier over a wide range of deformation. The landscape of fission half-lives reflects the landscape of shell-correction energies in the region of SHE. A significant increase of the SF half-life from 10^3 s for deformed nuclei to 10^{12} s for spherical SHE was calculated, see Figure 1.8. This difference originates from an increased width of the fission barrier, which becomes wider in the case of spherical nuclei.

Partial α-decay half-lives at $N = 184$ decrease almost monotonically from 10^{12} s near $Z = 114$ down to 10^{-9} s near $Z = 126$, see Figure 1.8b. The valley of β-stable nuclei passes through $Z = 114, N = 184$. At a distance of about 20 neutrons away from the bottom of this valley, β-decay half-lives have dropped down to one second [27]. Partial α-decay and β-decay half-lives are only slightly modified by shell effects, as their decay process occurs between neighboring nuclei.

1.2.6 Stability around $Z = 108$ and $N = 162$

Sobiczewski improved those calculations, including higher orders of deformation [20, 28, 29]. These advanced calculations suggested the ground state shell correction energy of deformed nuclei around $Z = 108$ and $N = 162$ to reach values as large as in the case of ^{298}114. The calculated shell correction energies show almost equally deep minima in both cases (Figure 1.9). The deformed shell closure at ^{270}Hs substantially influences
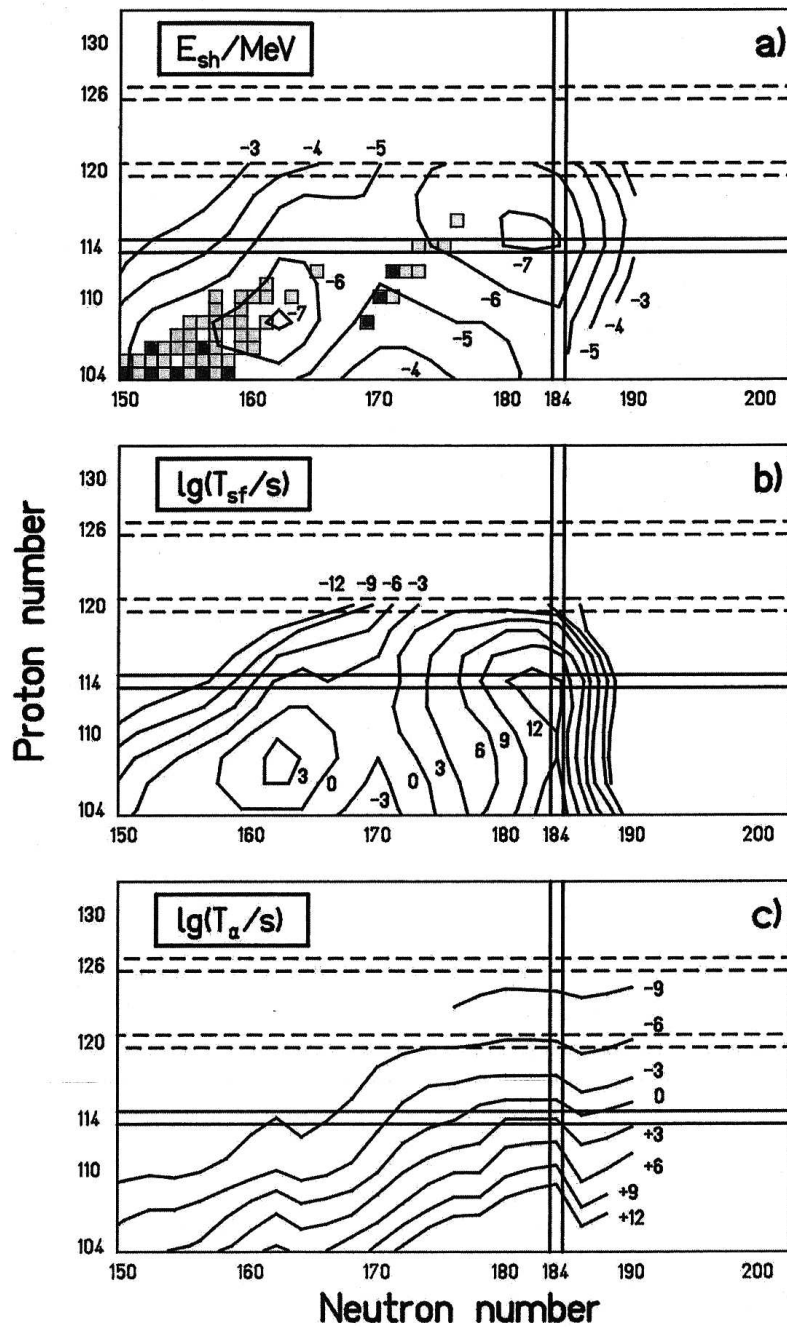
Figure 1.8: Shell-correction energy (a) and partial half-lives for SF (b) and α decay (c). Figure adapted from [25], using data from Reference [26].

the stability of nuclei in the region of SHE. Although other predictions exist, which are placing the neutron shell closure at $N = 164$ [30], calculations including the shell closure at $N = 162$ exhibit better agreement with experimentally measured data.
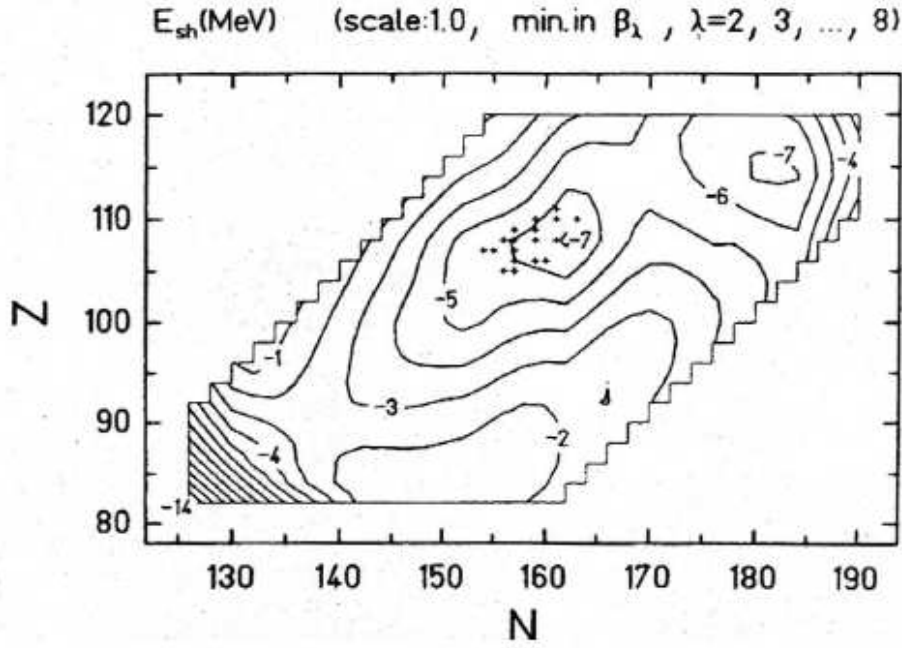
Figure 1.9: Shell correction energies in MeV for nuclei beyond ^{208}Pb. Plus signs represent nuclei known in 1998. Note the nearly equally deep minima close to $^{298}114$ and ^{270}Hs. Adapted from [31].

The stabilization effect is also reflected by lower α-decay energies (Q_α) near and at closed shells, because partial α-decay half-lives show a dependence on Q_α values. The relation of T_α on Q_α can be evaluated using the phenomenological Viola-Seaborg formula, modified by Parkhomenko and Sobiczewski [32]. The partial α-decay half-life is calculated as:

$$\log_{10} T_\alpha^{ph}(Z, N) = aZ(Q_\alpha - \bar{E}_i)^{1/2} + bZ + c, \tag{1.4}$$

where Z is the proton number, a, b, c are parameters adjusted to the experimental data and the parameter $\bar{E}_i$ varies for different nuclei:

$$\bar{E}_i = \begin{cases} 0 & \text{for even-even nuclei,} \\ \bar{E}_p & \text{for even-odd nuclei,} \\ \bar{E}_p + \bar{E}_n & \text{for odd-odd nuclei,} \end{cases} \qquad (1.5)$$

$$a = 1.5372, \qquad b = -0.1607, \qquad c = -36.573$$
$$\bar{E}_p = 0.113 \text{ MeV}, \qquad \bar{E}_n = 0.171 \text{ MeV} \qquad (1.6)$$

The parameters $\bar{E}_p$ and $\bar{E}_n$ correspond to the average excitation energy of proton and neutron one-quasiparticle states to which the α-decay goes, respectively. The above parameters were adjusted fitting the formula to experimentally obtained data. The final values of the parameter set (equation (1.6)) allows one to describe measured values of T_α using the formula 1.4 within a factor of four (within factor of two for even-even nuclei).

In Figure 1.10 calculated Q_α-values of even-even nuclei [33, 34] are plotted along with experimentally measured values [35, 36, 37] for nuclei close to ^{270}Hs. The shell closure at the $N = 162$ neutron shell leads to a stabilization and hence to a local minimum at $N = 162$. The shell closure at the $Z = 108$ proton shell is reflected by the a large difference in Q_α values between Ds and Hs isotones.

The dominating partial half-life can be obtained from the combination of results from individual decay modes as shown in Figure 1.11 for even-even nuclei. The two regions, the region of deformed nuclei near ^{270}Hs and the region of spherical SHE, form a landscape of α-emitters surrounded by spontaneously fissioning nuclei.

From the decay scenario in Figure 1.11 can be derived, that the most likely decay mode of ^{270}Hs is α-decay with a half-life of few seconds (42 s [38], 70 s [39] or 170 s [19]). Both even-even Hs isotopes neighboring ^{270}Hs, ^{268}Hs and ^{272}Hs are expected to decay by α-particle emission with half-lives shorter than one second. A significantly longer half-live of ^{270}Hs compared to its neighbors results from the stabilization at the $N = 162$ nuclear shell and the experimental measurement of such differences would give strong evidence for the location of the shell closure. In the case of the even-even isotope ^{266}Sg the decay via SF is more probable than α-decay, while ^{262}Rf is expected to undergo SF.

For even-odd nuclides, a similar calculation of the expected dominant decay mode
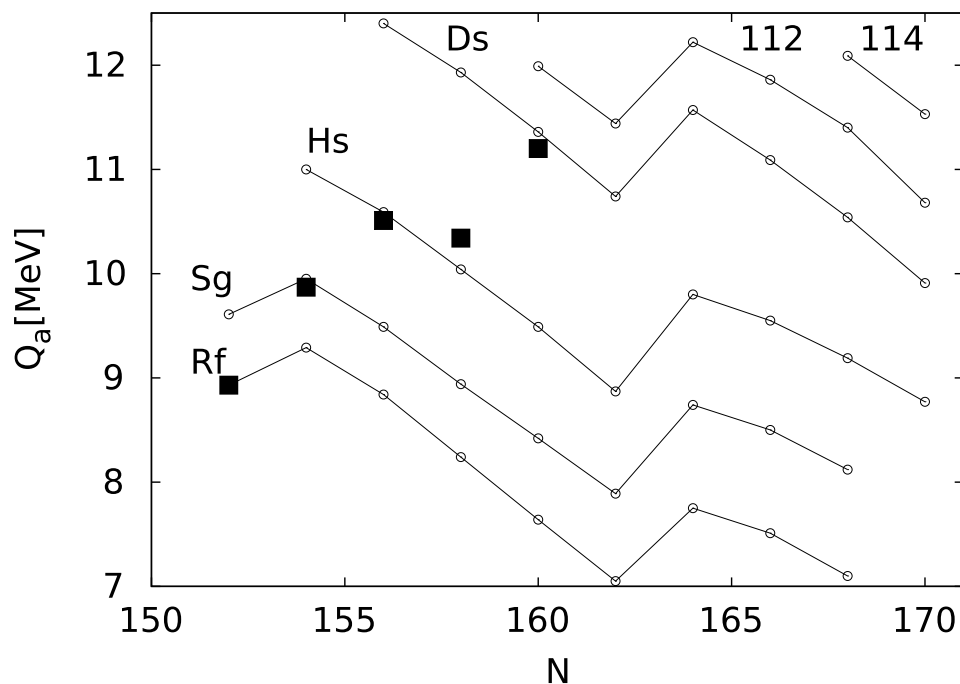
Figure 1.10: Comparison of Q_α values from theoretical calculations [33, 34] and experimental data [35, 36, 37] for even-even nuclei.
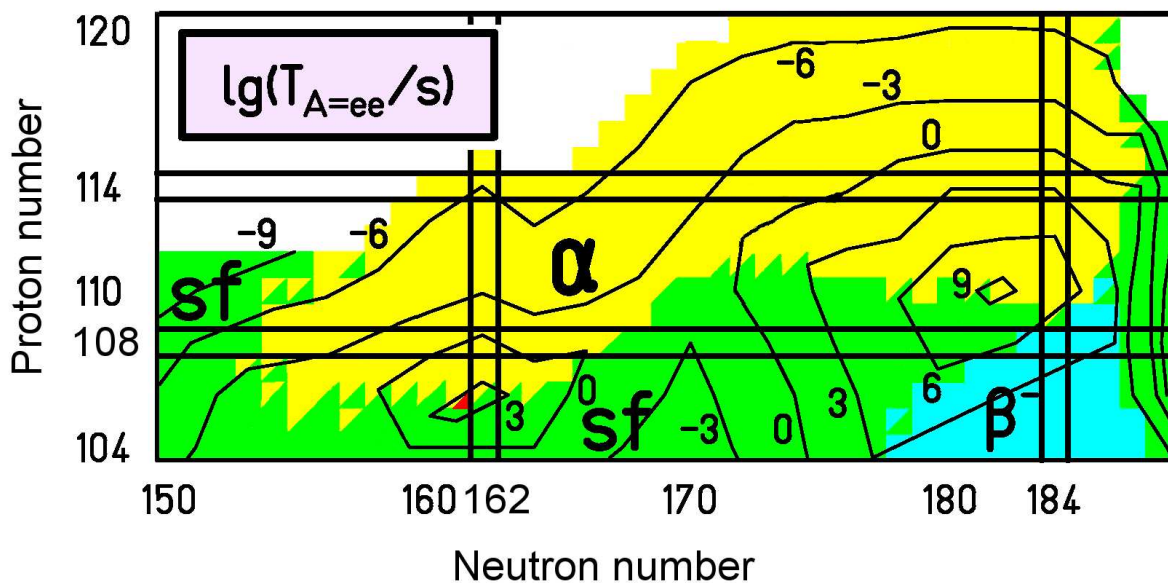
Figure 1.11: Decay scenario in the region of SHE for even-even nuclei. Data from [26].

can be done. The Hs isotopes ^{269}Hs and ^{271}Hs are expected to decay via α-decay, the even-odd Sg daughter isotopes (^{265}Sg and ^{267}Sg) are likely to decay via α-decay. For

^{261,263}Rf, there will be an about equal α/SF branching, since partial half-lives for α-decay and SF are comparable for these isotopes.

Summarizing the known decay properties of ^{269}Hs and the expected decay properties of ^{268}Hs, ^{270}Hs, and ^{271}Hs and their daughters, cascades of subsequent decays are the expected patterns. For ^{269}Hs, α-α-α-α or α-α-SF cascades are known from previous experiments [2, 3, 40, 41]. For decay of ^{268}Hs, ^{270}Hs, and ^{271}Hs, α-α-SF or α-SF decay chains can be expected.

1.3 Production of SHE in nuclear fusion reactions

1.3.1 Fusion mechanism

As SHE have not been found in nature, they have to be synthesized artificially in nuclear fusion reactions at suitable particle accelerators. The most important reaction for the creation of SHE is complete fusion followed by sequential evaporation of one or several neutrons. The target and the projectile nuclei form a compound nucleus (CN) in an excited state, which is highly unstable and undergoes spontaneous fission, unless it de-excites rapidly by emission of neutrons and γ-rays. Evaporation of every neutron competes with SF, which makes the survival probability extremely sensitive on the fission barrier. The process of the fusion reaction leading to the creation of a SHE is schematically shown in Figure 1.12.

Because of the repulsive Coulomb force between the target and the projectile nuclei, the projectile has to have an energy higher than the fusion barrier. This, however, increases the excitation energy of the CN. If the incident projectile nucleus interacts with the target nucleus at large impact parameters, the incident projectile is reflected, corresponding to elastic scattering (Figure 1.12a). The fusion probability is determined by the ratio of surface tension versus Coulomb repulsion, which strongly depends on the asymmetry of the reaction partners (the product $Z_1 \times Z_2$ at fixed $Z_1 + Z_2$). The important factor in the next stage is the impact parameter, which describes the centrality of the collision. With increasing impact factor (not-central collisions), the angular momentum increases to the point, where the nucleus is re-separated by centrifugal forces (Figure 1.12b). In case of central or nearly central collision the CN is formed, but in a highly excited state. As the fission barrier is lower than the excitation energy, the newly created excited CN undergoes fission within 10^{-20} s, unless the excitation energy
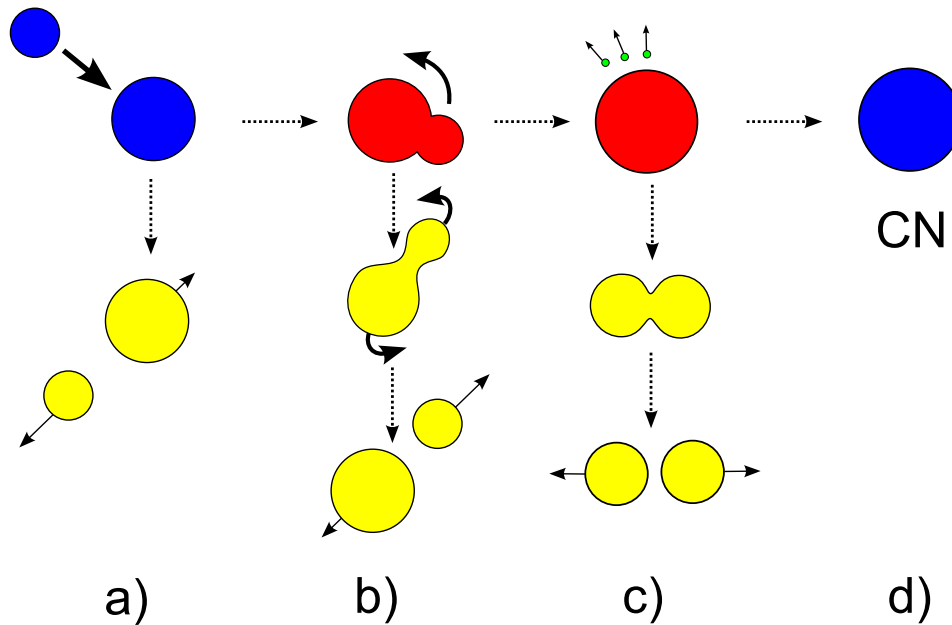
Figure 1.12: Schematic drawing of the fusion reaction towards creation of SHE. Letters under the figure describe different stages: a) collision and possible elastic scattering, b) inelastic scattering and quasi-fission, c) cooling of the excited CN with subsequent neutron evaporations or fission of CN and d) CN survival.

is reduced via evaporation of one or more neutrons and γ emission (Figure 1.12c). The probability of the survival of the CN is determined by the ratio of probability of neutron evaporation and γ emission versus fission of the compound nucleus.

In fusion reactions towards SHE the product $Z_1 \times Z_2$ reaches extremely large values ($Z_1 Z_2 > 1000$) and the fission barrier height decreases rapidly. In addition, the fission barrier itself is fragile, because it is solely built up from shell effects, which are "smeared out" in the excited nucleus. For these reasons the fusion of SHE is hindered twofold: (1) in the entrance channel by a high probability for re-separation and (2) in the exit channel by a high probability for fission. In contrast, the fusion of lighter elements proceeds unhindered, implying significantly higher production cross sections.

1.3.2   Production Cross Section

The production cross section of the xn evaporation channel of the complete fusion reaction is calculated as

$$\sigma_x = \sigma_{\text{CN}} P_x \prod_{i=1}^{x} \left(\frac{\Gamma_n}{\Gamma_n + \Gamma_f} \right)_i, \tag{1.7}$$

where σ_{CN} is the cross section for CN creation, P_x is the probability of emitting exactly x neutrons, and Γ_n and Γ_f are the partial widths for neutron emission and fission of state i, respectively. The term P_x is a function of the excitation energy. Γ_n and Γ_f represent the FWHM (full-width-at-half-maximum) of the state, undergoing neutron-emission or fission, respectively, and are proportional to the decay probability of the respective mode. Because $\Gamma_f \gg \Gamma_n$ in the region of the SHE, the equation (1.7) can be simplified as follows:

$$\sigma_x = \sigma_{\text{CN}} P_x \prod_{i=1}^{x} \left(\frac{\Gamma_n}{\Gamma_f} \right)_i, \tag{1.8}$$

Using the classical approach, σ_{CN} can be calculated as

$$\sigma_{\text{CN}} = \begin{cases} \pi R_B^2 (1 - V(R_B)/E_1) & \text{for } E_1 \geq V \\ 0 & \text{for } E_1 < V \end{cases}, \tag{1.9}$$

where R_B is the interaction distance (nuclear radius), V is the interaction potential (Coulomb energy at a distance R_B), and E_1 is the projectile energy. Sub-barrier fusion is disallowed in equation (1.9), although a quantum-mechanical tunneling through the barrier allows sub-barrier fusion [42]. The equation (1.9) also does not include any variation in the fusion cross section based on different orientations of deformed colliding nuclei. The terms R_B and $V(R_B)$ can be calculated as follows:

$$R_B = r_0 (A_1^{\frac{1}{3}} + A_2^{\frac{1}{3}}) \tag{1.10}$$

$$V(R_B) = \frac{Z_1 Z_2 e^2}{R_B}, \tag{1.11}$$

where r_0 is the radius parameter, Z_1, Z_2 and A_1, A_2 are proton and atomic number

of the projectile and target nuclei, respectively.

Because of the intrinsically low probability of fusion reactions leading to the creation of SHE and the complex interplay of sub-barrier fusion enhancement and dynamical limitations of the fusion probability, it is difficult to make theoretical estimates of the fusion probability that are sufficiently reliable to serve as a firm basis for the experiment. Many developments were done on the classical model of the cross section calculation, to improve its reproduction of experimental data (e.g. [43, 44, 45]). It should be mentioned, that the classical Coulomb barrier was found to be too high and the more realistic Bass barrier is used instead [43]. A simple formula for calculating the Coulomb potential has been proposed in [45]:

$$
\begin{aligned}
V &= 0.85247 z_c + 1.361 \times 10^{-3} z_c^2 - 2.23 \times 10^{-6} z_c^3 \; (\text{MeV}) \;, \\
z_c &= \frac{Z_1 Z_2}{A_1^{\frac{1}{3}} + A_2^{\frac{1}{3}}},
\end{aligned}
\tag{1.12}
$$

where all variables are explained above. However, the most reliable predictions on cross sections are given by statistical models. Such models were proposed in [46, 47] and significantly enhanced in the following 50 years. With the availability of computers they became an important tool for predicting production cross sections. The statistical model code HIVAP was developed at GSI for calculating production cross sections of fusion-evaporation reactions [48]. The fusion-evaporation reaction in this model is divided into several steps, whose probabilities are calculated using standard physical models, as described above. The evaporation part of the calculation is based on the evaluation of statistical fluctuations. From calculated probabilities of every involved step, production cross sections are enumerated. Statistical models including HIVAP are depending on physical parameters, whose precise values are sometimes unknown. Therefore a well-balanced set of parameters has to be found, with which the known experimental cross sections can be reproduced with sufficient precision. Finding a balanced parameter set is crucial for statistical models predictions of yet unknown reactions. For HIVAP calculations in this work, the most common parameter set proposed by Reisdorf and Schädel [49] is used.

1.3.3   Cold and Hot Fusion

The excitation energy (E^*) of the CN is a critical parameter for its survival. According to E^* nuclear fusion reactions leading to the synthesis of SHE can be divided into two groups: (i) "hot" fusion reactions at $E^* \sim 30 - 50$ MeV (evaporation of 3–5 neutrons), (ii) "cold" fusion reactions with low $E^* \sim 10 - 20$ MeV (1–2 n evaporation channel).

Examples for hot fusion reactions are reactions of light projectiles with actinide targets. These result in larger fusion cross sections but reduced survival probabilities due to the higher E^* of the CN. Using the hot fusion reactions the elements with $Z = 102 - 106$ were discovered. In reactions with the doubly magic ^{48}Ca projectile and actinide targets, a lower excitation energy of the CN can be reached, improving the survival probability. These reactions are sometimes called "warm" fusion. The production cross sections of reactions using ^{48}Ca projectiles and actinide targets are significantly higher compared to other combinations of projectile + actinide target, in which the same CN is synthesized. For this reason, reactions with ^{48}Ca projectiles have been used for the discovery experiments of elements with $Z = 113 - 116,\ 118$. A compilation of experimental cross sections is presented in Figure 1.13.

Examples of cold fusion reactions are typically reactions of massive projectiles with ^{208}Pb and ^{209}Bi targets leading to low E^* in these reactions. The formation of a surviving CN is possible after the evaporation of only one neutron. However, the fusion probability is much lower, as the product $Z_1 \times Z_2$ reaches high values. As a general rule, cold fusion reactions lead to more neutron deficient isotopes than hot fusion reactions. The elements with $Z = 107 - 112$ were synthesized for the first time using cold fusion.

The increasing Coulomb repulsion starts to severely affect the fusion cross sections of reactions, producing elements beyond fermium. From there on a continuous decrease of the cross sections was measured from microbarns for the synthesis of nobelium down to picobarns for the synthesis of element 112. The decrease of the cross sections has the same slope for both cold and hot fusion, but surprisingly the cross sections of reactions with ^{48}Ca projectiles are behaving differently - the cross sections remain stable at a level of a few picobarns for all reactions with actinide targets.
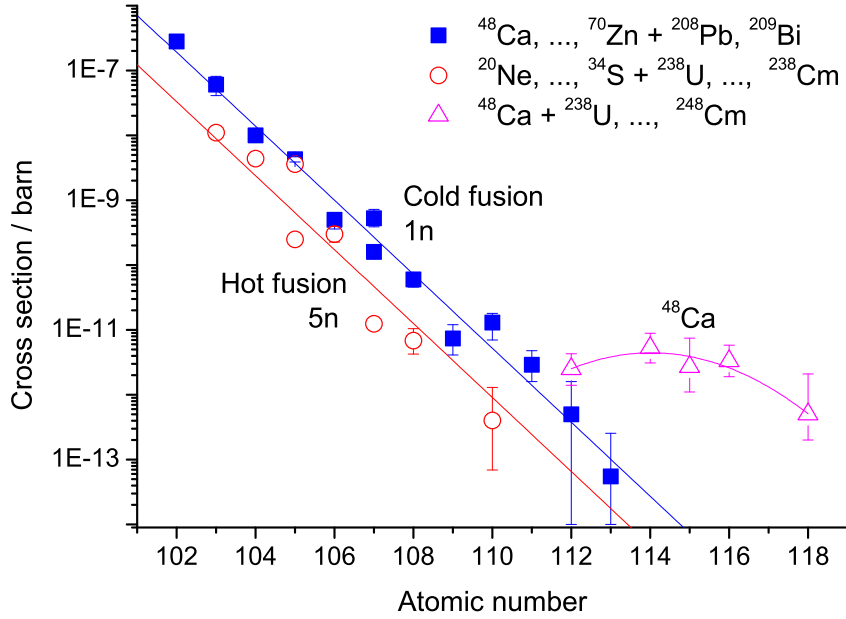
Figure 1.13: Experimental cross sections for the formation of nuclei with $Z \geq 102$ in ($\blacksquare$) the $1n$ evaporation channel of cold fusion reactions, ($\circ$) the $5n$ channel of hot fusion reactions, and ($\triangle$) the fusion reaction with the ^{48}Ca + actinide targets. The curves are drawn to guide the eye.

1.3.4 Predicted cross sections for the formation of ^{270}Hs

For the investigation of the decay properties of Hs nuclei the nuclear fusion reaction ^{248}Cm(^{26}Mg, xn)$^{274-x}$Hs was chosen. The fusion reaction ^{26}Mg+^{248}Cm was used in a previous Hs chemistry experiment and a cross section of $6 \pm^{12}_{4}$ pb for production of ^{269}Hs in the $5n$ channel was derived [3]. Calculations with the HIVAP code [49] predict production cross sections of a few picobarns for the $4n$, $5n$, but also for the $3n$ evaporation channel (see Figure 1.15). The expected production rate of Hs nuclei in the fusion reaction ^{26}Mg + ^{248}Cm is one or more atoms per day, enabling the investigation of the decay properties of Hs nuclei with acceptable statistics. In recent calculations, Liu and Bao [50] predicted cross sections of different reactions towards ^{270}Hs (see Figure 1.14). The cross section for the reaction ^{48}Ca + ^{226}Ra was predicted to be almost 3 times higher than for the reaction ^{26}Mg + ^{248}Cm used in this work. However, the validity of these calculations has to be confirmed experimentally.

To obtain strong evidence of shell closure at $N = 162$, the fusion reaction ^{25}Mg +
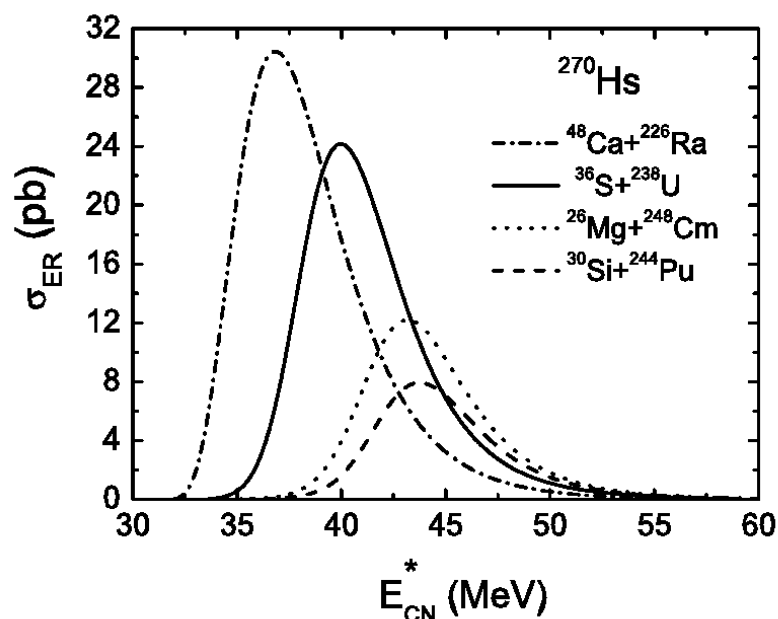
Figure 1.14: The evaporation residue cross sections (σ_{ER}) for the $4n$ channel of fusion reactions ^{26}Mg + ^{248}Cm, ^{30}Si + ^{244}Pu, ^{36}S + ^{238}U, and ^{48}Ca + ^{226}Ra. Adapted from [50].

^{248}Cm aiming at the production of ^{268}Hs was examined. The production cross section of the reaction ^{25}Mg + ^{248}Cm is expected to be lower compared to the reaction ^{26}Mg + ^{248}Cm, because of the lower number of neutrons in the projectile nucleus. At the laboratory-frame beam energy of 140 MeV, HIVAP predicts a maximum cross section of 1.3 pb for ^{268}Hs in the $5n$ evaporation channel and 0.4 pb for ^{269}Hs in the $4n$ channel. The expected production rate of Hs nuclei in this reaction is one atom per week.

1.4 Experimental evidence for shell stabilization in the SHE region

1.4.1 Experimental evidence for $Z = 108$ and $N = 162$ shells

The discovery of elements with $Z = 107-112$ was made using cold fusion reactions based on lead and bismuth targets. All these discovery experiments were carried out at the GSI employing the velocity filter SHIP (Separator for Heavy Ion reaction Products) during
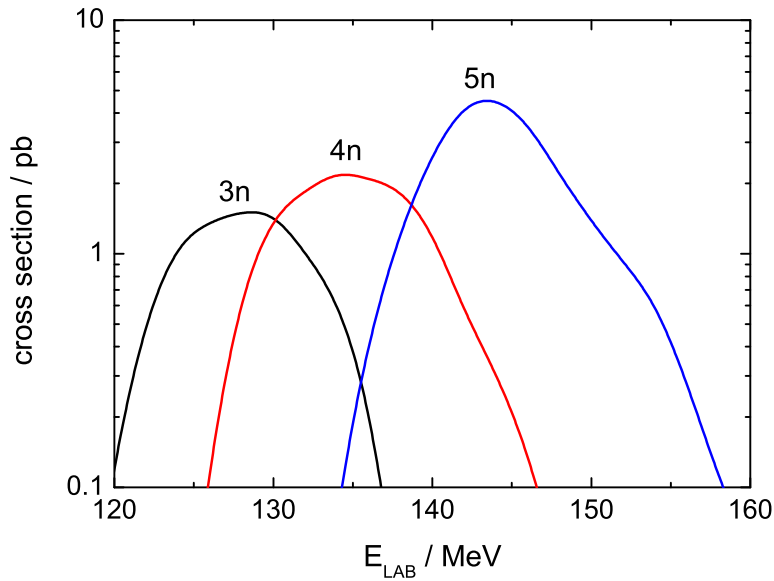
Figure 1.15: Excitation functions of the 3–$5n$ evaporation channels of the reaction ^{248}Cm(^{26}Mg, xn)$^{274-x}$Hs calculated with HIVAP using the Reisdorf and Schädel parameters [49].

the years 1981–1996. A detailed presentation and discussion of the decay properties of elements 107 to 109 and of elements 110 and 112 can be found in [51, 52, 53].

Hassium, element 108, was synthesized for the first time in 1984 using the reaction ^{58}Fe $+$ ^{208}Pb. The identification was based on observation of three decay chains, which were assigned to ^{265}Hs [54]. Only one α-decay chain was measured in the irradiation of ^{207}Pb with ^{58}Fe. The measured event was assigned to the even-even isotope ^{264}Hs [55]. Both these Hs isotopes, ^{264}Hs and ^{265}Hs, are far from the valley of β-stable nuclei and therefore their half-lives are very short, of the order of milliseconds. A much longer-lived Hs isotope, ^{269}Hs ($T_{1/2} = 11$ s), was discovered in the experiment that led to the first identification of element 112 [40]. The fist indication for a $N = 162$ neutron shell was reported from this experiment. Large differences in the α-decay energies and half-lives between ^{273}110 and ^{269}108 were interpreted as the result of a local minimum of the shell correction energy at neutron number $N = 162$, which is crossed by the α-decay of ^{273}110.

The first experiment claiming evidence of increased stability in the region of deformed SHE around ^{270}Hs by Lazarev *et al.* [56] aimed at the synthesis of Sg isotopes in the reaction ^{248}Cm $+$ ^{22}Ne. In this experiment four α-α-(α) and six α-SF decay chains were detected and attributed to ^{265}Sg and ^{266}Sg, respectively. This assignment was based on the decay properties of ^{261}Rf and ^{262}Rf known at that time: ^{261}Rf was known to decay
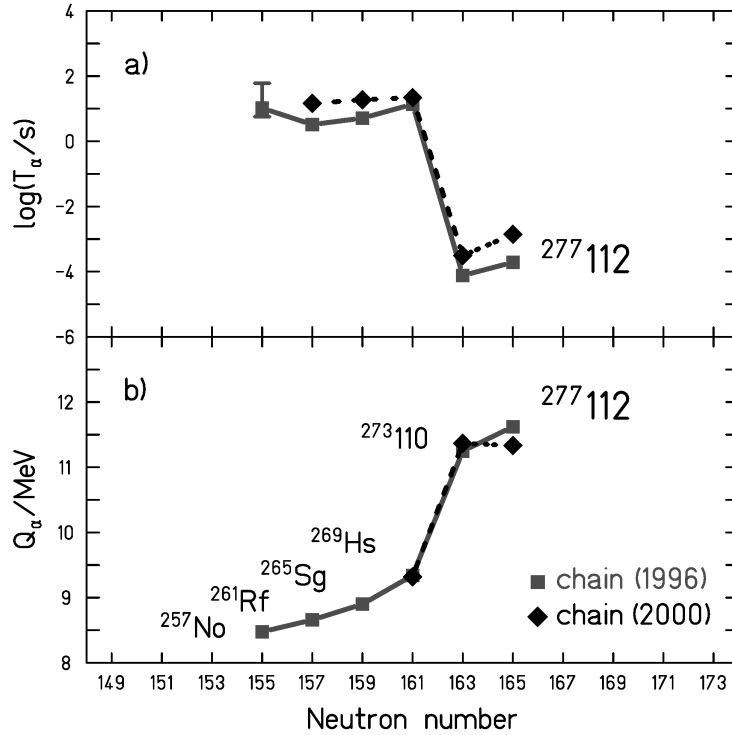
Figure 1.16: Systematics of the decay chains of ^{277}112: upper part, measured half-lives; lower part, Q_α-values. An example of the error bar of the half-lives is shown in one case. The large gap between the α-decay energy and half-lives of ^{273}110 and ^{269}108 occurs when crossing of the $N = 162$ neutron shell. Adapted from [40].

by α-decay with a half-life of 78 s [57,58] and ^{262}Rf was known to undergo spontaneous fission [59]. Because of the low recoil energy of evaporation residues (EVR), it was not possible to measure the half-life of Sg isotopes in this experiment. Single SF events could not be attributed to EVR signals and hence could not be distinguished from long-lived SF background. From the measured E_α a long half-life of 2–30 s for ^{266}Sg was derived by Lazarev *et al.* [56], which was seen as an indication of increased stability. Similar decay chains were detected later also in a chemistry experiment on Sg by Türler *et al.* [60]. Again, the decay chains were attributed according to the observed decay mode of populated Rf isotopes. Later, the observation of decay chains originating from ^{277}112 [40, 41] revealed that a second isomeric state of ^{261}Rf with a SF branch exists. In addition, Sg chemistry experiments could only detect isotopes with $T_{1/2} > 1$ s based on α-α and α-SF correlations. With the present knowledge of a SF decay branch in a ^{261}Rf isomer and because neither of the Sg experiments [56, 60] were sensitive to short-lived SF decay of Sg, which is a possible decay mode of ^{266}Sg according to theoretical calculations

(see Figure 1.11), the attribution of the decay chains from the experiments of Lazarev and Türler to ^{266}Sg may need to be revised.

The first successful Hs chemistry experiment was conducted by Düllmann *et al.* at the GSI in 2001 [2, 3]. Hassium atoms were produced in the fusion reaction ^{26}Mg + ^{248}Cm (CN ^{274}Hs). At a beam energy of $E_{\text{lab}} = 145$ MeV mostly production of ^{269}Hs in the $5n$ evaporation channel was expected, which was known as the decay grand daughter of ^{277}112 [40, 41]. During the experiment, seven correlated decay chains were detected and assigned to the decay of ^{269}Hs or tentatively ^{270}Hs. The attribution was based on the decay properties of the daughter nuclei, which was at that time believed to be known. However, the chains attributed to the decay of ^{270}Hs were similar to those, assigned to ^{269}Hs, and therefore only a tentative isotope attribution could be made.

Although considerably efforts aimed at the experimental investigation of $Z = 108$ and $N = 162$ shell closures were made, experimental evidence of these shells is inconclusive. An unambiguous measurement of the decay properties of the deformed doubly magic nucleus ^{270}Hs and evidence of stabilization of this nuclide compared to its neighbors would give the necessary strong indication of the $N = 162$ neutron shell.

1.4.2 Experimental evidence for $Z = 114$ and $N = 184$ shells

Elements with $Z = 113-116, 118$ were synthesized using ^{48}Ca as a projectile and different actinide targets at FLNR, Dubna. These reactions allowed to study more neutron-rich isotopes, which are closer to the region of spherical SHE and for which also longer half-lives are expected. An excellent overview can be found in [61]. The decay chains measured at FLNR, Dubna in ^{48}Ca + actinide targets reactions reveal to some extent internal redundancy, and the lifetimes are relatively short, making an origin by chance events extremely unlikely. However, as the chains end by spontaneous fission, genetic relations to known nuclei cannot be used, making a direct assignment difficult. An independent confirmation is necessary. Independent confirmation of the proton number can be realised in a chemical experiment. A chemical experiment confirming the decay properties of the isotope ^{283}112 produced in the reaction ^{48}Ca + ^{242}Pu after α-decay of ^{287}114 was conducted at Dubna by a group from the PSI, Switzerland [62]. Most recently, an experiment was conducted at GSI, in which the reaction ^{48}Ca+^{238}U was investigated and according to preliminary reports, four decay chains attributed to ^{283}112 were detected; the results from the experiment have not been published yet.

Although the measured relative stability of SHE with $Z > 104$ compared to the LDM model proves existence of closed shells close to $Z = 114$ and $N = 184$ and some other indications are present, definite conclusions about the position and influence of shells could not be made yet. The CN synthesized so far are too neutron-poor, far removed from the predicted neutron shell at $N = 184$. In order to reach an area close to $Z = 114$ and $N = 184$, the fusion reactions of ^{244}Pu and ^{248}Cm nuclei with heavier projectiles, such as ^{58}Fe or ^{64}Ni have to be utilized or future intensive beams of radioactive neutron-rich nuclei.

1.5   Chemical properties of SHE

1.5.1   General aspects of chemistry of SHE

The position of a new element in the Periodic Table is defined by its electronic configuration and therefore by its atomic number. Unfortunately, with increasing Z towards the super heavy elements, the cross sections and thus the production rates drop rapidly and only single atoms at a time can be produced. Moreover, chemical information can currently be accessed only for elements with a half-life of the order of a few seconds or longer. In this case, fast chemistry techniques must be used. They are based on the principle of chromatographic separations either in the gas phase exploiting the differences in volatility of heavy elements or their compounds, or in the aqueous phase by solvent extraction or ion exchange separations using differences in complex formation. Due to the very short half-lives, the chemical information obtained from these experiments is limited to the investigation of a few basic properties. Comparison with the behavior of the lighter homologues is the most important experimental approach.

The chemical properties of the heaviest elements can differ from those of their homologues, because of relativistic effects. The Coulomb force attracting the electrons to the nucleus grows with increasing Z of heavy elements. The electrons move faster, reaching relativistic velocities and their mass increases as

$$m = \frac{m_0}{\sqrt{1 - \left(\frac{v}{c}\right)^2}} \, , \tag{1.13}$$

where m_0 is the rest mass, v is the velocity of the electron and c the speed of light. As a consequence, the effective Bohr radius a_B decreases for s orbitals.

$$a_B = \frac{\hbar^2}{mc^2} = a_B^0 \sqrt{1 - \left(\frac{v}{c}\right)^2} \qquad (1.14)$$

As an example, the $1s$ electron of Sg has a velocity $v = 0.77c$ and its radius is 37% smaller compared to non-relativistic calculations. The relativistic contraction of the s and $p_{1/2}$ shells results in a more efficient screening of the nuclear charge, so that the outer orbitals become more expanded and destabilized. The third relativistic effect is the spin-orbit splitting of levels with $l > 0$ (p, d, f, ...orbitals) into $j = l \pm 1/2$. The increasing velocities of electrons to relativistic speeds make simple extrapolations of chemical properties of SHE from those of the lighter elements unreliable. Relativistic quantum theory and quantum-chemical methods have been developed in the last two decades to accurately treat relativistic effects for the many-electron problem. Figure 1.17 shows comparison of relativistic and non-relativistic calculations and the increasing difference between these two approaches with increasing Z. However, no strong deviations in electronic configuration caused by relativistic effects are expected up to element 120 ($8s^2$), with exception of predicted deviations in the filling of the f-shell ($f^7 - df^7 - f^9$). This implies that the position of a new element in the Periodic Table is fixed based on its proton number, although unusual ground state configurations may occur.

Chemical separation procedures to study chemical and physical properties of short-lived radioactive nuclides were applied as early as 1900 by E. Rutherford to determine the half-life of ^{220}Rn[65]. The discovery of new elements up to $Z = 101$ was accomplished by chemical means[1] and only from there on physical methods prevailed. Nevertheless, rapid gas phase chemistry played an important role in the claims to the discoveries of Rf and Db. The elements 104 through 108 have been successfully studied using chemical techniques in the years 1960–2001. An excellent overview of the experiments on chemical separation of SHE until the year 2003 and of the techniques used in these experiments can be found in the book "The Chemistry of Superheavy Elements" edited by M. Schädel [25].
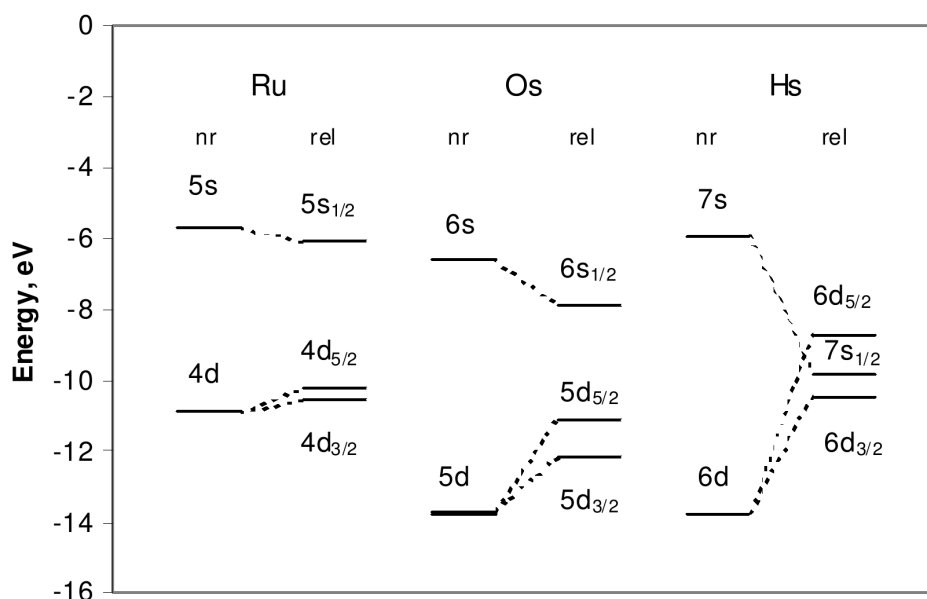
Figure 1.17: Hartree-Fock (non-relativistic) and Dirac-Fock (relativistic) energy levels of the valence ns and $(n-1)d$ electrons for group 8 elements. Adapted from [25], data from [63,64].

1.5.2 Chemistry of Hs

Element 108, hassium, is predicted to be a member of group 8 of the Periodic Table. It is a homologue of (Fe), Ru and Os. Ru and Os are the only elements known, which can form a state with an oxidation number 8+ (with the exception of Xe, which is known to form highly unstable and explosive XeO_4). HsO_4 behaves similarly to OsO_4 and its high volatility can be used for an effective separation of this element from non-volatile products. This approach was indeed used in several experiments on chemical separation of Hs.

In 1985, experiments searching for SF decaying isotopes of element 108, produced in heavy-ion induced fusion reactions ^{40}Ar+^{235}U (CN ^{275}110), were performed at FLNR, Dubna [66]. In another experiment using the ^{22}Ne+^{249}Cf reaction (CN ^{271}Hs) at 123 MeV, α or SF decaying ^{267}Hs was searched for, which was believed to have a half-life on the order of 1 s [66,67]. In test experiments with Os, OsO_4 was efficiently adsorbed on a Pb layer, however, the main experiment was not sensitive enough to detect Hs events.

Another set-up called On-line Separation and Condensation AppaRatus (OSCAR) was installed at the 88-inch cyclotron in Berkeley in the year 1987 [68,69]. OSCAR was

used to search for α-decaying ^{272}Hs which was expected to be the EC daughter product of ^{272}Mt. In test experiments, the efficiency for the separation and condensation of osmium was 36 %. However, no Hs events were detected and an upper limit for the production cross section of 1 nb was established.

The first successful experiment on Hs chemistry was conducted by Düllmann *et al.* at the GSI in 2001 [2,3]. A schematic drawing of the experimental setup is shown in Figure 1.18. Nuclear reaction products recoiling from the target were thermalized in the gas volume of the IVO device [70] flushed with a dry helium + oxygen mixture. The reaction products were transported with the carrier gas through a quartz column containing a quartz wool plug. This plug was heated to 600 °C and served as a filter for aerosol particles. At the same time it provided a surface to complete the oxidation reaction of Hs to hassium tetroxide. The HsO$_4$ molecules were further transported through a PFA capillary to the detection system. For the adsorption of HsO$_4$ from the gas phase, adsorption thermochromatography was used. The chromatographic column, the Cryo OnLine Detector (COLD), also served as detection system for the identification of decaying atoms of Hs. COLD consisted of 12 pairs of silicon PIN-photodiodes, mounted at a distance of 1.5 mm, suitable for detection of α-particles and fission fragments. A negative temperature gradient from -20 °C to -170 °C was established along the detector array. The efficiency for detecting a single α-particle emitted by a species adsorbed within the detector array was 77%. COLD was an improved version of a previous set-up called the Cryo-ThermoChromatography separator (CTS) [71]. Decay chains detected in this experiment were assigned to the decay of ^{269}Hs or tentatively ^{270}Hs. From the observed deposition temperature of Hs, its adsorption enthalpy was derived and hence confirmed expected chemical properties of Hs.

The next experiment aimed at the investigation of the chemical properties of Hs was a chemistry experiment conducted by A. von Zweidorf *et al.* at the GSI in 2002 [73]. In this experiment the same fusion reaction ^{26}Mg + ^{248}Cm and the same beam energy of $E_{\text{lab}} = 145$ MeV as in the previous experiment [2] was used. The setup for chemical separation of Hs in the form of HsO$_4$ was also identical. The only difference in the production phase was the addition of a small amount of ^{152}Gd to the Cm target, in order to produce short-living Os isotopes, which served as an on-line control of the experiment. The new detection apparatus CALLISTO (Continuously working Arrangement for cLusterLess transport of In-SiTu produced volatile Oxides) was used. The volatile Os and Hs tetroxides were transported to the detection setup, where they were deposited on a surface, covered with a thin layer of NaOH. In analogy to OsO$_4$,
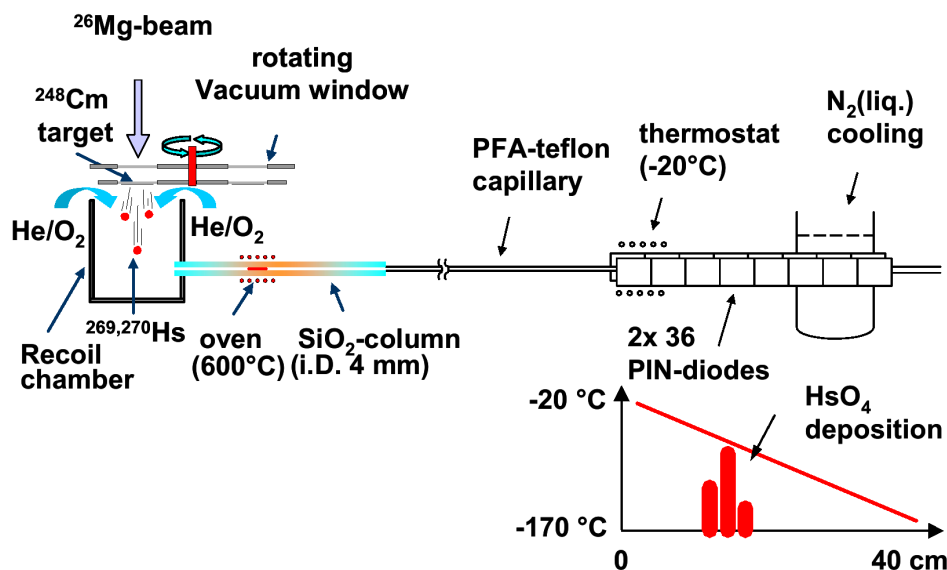
Figure 1.18: Schematic drawing of the experimental setup used in Hs chemistry experiment, which was carried out by Düllmann *et al.* [72].

which forms $Na_2[OsO_4(OH)_2]$, an osmate(VIII), with aqueous NaOH, HsO_4 presumably was deposited as $Na_2[HsO_4(OH)_2]$, a hassate(VIII). A detection system consisting of 16 silicon PIN-photodiodes was facing a layer of NaOH, allowing the detection of α particles and SF fragments. Altogether six decay chains were assigned to the decay of Hs isotopes. However, due the 2π detection geometry and the resulting low detection efficiency, mostly incomplete decay chains were detected. In addition, the energy of α-particles was partially lost in the alkali layer, resulting in a resolution of 80–130 keV. Because of these reasons it was impossible to make an unambiguous confirmation of the decay properties of ^{270}Hs.

1.6   Summary and Outlook

During the last 25 years the reaches of the Periodic Table were substantially extended towards superheavy elements. The discovery of the elements 107–116 and 118 correspond to an increase of the number of known elements of almost 10%. A compilation of all known nuclides of SHE and their decay properties is presented in Figure 1.19 in form of a cutout of the chart of nuclides.

SHE exist solely because of enhanced nuclear stability, due to shell effects. Two

centers of stabilization again spontaneous fission exist in the region of SHE: one around the predicted spherical doubly magic nucleus $^{298}114$ and one around the deformed doubly magic nucleus ^{270}Hs. Confirmation of enhanced stability of these nuclei would prove the hypothesis of their magicity and give an important reference point for theoretical calculations.

Experimental studies have shown that cross sections for the synthesis of SHE decrease continuously, with exception of warm fusion reactions of doubly magic ^{48}Ca with actinide targets. The recent data from Dubna prove the importance of the choice of the nuclear reaction. More systematic studies are needed for a better understanding of the reaction mechanism of fusion reactions in the SHE region and for confirmation of the new findings from Dubna. Yet, the exploration of the "island of stability" will be a difficult task, since many technical developments have to be done first. To advance towards the spherical shell at $N = 184$ a big neutron excess is needed, which can be reached only with radioactive ion beams. However, the construction of an accelerator, which can handle radioactive beams with sizable beam currents, is a remote future.

Exploration of nuclei close to the doubly magic ^{270}Hs is close to the border of present technical limitations. Although the experimental confirmation of $Z = 108$ and $N = 162$ shell closures is one of the key tasks of nuclear physics, experimental evidence of these shells is inconclusive. From the decay scenario can be derived, that the most likely decay mode of ^{270}Hs is α-decay with a half-life of several seconds. Both even-even isotopes neighboring ^{270}Hs, ^{268}Hs and ^{272}Hs are expected to decay by α-particle emission with half-lives shorter than one second. A significantly longer half-live of ^{270}Hs compared to its neighbors results from stabilization due to the $N = 162$ nuclear shell.

As shown by Düllmann *et al.* [2], a chemical separation of Hs is a very efficient method for the systematical study of chemical and decay properties of Hs isotopes. These informations are urgently needed for the understanding of shell stabilization in the region of superheavy elements and the dynamics of fusion reactions towards SHE. Credible results on the decay properties of ^{270}Hs, a confirmation of its magicity, and a study of the dynamics of fusion reactions are extremely important topics, which were the focus of this thesis.

Three experiments on Hs chemistry, prepared at the Institute for Radiochemistry of TU München were performed at the GSI Darmstadt. The first experiment was aimed at a confirmation of the identification of doubly magic ^{270}Hs in the reaction ^{26}Mg + ^{248}Cm, reported tentatively from the experiment of Düllmann *et al.* [2]. The objective

of the second experiment was to confirm the high cross section of the $3n$ channel in the reaction ^{26}Mg + ^{248}Cm and to investigate the fusion dynamics of this reaction. The goal of the third experiment, conducted in the year 2006, was to detect the so far unknown even-even Hs isotope ^{268}Hs in the $5n$ evaporation channel of the reaction ^{25}Mg + ^{248}Cm.
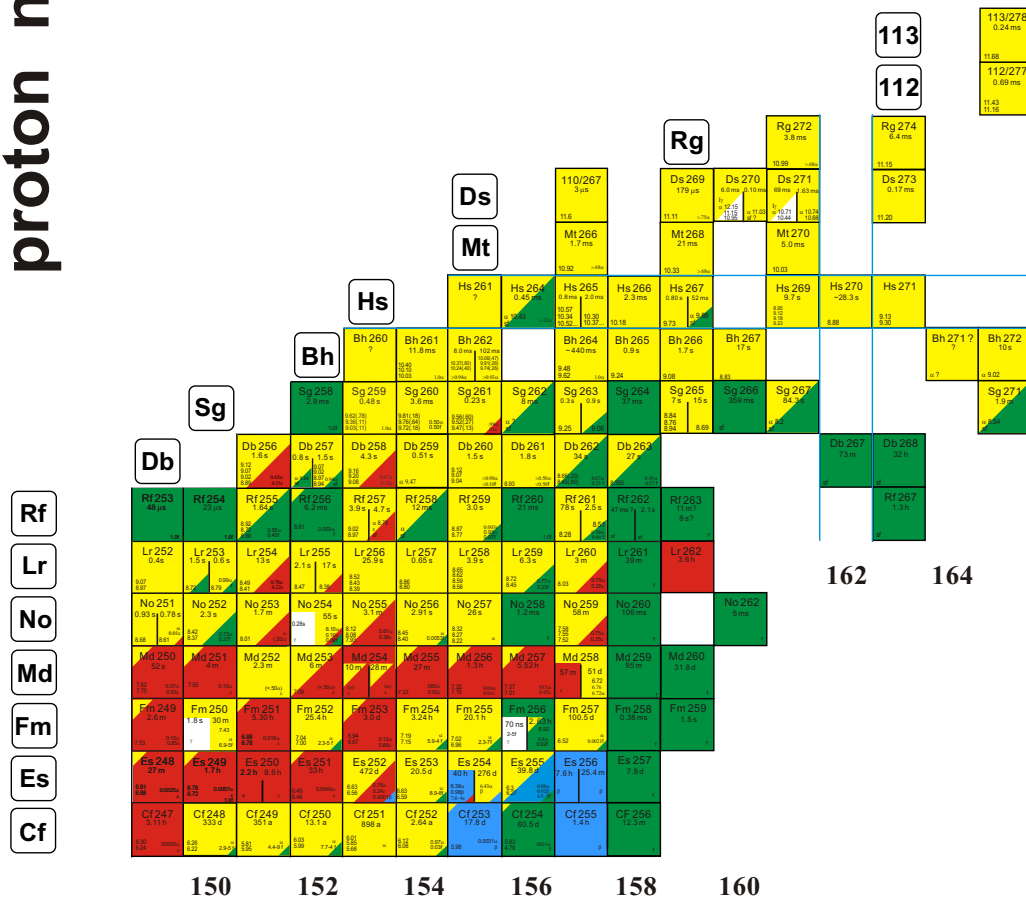
Figure 1.19: Chart of the nuclides, showing the region of SHE, part I.
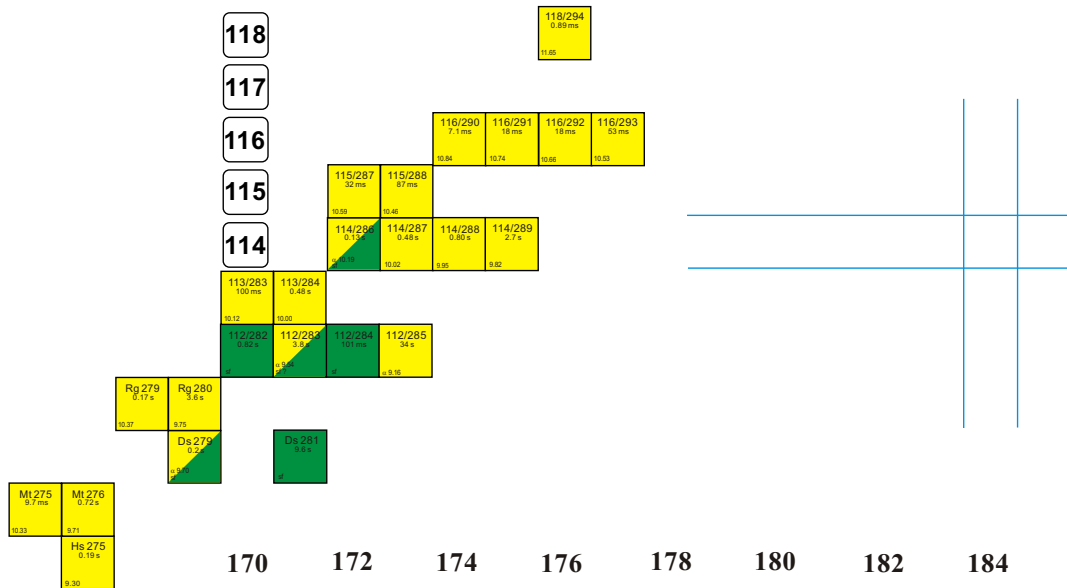
Figure 1.20: Chart of the nuclides, showing the region of SHE, part II.

Chapter 2

Experimental setup

"Theory guides, experiment decides."
— Personal motto of Izaak Maurits Kolthoff (1927–1962).

2.1 Overview

The experimental setup used was in principle the same on as described in ref. [2,3]. A schematic drawing of the experimental setup is shown in Figure 2.1. A beam of Mg ions impinged on a rotating ^{248}Cm target. Products of the nuclear reactions recoiled from the target and were stopped and thermalized in a He/O$_2$ mixture in the heated recoil chamber (RC). Because the helium contained 10% of oxygen, recoiling products of nuclear reactions were partially oxidised already in the RC. A gas flow sweeping the RC transported volatile species to a quartz wool plug inside an oven. This plug served as a filter for aerosol particles and provided a surface for completion of the oxidation reaction. All non-volatile species were effectively stopped by this filter, volatile species like HsO$_4$, OsO$_4$, Rn or At passed through the filter. Section 2.2 describes the irradiation setup in more detail.

Species volatile at room temperature were transported further through a PTFE (PolyTetraFluoroEthylene) capillary to the detection system COMPACT (Cryo On-line Multidetector for Physics And Chemistry of Transactinides). COMPACT is a separation and a detection system which allows to detect the nuclear decay properties of the species
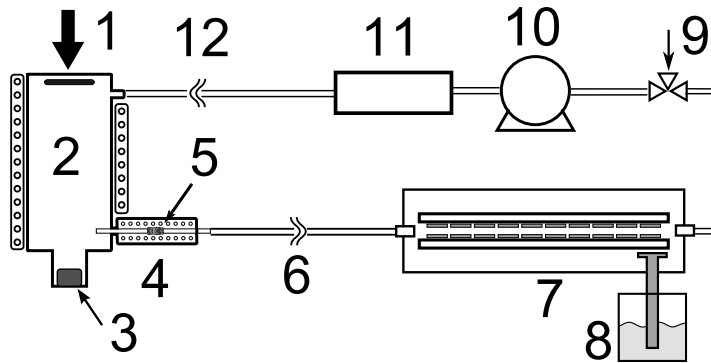
Figure 2.1: Schematic drawing of the experimental setup: (1) heavy ion beam, (2) heated recoil chamber with target, (3) beam stop, (4) oven, (5) quartz filter, (6) PTFA capillary for gas transport to detector, (7) COMPACT detection system with 2×32 PIPS detectors, (8) liquid nitrogen cooling, (9) gas mixture and flow control, (10) membrane pump, (11) NYAD$^{\text{TM}}$ measurement device, (12) gas inlet into the recoil chamber.

without the need of sampling. The detection in COMPACT is based on the principle of thermochromatography [71]. In COMPACT the thermochromatography column (TC) is formed by two arrays of 32 PIPS detectors sensitive to α-decay and spontaneous fission. The lowest temperature of $-160\,°C$ was reached in COMPACT using liquid nitrogen cooling. The design of COMPACT is discussed in Section 2.3.

The carrier gas was circulating in a loop, see Figure 2.1, in which flow and pressure of the gas were controlled remotely. The small leak rate (4 ml/min) was compensated by adding new oxygen and helium from tanks. Oxygen and water content in the helium gas were continuously monitored by a NYAD$^{\text{TM}}$ measurement device. To minimize water adsorption in COMPACT, the helium gas was dried in a cold moisture trap. Details of the gas system are presented in Section 2.4.

2.2 Irradiation setup

Hs nuclei were produced in intense bombardments of a ^{248}Cm target with Mg ions at the UNILAC (UNIversal Linear ACcelerator) at the GSI Darmstadt. The UNILAC can provide beams of accelerated ions of elements from carbon to uranium with energies up to 20 MeV/u. The beam is pulsed with a 25% duty cycle and a pulse length of 5 ms.

In the experiments conducted in the years 2004 and 2005, a beam of ^{26}Mg^{5+} ions was

delivered by the UNILAC accelerator. In the year 2006 experiment a ^{25}Mg^{4+} projectile was used instead. Typical beam intensities were 0.8 - 1 particleμA. Before entering the target material, the beam passed through 19.7 μm thick Be vacuum windows, 6 mm of He/O$_2$ mixture (10% O$_2$) and 15.3 μm thick Be target backing, supporting the target material.

Due to the energy loss of the beam in the vacuum window and the target backing a power of 10 W was generated during the bombardment with typical beam intensities. An effective cooling was necessary to prevent damage to the target and the windows due to overheating. Indeed, the target and window resistance against heat and radiation damages is the limiting factor for not increasing the beam intensities even further. In our experiment a beam wobbler was used, which allowed the spreading of the beam spot over a surface of 0.4 cm^2. Additionally, the rotating target and vacuum window wheel, ARTESIA, was used instead of a stationary target. Such a technically challenging irradiation setup was constructed and put into operation by M. Schädel et al. [74]. The target consisted of 3 arc shaped segments with an average thicknesses of 788 μg/cm^2, 743 μg/cm^2 and 244 μg/cm^2 of Cm (^{248}Cm 95.8%, ^{246}Cm 4.2%), see Figure 2.2. One segment contained 2% in weight of ^{152}Gd (30% enrichment) for the simultaneous production of α-decaying Os isotopes, the chemical analog of Hs. The target wheel was rotating at 2000 rpm, in synchronization with the beam pulse. The rotation of the target wheel allowed to spread the beam over a larger target area than in the case of a stationary target, which made the cooling of the target much more effective.

Products recoiling from the target were stopped in a gas mixture at 1.1 bar in a recoil chamber (Figure 2.3). The beam passing through the target was stopped on a water cooled copper beam dump at the end of the RC. The depth of the RC and the gas pressure in the RC were optimised for the stopping range of recoiling Hs atoms. In order to accelerate oxidation of the products, the RC was heated to 400 °C. The RC was flushed with 1.5 or 1.8 l/min He/O$_2$ mixture (10% O$_2$). The gas flow carried the volatile compounds of products, including volatile HsO$_4$ and OsO$_4$, to the quartz wool filter, kept at 650 °C. Here the oxidation process was completed and non-volatile products were retained. The retention time for volatile species was negligible in comparison with the transport time to the detector. The separation factor of the filter for separation of volatile species from nonvolatile species was $> 10^6$.

Because of the high radiation close to the target during an irradiation, the detection setup was placed behind a two meter thick concrete wall. The length of the transport line was up to ten meters, corresponding to transport times of about two seconds. Therefore,
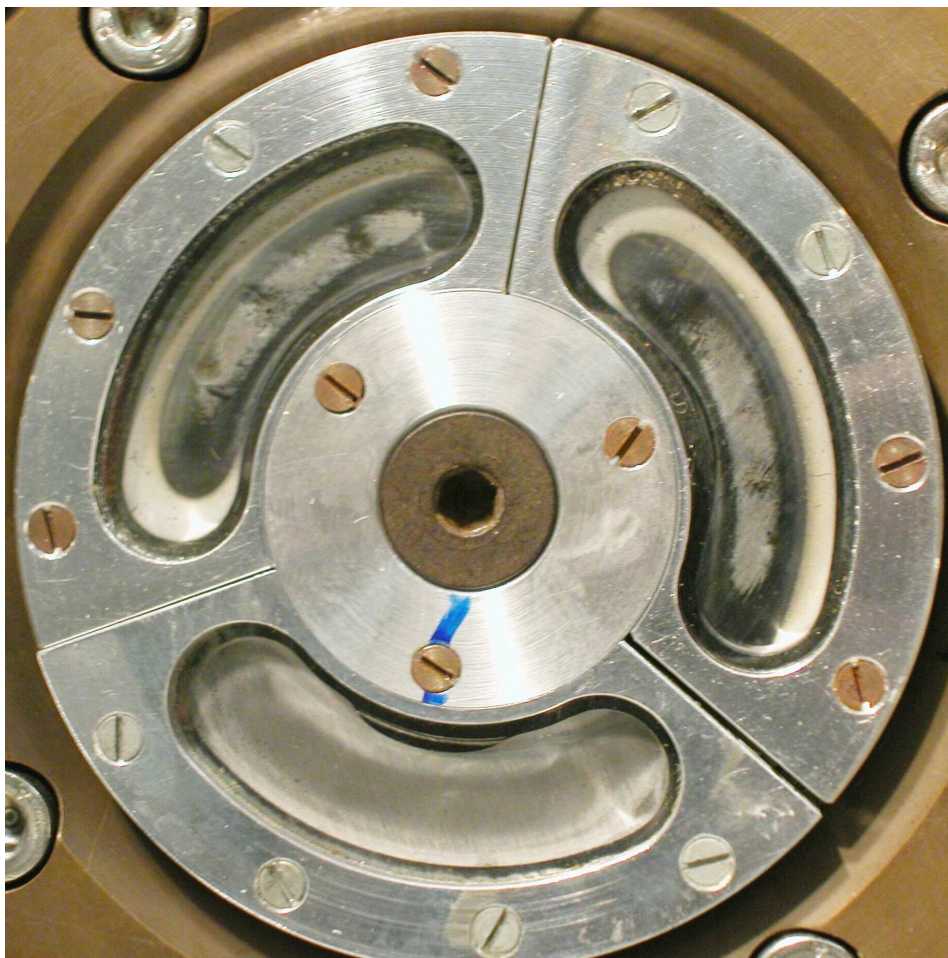
Figure 2.2: Photography of the target wheel ARTESIA with ^{248}Cm targets used in the TUM experiments on Hs chemistry. Photo courtesy of W. Brüchle.

in the search experiment of short-lived ^{268}Hs ($T_{1/2} < 1$ s), synthesized in the nuclear reaction ^{25}Mg + ^{248}Cm, the detection setup was placed in a shielded position inside the irradiation cave.

Placing COMPACT, surrounded by shielding, directly in the irradiation cave allowed to shorten the length of the capillary to 4 m, corresponding to a transport time of about one second. The shielding of COMPACT consisted of a 40-cm thick concrete wall, a 15-cm thick boron-paraffin layer, and a 7-cm thick Pb layer. This shielding proved to be satisfactory. No electronic noise was observed and the background of events detected in the detector did not increase significantly compared to previous experiments, when COMPACT was located outside of the irradiation cave.
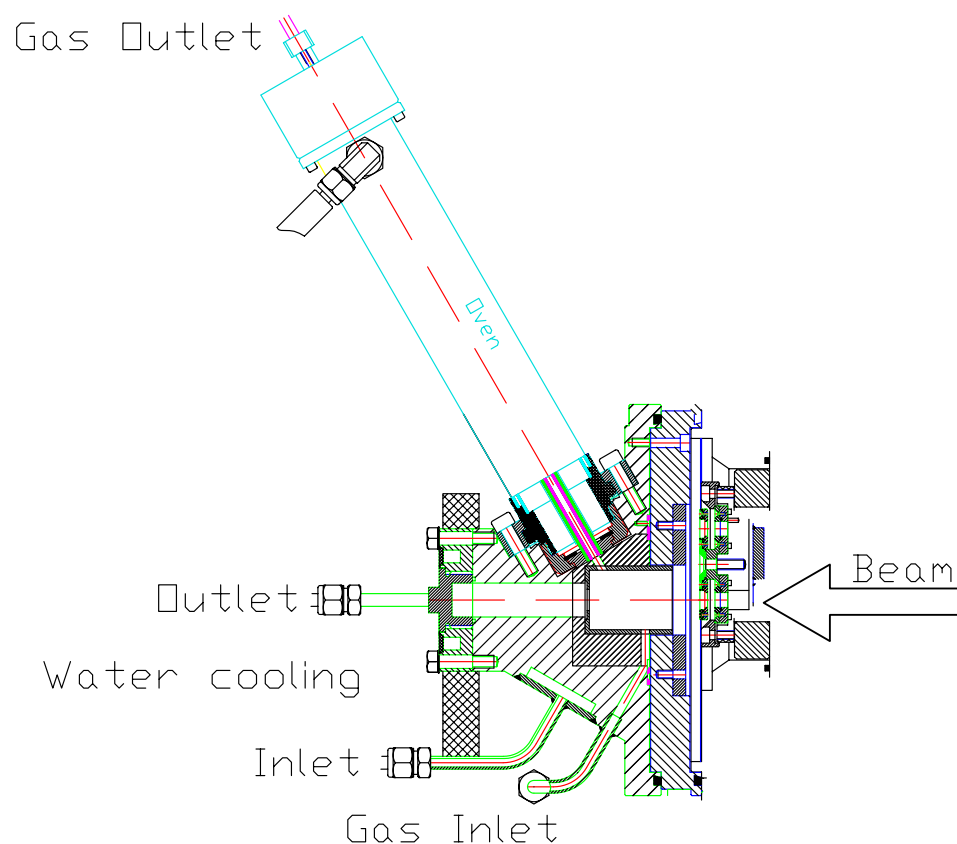
Figure 2.3: Schematic cross section drawing of the recoil chamber. The oven attached to the gas outlet contains the quartz wool filter.

2.3   Detection system COMPACT

The detection system COMPACT (Cryo Online Multidetector for Physics And Chemistry of Transactinides) was constructed particularly for chemical experiments with Hs, as well as future experiments with elements 112 and 114. Its commissioning was accomplished in the frame of this thesis. COMPACT was designed for the detection of volatile compounds of α-decaying superheavy elements. The detection system COMPACT is constructed as a thermochromatography column (TC) [75], covered on the inner side with silicon diodes for the detection of α-particles and SF fragments. The design of such a detection system was developed by Kirbach *et al.* [71] and proof of principle was obtained observing the nuclide ^{269}Hs and its decay daughters after chemical isolation by Düllmann *et al.* [2].

A carrier gas is flowing through a chromatography column, to which a negative longitudinal temperature gradient has been applied. Species, that are volatile at a
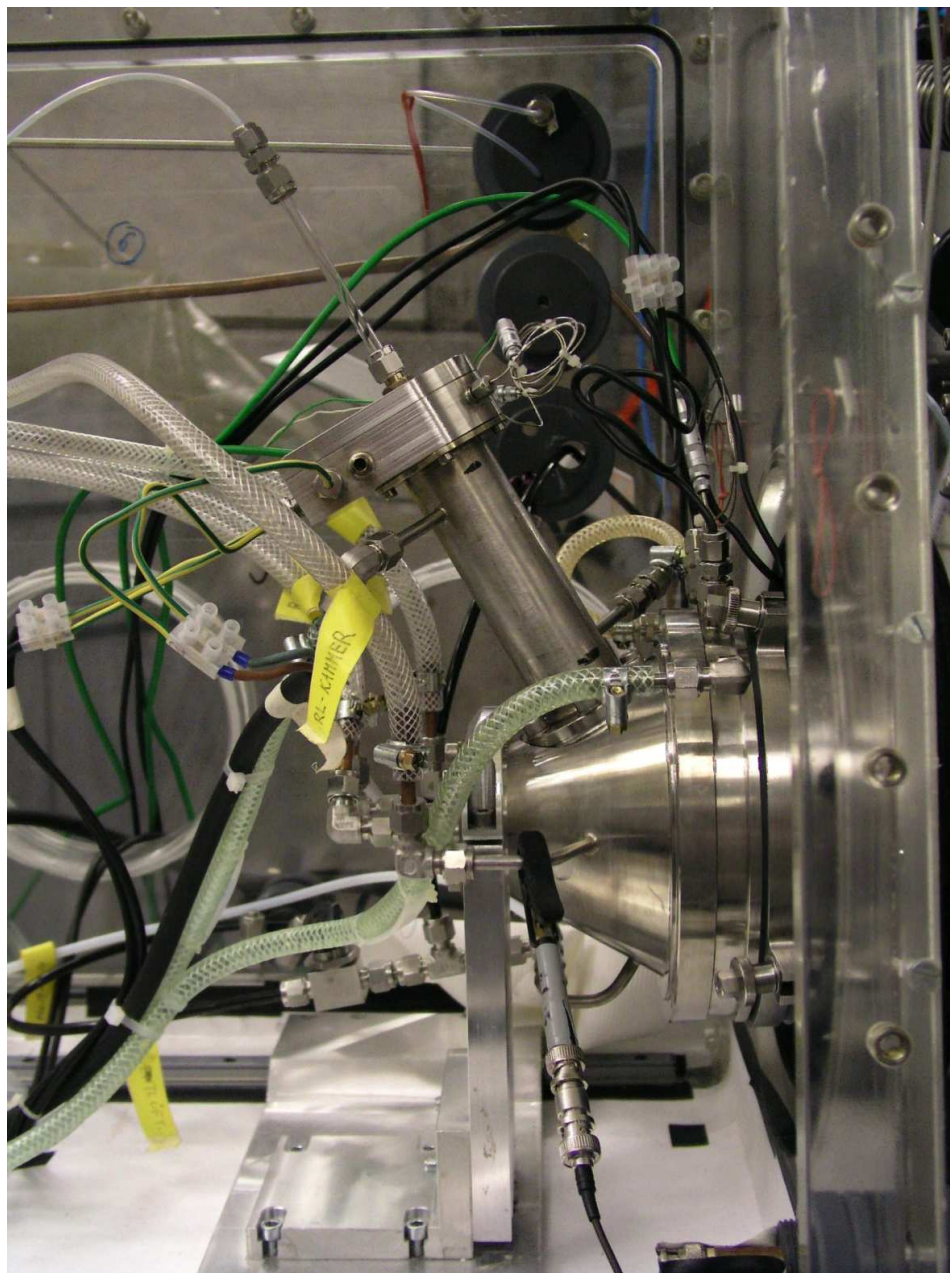
Figure 2.4: Photography of the mounted recoil chamber with the oven connected to the gas outlet.

starting point, are transported through the column downstream by the carrier gas flow. Due to the decreasing temperature in the column, the time the species spend in the adsorbed state increases exponentially. Different species form distinct deposition peaks, depending on their adsorption enthalpy (ΔH_a^0) on the column surface and thus are separated from each other. The thermochromatography column used consisted of two

linear arrays of 32 PIPS (Passivated Implanted Planar Silicon) detectors (1×1 cm^2 in size), glued to the inner walls of two Invar$^{\text{TM}}$ panels into which a grove was machined. The two panels were joined together and sealed with 1 mm In-wire, forming a vacuum tight gas channel. The gas carrying volatile species flowed through a 0.5 mm wide gap formed between the panels. A schematic drawing of the arrangement of the PIPS detectors in the Invar panel$^{\text{TM}}$ is shown in Figure 2.5. Electrical feedthrough contacts were welded into the Invar panels and sealed with epoxy. The leak rate was dependent on the temperature of the detector, but not exceeding 3 ml/min (0.2 % of the nominal gas flow) under experimental conditions. The PIPS diodes were designed at the Institute of Electron Technology, Warsaw. They were 300 μm thick epitaxial silicon PIN diodes with 100 μm thick active layer, sensitive for α-particles and fission fragments. The active area of a PIPS diode was 9.3×9.3 mm^2. The surface of the diodes can be covered with a thin layer of various materials depending on the chemical properties of the element or compound to be investigated. The nearly 4π detection geometry yielded a high detection efficiency, necessary for the investigation of SHE. The probability for detecting an α-particle emitted from a species deposited anywhere in the detector channel, including non-active surface of diodes and channel sides, was 78%. Analysis of the detection efficiency is presented in Chapter 3. The detectors were calibrated off-line with ^{219}Rn and its α-decaying products emanating from an ^{227}Ac source. The energy resolution was better than 50 keV (FWHM) under experimental conditions.

The negative temperature gradient from +20 to -160 °C was achieved by cooling the exit end of the TC column with liquid nitrogen. The temperature profile was monitored on-line with four temperature sensors. After drying of the gas in condensation cold-traps and by chemical means a dew point of -60 °C was achieved under experimental conditions, minimising water adsorption on the inner detector surface. A thin ice layer was formed during the experiment on surfaces with temperatures below the dew point. The ice layer was negatively affecting the detection resolution in the cold part of the detector channel. Because HsO$_4$ molecules were adsorbed at higher temperature (-40 °C), formation of ice did not degrade the detector resolution for Hs decays. The detector was heated up to room temperature once a day to remove the ice layer from the detector channel.

The signals from the PIPS diodes were processed in spectrometric electronics, built at Joint Institute for Nuclear Research, Dubna. A schematic diagram of the COMPACT electronics is presented in Figure 2.7. 64 PIPS diodes were connected to four 16-channel preamplifiers through coaxial cables. The diodes were operated at 10 V, the average
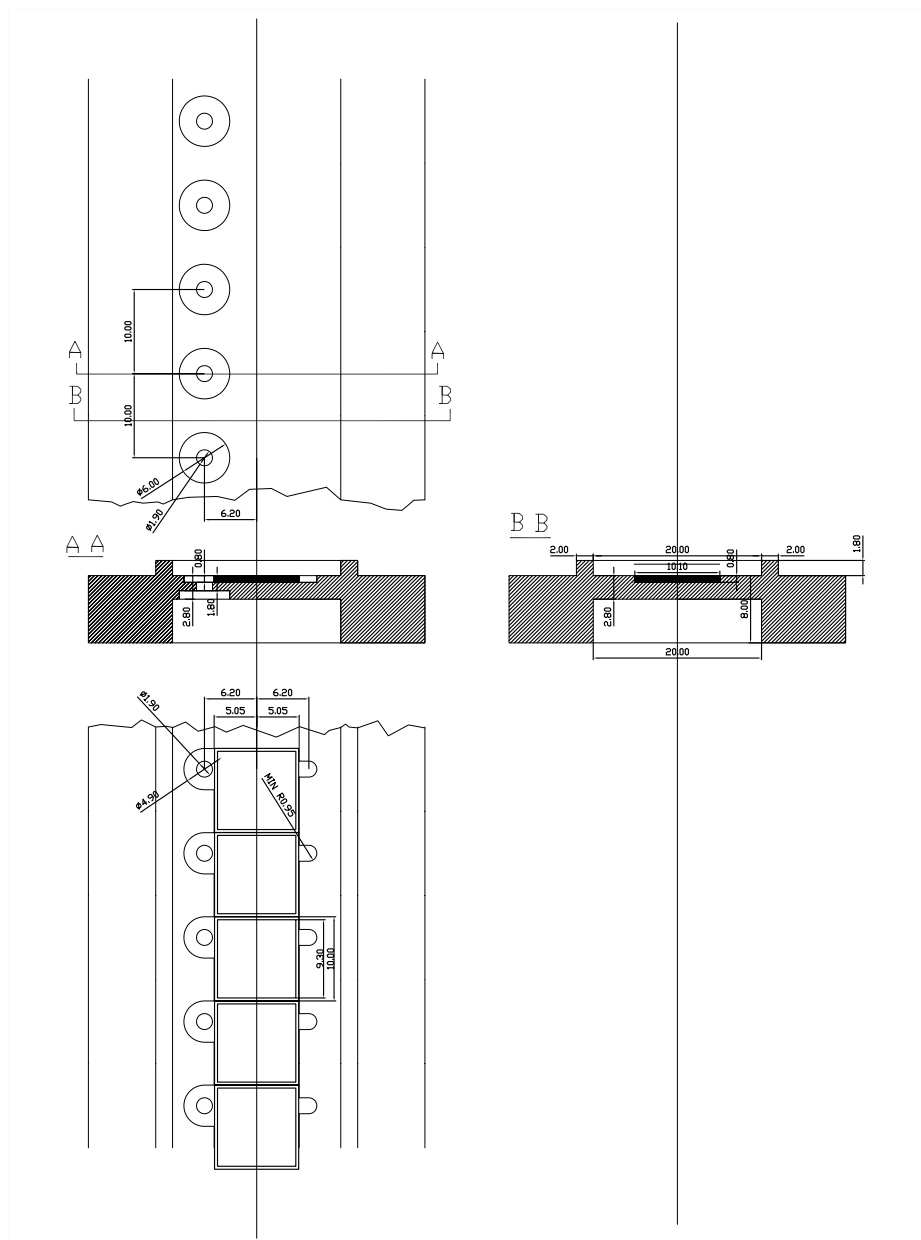
Figure 2.5: Technical drawing of the COMPACT detector. The design of the vacuum feedthroughs and the arrangement of the PIPS diodes in the Invar panel are shown.

dark current through one single diode was ~ 10 nA. Signals from the preamplifiers were transported over coaxial cables to four 16-channel amplifiers with two amplification ranges ($\times 1$ and $\times 10$). Then they were multiplexed in 8 multiplexors. The analog
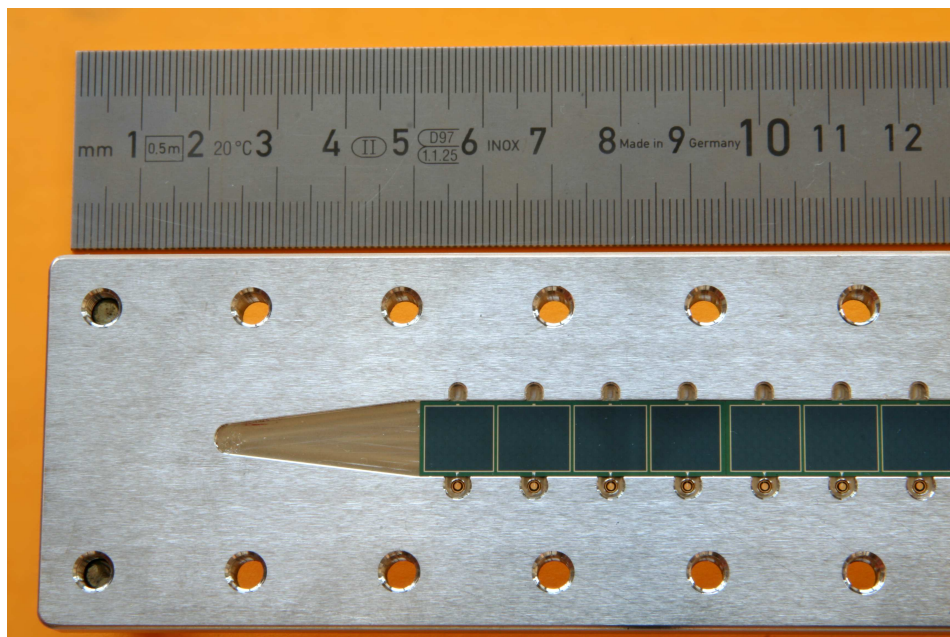
Figure 2.6: Photograph of one Invar panel with glued-in PIPS detectors.

signal and digital information about the detector number from the multiplexor were processed in a 12 bit ADC. The ADC module consists of 8 ADCs, a 1 μs clock and a communication module based on the ALTERA$^{\mathrm{TM}}$ chip. The ADC device was read out by the data acquisition computer via a PCI interface card containing a FIFO buffer. The readout time was 5 μs, hence a signal counting rate with a frequency of up to 200 kHz could be processed. Data were transfered via a computer network to a data analysis computer, placed in the control room. The data analysis software allowed on-line visualization of the data and an on-line correlation search. The COMPACT electronics was constructed to be reliable and easily transportable. The power supply for the electronics, all amplifiers, and ADCs were designed as 19" rack modules. Hence, it was possible to place the whole electronics together with the power supply and test modules in a 12 U 19" rack.

2.4   Gas system

Because the detector was cooled down to a very low temperature, the water content of the transport gas had to be removed to avoid water condensation and ice formation on cold surfaces inside the detector channel. This was achieved by continuous recycling and
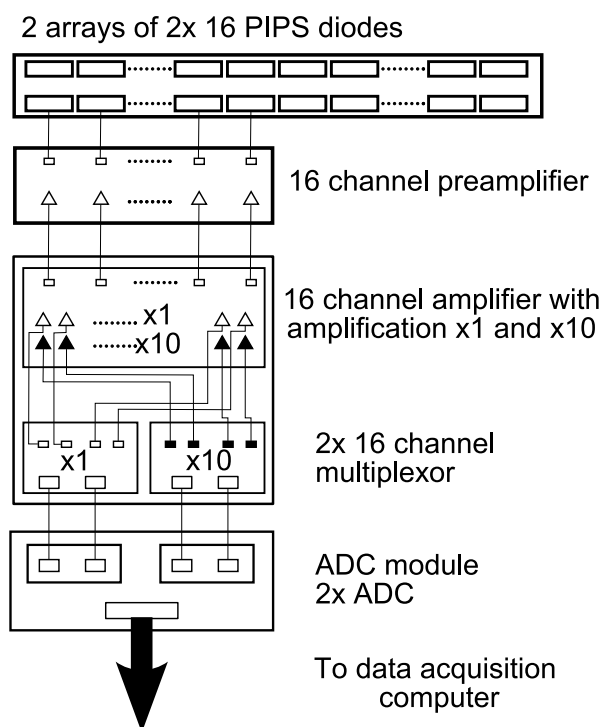
Figure 2.7: Schematic drawing of the data acquisition electronics. Connections for the readout of 16 out of 64 PIPS diodes are shown.

drying of the gas. Another important condition was the pressure in the recoil chamber, which was limited by a ~ 20 μm thin Be vacuum window, separating the RC from the accelerator beam line, to a maximum pressure difference of 1.2 bar. Especially during an irradiation of radioactive targets like ^{248}Cm any rupture of the vacuum window is extremely dangerous and has to be avoided. Reliable and fast acting safety precautions have to be employed to avoid a pressure increase, which can result in a window rupture.

A schematic drawing of the gas system used in TUM experiments on Hs chemistry is shown in Figure 2.8. Gas was circulating in a loop, flow conditions and the composition of the gas were controlled continuously by a computer. The control software was written in Labview^{TM} and it allowed automatization of the gas control. Safety measures consisted of two independent systems. The first safety system, shown in Figure 2.8 as a box with a description "GSI safety valves", was a system of hardware operated valves, which immediately ventilated the recoil chamber to air in case of an overpressure or underpressure in the recoil chamber. The second safety system was operated by the control server, which prohibited all flows in the gas system and switched the system to the by-pass mode in case of any unexpected behaviour of the gas system.
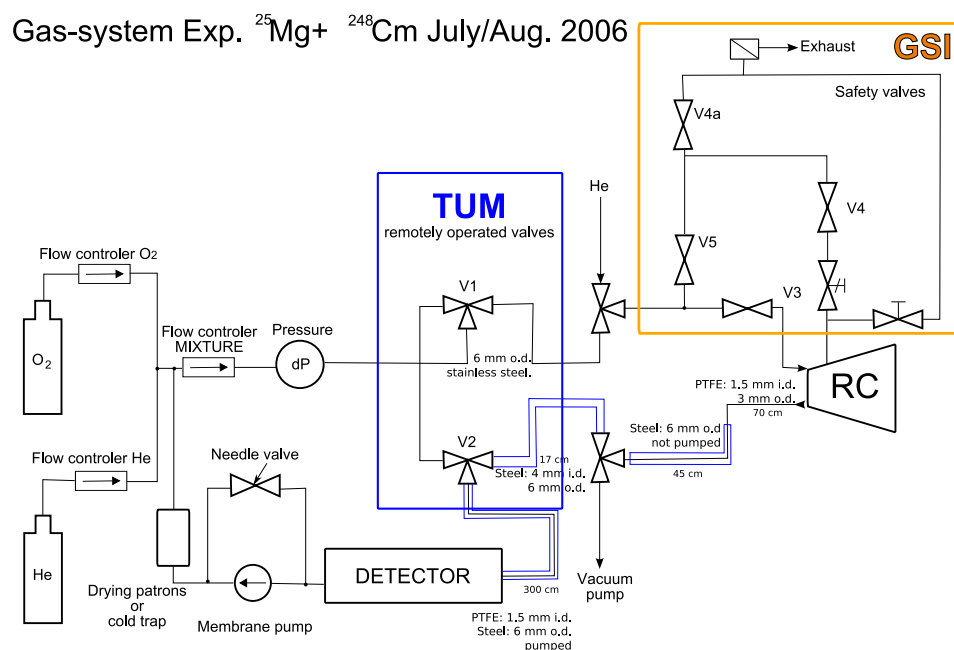
Figure 2.8: Schematic drawing of the improved gas system, as used in the ^{25}Mg + ^{248}Cm experiment. Contrary to the previous two experiments, remotely operated valves (in the box in the middle of the figure) were added to minimize a possible water contamination during a ventilation of the system to air. Also the length of the capillary between the recoil chamber and the detector system was minimized in the last experiment in order to reach a transport time as short as possible.

The amount of water vapors in the gas was determined by a NYAD$^{\mathrm{TM}}$ device through the dew point temperature. For drying of the gas, a cold trap filled with Sicapent$^{\mathrm{TM}}$, or another chemical drying agent was used. A dew point of -60 °C was achieved under experimental conditions, which proved to be sufficient to keep the part of the detector surface clean, where HsO_4 adsorbed.

At typical gas flow rates a transport time of about 3 s was achieved in the experiments ^{26}Mg + ^{248}Cm. In the last experiment to search for ^{268}Hs in the reaction ^{26}Mg + ^{248}Cm, the transport line was significantly shortened to reach faster transport times. The transport time of the improved setup was estimated from measurements with short-lived Os isotopes. In bombardments of an enriched ^{152}Gd target with a chopped (1 s on/59 s off) ^{25}Mg beam, the isotopes ^{171}Os and ^{172}Os with half-lives of 8.3 and 19.2 seconds, respectively, were produced. Because the stopping range of recoiling Os atoms is larger than in the case of Hs, the recoil chamber depth was extended by 15 mm to ensure, that the products are stopped in the same position relative to the exit capillary.

The time dependence of the counting rate of Os decays was examined and is presented in Figure 2.9. The time dependence of the Os counting rate in the detector was fitted using a theoretical model [76]. A mean transport time of 1.4 s at typical flow rates of 1.5 l/min was evaluated for the improved setup.
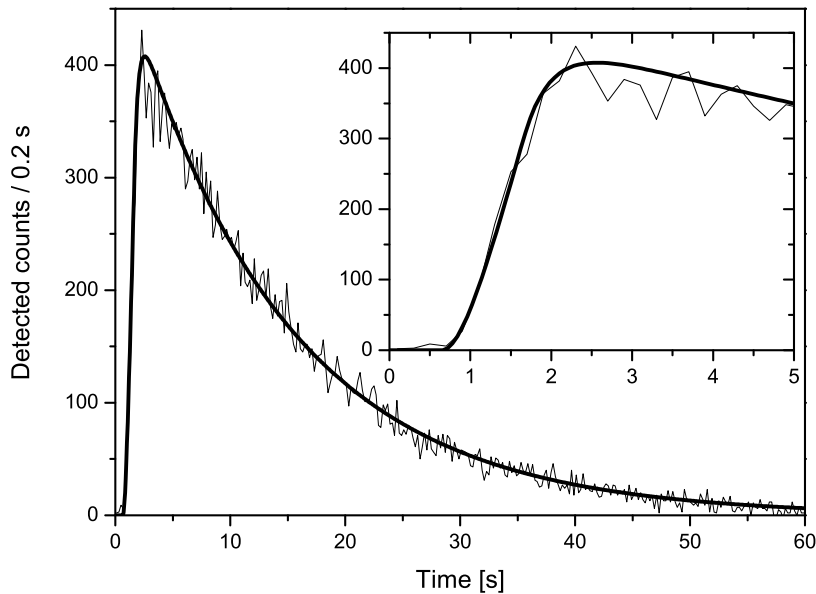
Figure 2.9: Time dependence of the counting rate of detected αdecays of ^{171,172}Os in the detector and fit from theoretical model with transport time of 1.4 s. Zero corresponds to the start of the irradiation.

Due to small leaks in the vacuum windows and of the RC and in the cooled detector panel, new gas had to be supplied from gas tanks. A leak rate of 3 ml/min was measured, corresponding to 0.2% of the total flow through the system. The leak rate served as a sensitive indicator of the extent of the damage of the vacuum windows. The gas pressure in the system, gas flow rates, as well as water and oxygen content were controlled on-line by a Labview$^{\text{TM}}$ server. The inner logic of the server allowed autonomous operation of the gas system and automatic actuation of safety valves in case of unexpected behaviour. The design and commissioning of the gas control system was carried out in the framework of this thesis.

Chapter 3

Analysis of the experimental data

"Science is the systematic classification of experience."
   — George Henry Lewes (1817–78)

The analysis of the experimental data obtained in the TUM experiments on Hs chemistry are presented in Section 3.1. The method of analysis of the overall efficiency, necessary to evaluate the experimental sensitivity, is described in Section 3.2. Because a cascade of subsequent decays is the expected decay pattern of Hs nuclei, time correlations between detected events can be used for the recognition of the characteristic decay chain patterns in α and SF background. A thorough analysis of methods to search for time-correlated chains out with background is introduced in Section 3.3.

3.1 Analysis of experimental data from TUM experiments on Hs chemistry

3.1.1 Experiments on the reaction ^{26}Mg + ^{248}Cm

Hs nuclei were produced in the 3–5n channel of the reaction ^{248}Cm(^{26}Mg, xn)$^{274-x}$Hs. In two experimental campaigns, five beam energies were used - E_{LAB} = 150, 145, 140, 136, and 130 MeV. Table 3.1 summarizes the experimental conditions at various beam energies. Due to the chemical separation, only α-lines originating from $^{172-174}$Os, ^{211}At and ^{219,220}Rn and their daughters were identified. Unfortunately, aerosol particles created

by sputtering of the target material were not completely retained by the filter resulting in a SF-background. Background α-decay events in the area of interest at α-particle energies of 8.0–9.5 MeV were attributed mainly to ^{212}Po originating from the in-flight decay of ^{220}Rn. A typical sum spectrum of all α-particles detected during the first ^{26}Mg + ^{248}Cm experimental campaign (E_{LAB} = 145, 135 MeV) on the first 25 detector pairs is presented in Figure 3.1.

E_{LAB} [MeV]	E^* [MeV]	I_{Beam} [particles]	T_{irr} [h]	N_α	N_{SF}	$n_b(\alpha\text{-SF})$ (300 s)	$n_b(\alpha\text{-}\alpha\text{-SF})$ (2×300 s)	N_2	N_3	N_4
150	54	$1.43 \cdot 10^{18}$	91	57	206	1.3	$8 \cdot 10^{-3}$	0	1	1
145	49	$1.46 \cdot 10^{18}$	139	83	68	0.4	$2 \cdot 10^{-3}$	2	5	1
140	45	$2.55 \cdot 10^{18}$	158	50	101	0.3	$3 \cdot 10^{-3}$	5	1	0
136	40	$2.02 \cdot 10^{18}$	120	62	102	0.5	$3 \cdot 10^{-3}$	5	2	0
130	36	$1.71 \cdot 10^{18}$	91	17	176	0.3	$3 \cdot 10^{-3}$	3	0	0

Table 3.1: Experimental conditions in the ^{26}Mg + ^{248}Cm experiments. E_{LAB} stands for the beam energy in LAB frame, E^* is the excitation energy, I_{Beam} is the accumulated beam integral, T_{irr} is the irradiation time in hours, N_α and N_{SF} are the numbers of measured α- ($8 \leq E_\alpha \leq 9.5$) and SF decays. $n_b(\alpha\text{-SF})$ and $n_b(\alpha\text{-}\alpha\text{-SF})$ stand for the number of expected random α-SF and α-α-SF correlations caused by the α- and SF-background. Columns N_2, N_3 and N_4 list the number of observed two-, three- and four-member correlations (α-SF, α-α-SF and α-α-α-α). The search for correlations was performed in subsequent 300 s time windows.

Based on the decay properties of ^{269}Hs reported in $[2, 3, 40, 41, 73]$ and expected decay properties of ^{270}Hs and ^{271}Hs, a decay chain was defined as an α-decay occurring in the energy range from 8.0 – 9.5 MeV followed within 300 s in the same or a neighboring detector pair (i) by an α-decay in the same energy window or (ii) by a SF. The search procedure was repeated within the chain with identical conditions until no further α-decay or SF was registered. Due to the α- and SF background, pseudo-correlated sequences can be formed with non-zero probability. Based on measured count rates the numbers of expected random correlations were calculated. The number of expected α-SF and α-α-SF pseudo-correlations caused by background are presented in Table 3.1 along with the number of detected correlations. From the comparison it is clear, that one or two of the detected α-SF correlations can be of random origin, the other correlations are caused by detection of sequences of α-decays from real decay chains. In both ex-
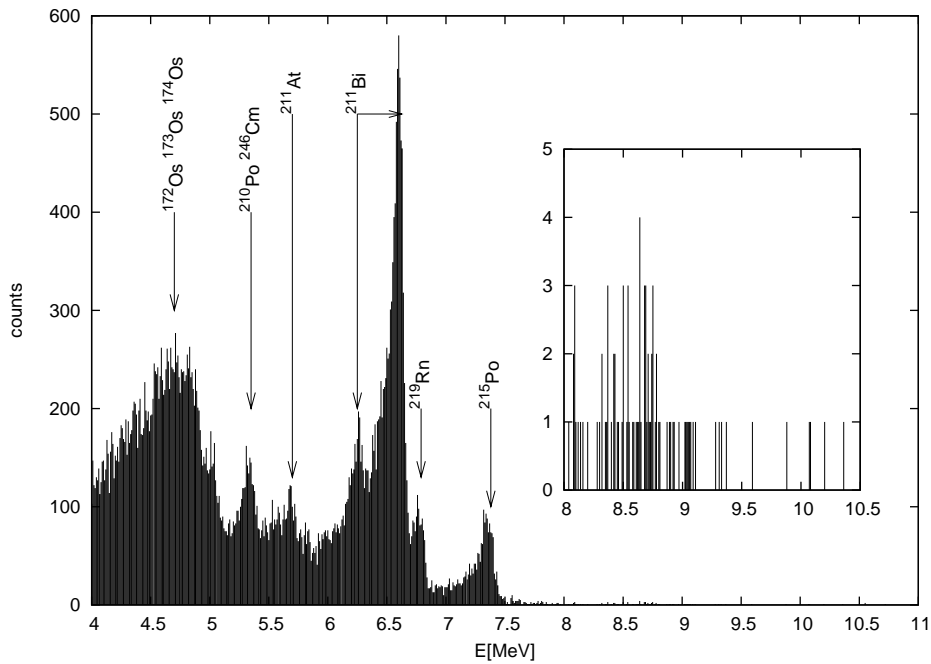
Figure 3.1: Alpha sum spectrum of the first 25 detector pairs accumulated during the first ^{26}Mg + ^{248}Cm experimental campaign (258 hours). ^{211}Bi originates mostly from α-line calibrations. Only α-lines originating from $^{172-174}$Os, ^{211}At and ^{219,220}Rn and their daughters were identified in the spectrum. α-lines originating from the α-decay of ^{246}Cm, resulting from target sputtering could not be distinguished from the decay of ^{210}Po. The area of interest is shown in the enlarged cutout. Background α-decay events in the area of interest were attributed mainly to ^{212}Po originating from the in-flight decay of ^{220}Rn.

perimental campaigns only $6 \cdot 10^{-5}$ α-α-α-SF pseudo-correlations and $2 \cdot 10^{-5}$ α-α-α-α correlations were expected from background counting rates. The analysis of the search method and evaluation of expected random correlations is presented in Section 3.3.

3.1.2   Experiment on the reaction ^{25}Mg + ^{248}Cm

In the experiment, the ^{248}Cm target was bombarded with ^{25}Mg^{4+} ions with energy of $E_{LAB} = 140$ MeV, where the maximum cross section for the $5n$ evaporation channel is predicted by HIVAP using the Reisdorf and Schädel parameters [48]. With beam intensities of 1.5 particle$\cdot\mu$A, a beam integral of $3.61 \cdot 10^{18}$ was accumulated on the target in 170 hours of irradiation. However, no α-SF or α-α-SF correlations were found in the experimental data.

3.2   Overall efficiency

The overall efficiency is defined as the probability, that a wanted evaporation residue of a nuclear reaction, is transported to the detection system and detected there. Hence, it is the product of the transport efficiency and the detection efficiency of the detection system.

3.2.1   Average transport efficiency

The transport efficiency consists of two components:

Chemical reaction and transport yield - probability, that the product of a nuclear reaction forms a volatile compound and is transported to the detector with the gas flow.

Survival probability - probability, that the species does not decay during the transport.

The chemical reaction and transport yield was estimated in previous test experiments, where α-decaying Os isotopes with short half-lives were produced under the same conditions as later in the Hs chemistry experiments. The Os yield was optimized

by changing the temperature in the recoil chamber, the temperature of the quartz filter, the He to O_2 mixing ratio and the gas flow rate. Optimal conditions found were used in the Hs chemistry experiments to achieve maximal yield. From the calculated production cross section of the nuclear reaction and from the Os yield, the efficiency of this step was estimated to be 80%.

The survival probability is clearly dependent on the half-life of the investigated Hs isotopes and can easily be calculated from the known transport time in the gas flow. The transport time was evaluated in test experiments with short-lived Os isotopes. In the first two experiments, searching for Hs isotopes with expected half-lives of 10 and 20 s seconds, a transport time of three seconds was estimated, resulting in a survival probabilities of 81% and 90%, respectively. The experiment conducted in the year 2006 was aimed at the detection of ^{268}Hs, a nuclide with a predicted half-life of 0.1–1 s [19, 28, 38, 39]. The transport line was optimized to reach the shortest transport times possible. After the optimization, a transport time of about 1.4 s was estimated, an extraordinary short value for chemical experiments.

The transport efficiency can be calculated as the product of the chemical reaction and transport yield and the survival probability. In the case of the first two experiments, transport efficiencies of 64% and 72% were reached for 10 and 20 s Hs nuclei. The calculation of the transport efficiency in case of the last experiment is half-life dependent, as no information about the half-life of ^{268}Hs is available. A more detailed calculation is presented in Section 4.4.

3.2.2 Detection efficiency of COMPACT

The two detector arrays facing each other result in a close to 4π geometry with a high efficiency for the detection of α-decays and SF of species, deposited on the active surface of the PIPS diodes. However, also inactive surfaces in the detector panel are available for adsorption of species, like the sides of the detector channel or the vacuum feedthroughs. Hence, a precise calculation of the detection efficiency is necessary to estimate the probability of an α-particle escaping a decay chain. The following assumptions were made for the calculation of the detection efficiency:

1. The probability of deposition is equal on all types of surfaces.

2. An α-particle emitted from the decaying nucleus can fly in all directions with the

same probability.

3. In a spontaneous fission of disintegration of a nucleus, the two fragments emitted by a spontaneously fissioning nucleus are flying in opposite directions under 180°.

4. If an α-particle emitted from a decaying nucleus hits the active surface of a PIPS diode, it is detected.

5. To exclude signals from α-particles that enter the detector under very shallow angles, only signals from neighbouring detectors are accepted for the detection of genetically linked decay chains.

Deposition Probability

Dimensions of the detector channel and a single PIPS diode are shown in detail in Figure 3.2. Surfaces inside the detector channel, where a deposition of a species is possible, can be divided as follows:

Active surface - species is deposited on the active surface of a PIPS diode.

Nonactive surface - a species is not deposited on the active detector surface, but an emitted particle can reach it. There are two kinds of nonactive surface in our detector channel:

- Nonactive surface of a PIPS diode.
- Side of the channel.

Dead surface - a species deposited on the dead surface cannot be detected. In our channel this corresponds to the contact place of vacuum feedthroughs. These form cavities, which the species can enter only via diffusion. The particle is considered to be lost, if it reaches the opening of the vacuum feedthrough cavity facing the detector channel. Therefore the dead surface area is equal to the areas of openings of vacuum feedthroughs.

The probability of deposition on a surface depends on the area of this surface. The probability, that a species will be lost on the dead surface is given by the area of the opening of the cavity of a vacuum feedthrough. Relative areas of all surfaces inside the detector channel per one PIPS diode are presented in Table 3.2.
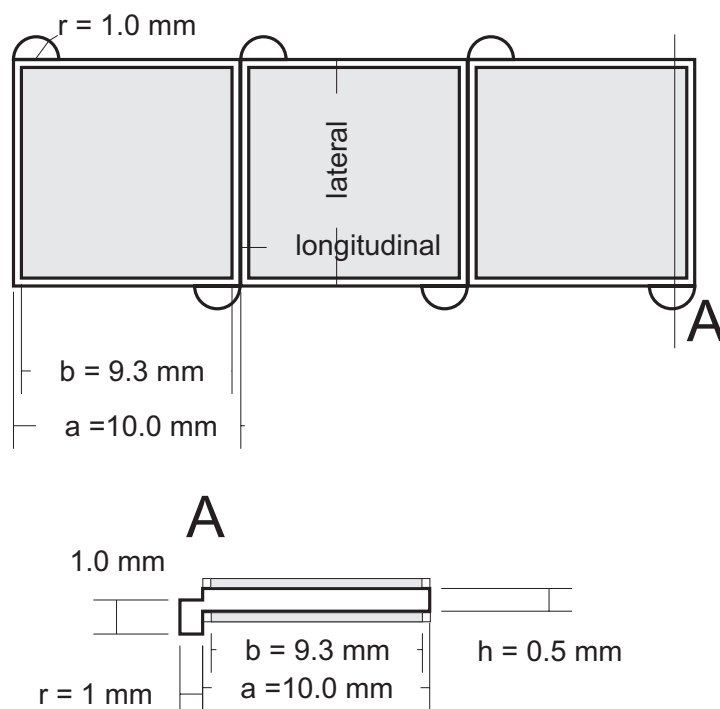
Figure 3.2: Top view & cross section view of the detector channel. Dimensions and directions, used in the calculations discussed below are shown.

	Active surface	Nonactive surface		Dead surface
		Detector	Side	
Area of surface in mm^2	86.49	13.51	4.5	0.5
Deposition probability	82.37 %	12.87 %	4.29 %	0.48 %

Table 3.2: Relative areas of different surfaces inside the detector channel per one PIPS diode and the probability of deposition on these surfaces.

Geometrical detection probability

The geometrical detection probability is the probability, that a particle emitted from a decaying species hits the active detector surface. Clearly it differs for every type of surface.

Active surface:

If a species emits an α-particle towards the surface, on which it is deposited, this

particle is detected. For particles emitted in the opposite hemisphere, the probability is calculated as a normalized integral over all possible positions and emittance angles. Integration in the 3 dimensional space is decomposed into two orthogonal directions - longitudinal and lateral, as shown in Figure 3.2.

Longitudinal direction - In longitudinal direction, particles can be detected in the detector directly opposite of the detector on which the species was deposited as well as in the neighboring detectors.

$$P_{Long} = \frac{1}{\pi b} \int_{-\frac{b}{2}}^{\frac{b}{2}} \int_{0}^{\pi} \mathrm{d}\alpha \mathrm{d}x$$

$$P_{Long} = \frac{1}{\pi b} \int_{-\frac{b}{2}}^{\frac{b}{2}} \left[\int_{\tan^{-1}\left(\frac{a+\frac{b}{2}-x}{h}\right)}^{\tan^{-1}\left(\frac{a-\frac{b}{2}-x}{h}\right)} \mathrm{d}\alpha + \right.$$

$$\left. + \int_{\tan^{-1}\left(\frac{\frac{b}{2}-x}{h}\right)}^{\tan^{-1}\left(\frac{-\frac{b}{2}+x}{h}\right)} \mathrm{d}\alpha + \int_{\tan^{-1}\left(\frac{-a+\frac{b}{2}+x}{h}\right)}^{\tan^{-1}\left(\frac{-a-\frac{b}{2}-x}{h}\right)} \mathrm{d}\alpha \right] \mathrm{d}x$$

$$P_{Long} = \frac{1}{\pi b} \int_{-\frac{b}{2}}^{\frac{b}{2}} \left[\tan^{-1}\left(\frac{a-\frac{b}{2}-x}{h}\right) - \tan^{-1}\left(\frac{a+\frac{b}{2}-x}{h}\right) + \tan^{-1}\left(\frac{-\frac{b}{2}+x}{h}\right) - \right.$$

$$\left. - \tan^{-1}\left(\frac{\frac{b}{2}-x}{h}\right) + \tan^{-1}\left(\frac{-a-\frac{b}{2}-x}{h}\right) - \tan^{-1}\left(\frac{-a+\frac{b}{2}+x}{h}\right) \right] \mathrm{d}x$$

$$P_{Long} = 93.17 \ \%$$

$$(3.1)$$

Lateral direction - In lateral direction, only α-particles reaching the opposite detector are detected.

$$P_{Lat} = \frac{1}{\pi b} \int_{-\frac{b}{2}}^{\frac{b}{2}} \left[\tan^{-1}\left(\frac{\frac{b}{2}-x}{h}\right) - \tan^{-1}\left(\frac{-\frac{b}{2}-x}{h}\right) \right] \mathrm{d}x$$

$$P_{Lat} = 86.57 \ \%$$

$$(3.2)$$

The probability to detect an α-particle emitted by the decay of a nucleus under a random angle from the active surface of the PIPS diode is:

$$P_{AD}(\alpha) = 0.5 + 0.5 * P_{Long} * P_{Lat} = 0.5 + 0.5 * 0.9317 * 0.8657 = 90.33\% \qquad (3.3)$$

As one SF fragment always hits the surface, where the species is deposited, and the other one flies in opposite direction, the geometrical detection probability for the first SF fragment is $P_{AD}(1.SFf) = 100$ % and $P_{AD}(2.SFf) = P_{Long} * P_{Lat} = 80.65$ % for the second one. Therefore, $P_{AD}(SF) = 100$ % (both fragments) is also 80.65 %.

Nonactive surface of a PIPS diode:

If a nucleus emits an α-particle towards the surface, on which it is deposited, this particle is not detected. For α-particles emitted from the surface, the probability of detection is calculated as in the case of active surface. The nonactive surface of a PIPS diode is divided into two parts - longitudinal and lateral strips. Longitudinal strips have the area of $S^{Long} = 2 * b * \frac{a-b}{2} = 6.51$ mm^2, lateral strips $S^{Lat} = 2 * a * \frac{a-b}{2} = 7$ mm^2; the surface is divided in the ratio 48.19:51.81.

Longitudinal strip - Longitudinal direction The calculation is the same as for the active surface - longitudinal direction.

$$P_{Long}^{Long} = 93.17 \text{ \%} \qquad (3.4)$$

Longitudinal strip - Lateral direction Since α-particles that are emitted under very shallow angles are neglected, only the two opposite detectors are taken into account.

$$P_{Lat}^{Long} = \frac{2}{\pi(a-b)} \int_0^{\frac{a-b}{2}} \left[\tan^{-1}\left(\frac{\frac{a-b}{2} - x}{h} \right) - \tan^{-1}\left(\frac{\frac{a+b}{2} - x}{h} \right) \right] \mathrm{d}x$$

$$P_{Lat}^{Long} = 41 \text{ \%}$$

$$(3.5)$$

Lateral strip - Longitudinal direction

$$P_{Long}^{Lat} = \frac{2}{\pi(a-b)} \int_{-\frac{a-b}{2}}^{\frac{a-b}{2}} \left[\tan^{-1}\left(\frac{\frac{a+b}{2} - x}{h} \right) - \tan^{-1}\left(\frac{\frac{a-b}{2} - x}{h} \right) \right] \mathrm{d}x \tag{3.6}$$

$$P_{Long}^{Lat} = 60.05 \ \%$$

Lateral strip - Lateral direction The calculation is the same as for the active surface - lateral direction.

$$P_{Lat}^{Lat} = 86.57 \ \% \tag{3.7}$$

Thus the final geometrical probabilities for species deposited on the nonactive surface of a PIPS diode are:

$$P_{NAD}(\alpha) = 0.5 * (0.4819 * P_{Long}^{Long} * P_{Lat}^{Long} + 0.5181 * P_{Lat}^{Long} * P_{Lat}^{Lat}) = 22.67 \ \%$$

$$P_{NAD}(1.SFf) = 0 \ \%$$

$$P_{NAD}(2.SFf) = (0.4819 * P_{Long}^{Long} * P_{Lat}^{Long} + 0.5181 * P_{Lat}^{Long} * P_{Lat}^{Lat}) = 45.37 \ \% \tag{3.8}$$

Nonactive surface - side of channel:

Longitudinal direction - The calculation is similar as for the active surface, only the integration limits are $-\frac{a}{2}, \frac{a}{2}$.

$$P_{Long} = 90.91 \ \% \tag{3.9}$$

Lateral direction - An α-particle from the decay of a nucleus can be detected in either one of the two adjacent PIPS diodes.

$$P_{Lat} = \frac{2}{\pi h} \int_{-\frac{h}{2}}^{\frac{h}{2}} \left[\tan^{-1}\left(\frac{b + \frac{a-b}{2}}{\frac{h}{2} - x} \right) - \tan^{-1}\left(\frac{\frac{a-b}{2}}{\frac{h}{2} - x} \right) \right] \mathrm{d}x \tag{3.10}$$

$$P_{Lat} = 34.69 \ \%$$

therefore, the final geometrical detection probability for the species deposited on the side of the channel:

$$P_{NAS}(\alpha) = 0.5 * P_{Long} * P_{Lat} = 15.77 \%$$
$$P_{NAS}(1.SFf) = 0 \%$$
$$P_{NAS}(2.SFf) = 31.54 \%$$

(3.11)

Dead surface:

The probability, that an α-particle emitted by a decaying nucleus adsorbed on a dead surface hits an active surface of a PIPS diode is assumed to be equal to zero.

Summary of geometrical detection probability:

The calculated geometrical probabilities are summarized in the Table 3.3.

	Active surface	Nonactive surface		Dead surface
		Detector	Side	
$P(\alpha)$	90.33 %	22.67 %	15.77 %	0 %
$P(1 \times SFf)$	100 %	45.37 %	31.54 %	0 %
$P(2 \times SFf)$	80.65 %	0 %	0 %	0 %

Table 3.3: Geometrical probabilities of different surfaces

Detection efficiency

The detection efficiency is calculated from deposition probabilities (Table 3.2) and geometrical probabilities (Table 3.3). The probability to detect an α-particle, emitted from a species deposited somewhere in the detector channel, is 78%. The probability to detect both fragments of a spontaneous fission decay is 66%, to detect at least one fragment is 89%. The detection probabilities for an α-α-SF decay chain are presented in Table 3.4. The abbreviation SFf stands for one fission fragment. The detection probabilities for an α-SF decay chain are presented in Table 3.5.

	Active surface	Nonactive surface		Dead surface	Whole detector
		Detector	Side		
$\alpha - \alpha - 2 \times SFf$	65.81 %	0 %	0 %	0 %	54.21 %
$\alpha - \alpha - 1 \times SFf$	15.79 %	2.33 %	0.78 %	0 %	13.34 %
$\alpha - \alpha$	0 %	2.81 %	1.70 %	0 %	0.43 %
$\alpha - 2 \times SFf$	14.09 %	0 %	0 %	0 %	11.61 %
$\alpha - 1 \times SFf$	3.38 %	15.91 %	8.38 %	0 %	5.19 %
α	0 %	19.15 %	18.19 %	0 %	3.24 %
$2 \times SFf$	0.75 %	0 %	0 %	0 %	0.62 %
$1 \times SFf$	0.18 %	27.13 %	22.38 %	0 %	4.6 %
nothing	0 %	32.67 %	48.57 %	100 %	6.76 %

Table 3.4: Detection probabilities for a α-α-SF decay chain.

	Active surface	Nonactive surface		Dead surface	Whole detector
		Detector	Side		
$\alpha - 2 \times SFf$	72.85 %	0 %	0 %	0 %	60.01 %
$\alpha - 1 \times SFf$	17.48 %	10.29 %	4.97 %	0 %	15.93 %
α	0 %	12.38 %	10.80 %	0 %	2.06 %
$2 \times SFf$	7.80 %	0 %	0 %	0 %	6.42 %
$1 \times SFf$	1.87 %	35.08 %	26.57 %	0 %	7.19 %
nothing	0 %	42.25 %	57.66 %	100 %	8.38 %

Table 3.5: Detection probabilities for a α-SF decay chain.

From the values in Tables 3.4 and 3.5 can be concluded, that the probability to identify an α-α-SF decay chain as a complete one (α-α-$2 \times$ SFf or α-α-$1 \times$ SFf is about 68% and to detect it as an at least two member correlation is about 85%. An α-SF chain will be identified in about 76% of all cases as complete.

3.2.3 Expected incomplete chains

As a valid decay chain, only a correlation of an α-particle with another α-particle or SF fragment is considered. However, no α-α correlations without following SF were

observed in the experimental data. In 17% of the cases, one α-particle of a α-α-SF decay chain will be missed. If we take into account only identified correlations, the expected ratio of the number of incomplete decay chains (two-member correlations) to the number of all identified correlations originating from α-α-SF chains is 20%. The probability distribution to detect x complete chains out of n with the probability p, follows the binomial distribution:

$$P(x) = \binom{n}{x} p^x (1-p)^{n-x} = \frac{n!}{x!(n-x)!} p^x (1-p)^{n-x} \qquad (3.12)$$

The probabilities, that out of 10 decay chains x will be detected complete is presented in the Table 3.6. With the highest probability 2 decay chains will be detected as incomplete.

x	Probability
0	1.02×10^{-5} %
1	4.10×10^{-4} %
2	7.37×10^{-3} %
3	7.86×10^{-2} %
4	0.55 %
5	2.64 %
6	8.81 %
7	20.13 %
8	30.20 %
9	26.84 %
10	10.74 %

Table 3.6: Probability, that x out of 10 decay chains will be detected as complete, when the probability to detect a complete chain is $p = 80\%$.

Overall efficiency

The overall efficiency is calculated from the transport efficiency and the detection efficiency in COMPACT. The overall efficiency for detection of ^{269}Hs ($T_{1/2} \sim 10$ s) in the

^{26}Mg + ^{248}Cm experiments is 55%, for detection of ^{270}Hs (T$_{1/2}$ $\sim$ 20 s) 55%, and for detection of ^{271}Hs (T$_{1/2}$ $\sim$ 10 s) 55% in case of an α-decay of ^{267}Sg and 49% in case of an SF-decay of ^{267}Sg. These overall efficiencies are significantly higher than those of kinematic separators for this type of reaction, which typically are $\sim$ 20 $-$ 30% and allow to measure products from a nuclear reaction with a production cross section on the level of a few picobarns. Conclusions on the overall efficiency in the ^{26}Mg + ^{248}Cm experiment to produce ^{268}Hs are presented in Section 4.4.

3.3 Time correlation search

Because a cascade of subsequent decays is the expected decay pattern of Hs nuclei, time differences between detected events can be used for the recognition of the characteristic decay chain patterns in α and SF background. The background is considered to be stochastic and hence it can be treated mathematically by the use of a Poisson distribution. However, the possibility, that random background of uncorrelated events could simulate a correlated decay sequence has to be carefully considered.

The calculation of the number of expected pseudo-correlated background events is determined by correlation search methods and parameters. Two correlation search methods can be found in the literature:

Subsequent time windows - After a start signal (detection of the first potential member of a decay chain), a time window is opened. If in the time window a correlated event is observed, a next window is opened, starting immediately after the most recently found event, to search for an another correlated event. The procedure is repeated, until no more events are detected. This procedure was used e.g. in [77].

Single time window - After a start signal (detection of the first potential member of a decay chain), a time window of defined length is opened and correlated events within this window are searched for. This procedure was used for instance in [2]

In the following these two methods are compared in terms of the number of expected random correlations and search efficiency for a real decay chain. For comparison, a calculation with real experimental data is presented. The data were acquired during the first experiment conducted in the year 2004 during an irradiation with a projectile

energy of $E_{LAB} = 145$ MeV [78]. In the irradiation, eight correlated chains were observed, attributed to the decay of Hs nuclei. One of these was a correlation of four α-decays, five of them were α-α-SF correlations and two were α-SF correlations. However, for purposes of the following calculation, all detected events are concidered as of purely random origin. Experiment parameters are summarized in Table 3.7.

Parameter	Value	Description
T_{exp}	138.76 h	Total time of irradiation
N_α^{Total}	83	Number of detected α-particles
N_{SF}	68	Number of detected SF events
N_{CD}	6	Number of PIPS diodes for pos. corr.
N_D	50	Total number of PIPS diodes
t_c	300 s	Correlation time window

Table 3.7: Set of parameters from data obtained from an irradiation with a projectile energy of $E_{LAB} = 145$ MeV

The COMPACT detector consists of two arrays of 32 PIPS diodes, but based on the known volatility of HsO_4 only the first 25 diode pairs were used for data analysis. Events are searched for not only time correlated, but also position correlated. Only events on the same or the neighbouring two detector pairs are considered to be position correlated. Hence, the average number of α-particles, which are in position correlation to a detected SF decay is reduced to:

$$N_\alpha = \frac{N_{CD}}{N_D} \times N_\alpha^{Total} \tag{3.13}$$

Mean count rates of α-decays and SF-events, are defined as:

$$\lambda_\alpha = \frac{N_\alpha}{T_{exp}}, \text{ and } \qquad \lambda_{SF} = \frac{N_{SF}}{T_{exp}} \tag{3.14}$$

3.3.1 Correlation search in subsequent time windows

For calculation of the number of expected random correlations, when the correlation is searched in subsequent time windows, several methods can be employed.

Method proposed in [77]:

This method is described in detail in reference [77]. The number of expected random correlations n_b for K different event groups is:

$$n_b = T_{exp} \frac{\prod\limits_{i=1}^{K} \lambda_i}{\left(\sum\limits_{i=1}^{K} \lambda_i \right)^{K-1}} \prod_{j=1}^{K-1} \left(1 - e^{-\sum_{i=1}^{K} \lambda_i \Delta t_{j,j+1}} \right) \tag{3.15}$$

where λ_i is the mean counting rate for event group i and Δt is the time interval between successive events. In our experiment, for an α-SF correlation $K = 2$ (α and SF).

$$n_b = T_{exp} \frac{\lambda_{SF} \cdot \lambda_\alpha}{\lambda_{SF} + \lambda_\alpha} \left[1 - e^{-t_c(\lambda_{SF} + \lambda_\alpha)} \right] \tag{3.16}$$

For an α-α-SF correlation ($K = 3$), where the α-particles have free order, the following formula was proposed:

$$n_b = T_{exp} \frac{\lambda_{SF} \cdot \lambda_\alpha^2}{(\lambda_{SF} + \lambda_\alpha)^2} \left[1 - e^{-t_c(\lambda_{SF} + \lambda_\alpha)} \right]^2 \tag{3.17}$$

From the analysis of equation (3.17) it is evident, that an exponential distribution of the time delay between two random events is expected. The two groups of events, α-decays and SF are considered to be independent and therefore they form two independent Poisson distributions in stochastic background. Thus the distance between two random events can be expressed using the Poisson distribution.

Poisson distribution method:

In this method is assumed, that the time delay between two random events can be calculated according to the Poisson distribution. The number of expected random correlations n_b is as follows:

$$n_b = T_{exp}\lambda_{SF} \prod_{i=1}^{K} \left(\lambda_i \cdot \Delta t_{i,i+1} e^{-\lambda_i \cdot \Delta t_{i,i+1}} \right) \tag{3.18}$$

where the variables are explained above. For α-SF correlations:

$$n_b = T_{exp}\lambda_{SF}(\lambda_\alpha \cdot t_c)e^{-\lambda_\alpha \cdot t_c} \tag{3.19}$$

For α-α-SF correlations with two indistinguishable α-particles:

$$n_b = T_{exp} \cdot \lambda_{SF}(\lambda_\alpha \cdot t_c)^2 e^{-2\lambda_\alpha \cdot t_c} \tag{3.20}$$

The Poisson distribution method gives the most precise calculations of the number of expected random correlations. However, a further simplification is possible in case of a low background counting rate.

Simplified method:

If the condition $\sum_{i=1}^{K} \lambda_i \Delta t_{i,i+1} \ll 0$ is fulfilled, n_b can be approximated as:

$$n_b = T_{exp} \prod_{i=1}^{K} \lambda_i \prod_{i=1}^{K-1} \Delta t_{i,i+1} \tag{3.21}$$

In case of α-SF correlations:

$$n_b = T_{exp}\lambda_{SF}\lambda_\alpha t_c \tag{3.22}$$

For α-α-SF correlations with two indistinguishable α-particles:

$$n_b = T_{exp}\lambda_{SF}(\lambda_\alpha t_c)^2 \tag{3.23}$$

Monte Carlo simulation:

To obtain an independent verification of the above mentioned methods for the calculation of n_b, a Monte Carlo simulation was carried out.

Comparison of the results obtained by different methods:

With the set of parameters presented in Table 3.7 the number of expected random correlations was calculated using all the methods discussed above. Results are presented in Table 3.8.

Method	α-SF (300 s)	α-α-SF (2×300 s)
Monte Carlo simulation	$4.03 \pm 0.02 \times 10^{-1}$	$2.42 \pm 0.16 \times 10^{-3}$
Method proposed in [77]	3.97×10^{-1}	2.32×10^{-3}
Simple calculation	4.07×10^{-1}	2.43×10^{-3}
Poisson distribution	4.04×10^{-1}	2.40×10^{-3}

Table 3.8: Comparison of different methods for calculating the number of expected random correlations. A set of parameters from a real measurement (Table 3.7) is used.

All methods described above deliver comparable results for the analysis of real experimental data, as can be seen from Table 3.8. Use of the simple method is well motivated by this comparison, however, attention has to be payed, that the background counting rate remains low. The Poisson distribution method proved to give the most precise results, in agreement with expectations.

3.3.2 Search efficiency of the subsequent time windows method

As the number of expected random correlations can be calculated precisely, the question remains, what the optimal length of time windows is, in which almost all real decay

chains are found, but which contain only a small number of purely randomly correlated patterns formed by background. In experiments the real data form decay sequences, so that the time delay between the decay of chain members follows an exponential decay distribution. In the case of known half-lives of the members of a decay chain the probability to observe the decay chain in subsequent time windows can be calculated as:

$$P_{subseq} = \prod_{i=1}^{K} \left(1 - e^{-\Delta t_{i,i+1} \frac{ln(2)}{(T_{1/2})_i}} \right) \qquad (3.24)$$

where K is the number of chain members after the starting signal, $\Delta t_{i,i+1}$ is the time window for the search of member i and $(T_{1/2})_i$ is half-life of member i. The first α-decay is used as the starting signal for the correlation search in our chemical experiment, because no information on the time of formation of Hs atom is available. Resulting efficiencies for the search of decay chains in our experiments using 300 s time windows (as used in the actual data analysis) are shown in Table 3.9. A crucial point of the correlation search is the choice of a suitable time window. The choice of 300 s time window for correlation search in our experiment is well-founded by the observed decay properties of ^{267}Sg and ^{261a}Rf, which have half-lives that are relatively long in comparison to other decay products of $^{269-271}$Hs, resulting in only 92% and 93% search efficiency for the ^{271}Hs and ^{269}Hs decay chains, respectively. Clearly, a different time window length would be optimal for searches of different types of decay chains, but a single time window length (300 s) was used in our experiment for simplicity. Also a different choice of window lengths for decay members with different half-lives, that further decreases the chance of false identification of correlated decay chains of random origin, was not utilized.

3.3.3 Correlation search in a single time window

The search for correlated events within a single time window was used e.g. in [2]. The number of expected random correlations can be calculated as:

$$n_b(x) = \frac{\prod_{i=1}^{K} \lambda_i}{\lambda^K} \cdot n \binom{n-1}{x} \left(\frac{t_c}{T_{exp}} \right)^x \left(1 - \frac{t_c}{T_{exp}} \right)^{n-1-x}, \qquad (3.25)$$

Decay	$T_{1/2}$		Decay chain search efficiency	
	1st	2nd	I. $(2 \times 300$ s$)$	II $(300$ s$)$
^{269}Hs $\rightarrow$ ^{265}Sg $\rightarrow$ ^{261a}Rf	15 s	78 s	0.93 [0.93]	0.91 [0.91]
^{269}Hs $\rightarrow$ ^{265}Sg $\rightarrow$ ^{261b}Rf	15 s	2.5 s	$(1 - 1 \times 10^{-6})$	$(1 - 1.1 \times 10^{-6})$
			$[(1 - 1 \times 10^{-6})]$	$[(1 - 1 \times 10^{-6})]$
^{271}Hs $\rightarrow$ ^{267}Sg $\rightarrow$ ^{263}Rf	84 s	8.3 s	0.92 [0.92]	0.91 [0.91]

Table 3.9: Comparison of decay chain search efficiencies for both methods : I. - with subsequent 2×300 s windows and II. - within one 300 s window. Results for a Monte Carlo simulation are presented in parenthesis. For calculation purposes, real half-lives determined from the Hs chemistry experiments for Hs decays were used.

where $n = N_{SF} + N_\alpha$ is the sum of all events, $\lambda = n/T_{exp}$ is the total background counting rate and x is number of correlated events, besides the above defined variables. Using this formula, the expected number of x-member random correlations can be calculated. In case of α-SF correlations:

$$n_b = \frac{\lambda_{SF}\lambda_\alpha}{(\lambda_{SF} + \lambda_\alpha)^2} \cdot n(n-1)\left(\frac{t_c}{T_{exp}}\right)\left(1 - \frac{t_c}{T_{exp}}\right)^{n-2} \tag{3.26}$$

For α-α-SF correlations with two indistinguishable α-particles:

$$n_b = \frac{\lambda_{SF}\lambda_\alpha}{(\lambda_{SF} + \lambda_\alpha)^2} \cdot \frac{n(n-1)(n-2)}{2}\left(\frac{t_c}{T_{exp}}\right)^2\left(1 - \frac{t_c}{T_{exp}}\right)^{n-3} \tag{3.27}$$

As in the case of subsequent time windows, a Monte Carlo simulation was carried out. The resulting values of n_b for the set of parameters from Table 3.7 using the one window search method are presented in Table 3.10. Although the agreement between calculation and MC simulation is generally good, the calculated results are about 10% lower than those of the MC simulation.

Method	α-SF (300 s)	α-α-SF (300 s)
MC simulation	$4.04 \pm 0.02 \times 10^{-1}$	$1.23 \pm 0.10 \times 10^{-3}$
Calculation	3.84×10^{-1}	1.12×10^{-3}

Table 3.10: Comparison of different methods for the calculation of the number of expected random correlations. A set of parameters from a real measurement (Table 3.7) is used.

3.3.4   Search efficiency of the single time window method

The calculation of the search efficiency in case of a single time window is more complicated than in case of subsequent time windows. Multiple decays can be detected within a fixed time interval, but these decays can occur from nuclei that have different half-lives. The probability to find a K-member decay chain with decay constants $\lambda_1, \ldots, \lambda_K$ in the interval τ can be calculated as:

$$P_{one} = \left(\prod_{i=1}^{K} \lambda_i \right) \int_0^{\tau} dt_1 \int_{\tau - t_1}^{\tau} dt_2 \cdots \int_{\tau - (\sum_{i=1}^{K} t_i)}^{\tau} dt_K \; e^{-\sum_{i=1}^{K} t_i \lambda_i} \tag{3.28}$$

For an α-α-SF decay chain, often found in our experiments, the solution can be simplified:

$$P_{one} = \lambda_1 \int_0^{\tau} e^{-t\lambda_a} \left(1 - e^{-(\tau - t)\lambda_2} \right)$$
$$P_{one} = 1 - \frac{1}{\lambda_2 - \lambda_1} \left[\lambda_2 e^{-\tau\lambda_1} - \lambda_1 e^{-\tau\lambda_2} \right] \tag{3.29}$$

where all variables are described above. Search efficiencies calculated using this formula are presented in Table 3.9 for comparison.

3.3.5   Conclusion on correlation search methods

Two methods were described and throughly analyzed - correlation search in one time window and correlation search in subsequent time windows. Both methods proved to be useful, when proper time window lengths are used. The time window length is a critical parameter in both cases and has to be chosen carefully, to make an optimal trade-off between search efficiency and number of expected random correlations. As no common priorities can be given for every possible experiment, equations for search efficiency calculations and expected number of random correlations are presented here in detail, so an optimal time window for every future experiment can be found easily. In TUM experiments on Hs chemistry the method of search in subsequent windows with a fixed time window length of 300 s was chosen. Correlation search efficiencies for decay chains detected in the Hs experiments are presented in Table 3.9, numbers of expected random correlations for every irradiation are given in Table 3.1.

Chapter 4

Results and discussion

"The most exciting phrase to hear in science, the one that heralds new discoveries, is not 'Eureka!' ('I found it!') but rather 'hmm . . . that's funny. . . '."

— Isaac Asimov (1920-1992)

4.1 Decay properties of ^{269}Hs, ^{270}Hs, ^{271}Hs and their daughters

The data analysis revealed 26 correlated decay chains in the first 25 detector pairs - 15 during the first experimental campaign at beam energies of 145 and 136 MeV and 11 during the second campaign at energies of 150, 140 and 130 MeV. Decay chains from the first campaign are listed in Table 4.1, decay chains from the second campaign are presented in Table 4.2.

4.1.1 Decay chains attributed to ^{269}Hs

At a beam energy of 145 MeV mainly production of ^{269}Hs in the $5n$ evaporation channel is expected [2, 3]. The decay of ^{269}Hs has been observed previously in several different experiments [2, 3, 40, 41, 73]. In all previously performed experiments ^{269}Hs decayed by α-particle emission followed by α-decay of ^{265}Sg to ^{261}Rf which decayed by SF or by emission of an α-particle ($E_\alpha = 8.5$ MeV, $b_{SF} \sim 40\%$, $T_{1/2} = 4$ s). For ^{261}Rf, a second

No.	E_{beam}	E_1	E_2	Δt_2	E_3	Δt_3	E_4	Δt_4	Assignment
1	145	8.93 (16T)	8.69 (16B)	32.5 s	8.29 (16T)	32.1 s	8.29 (17B)	2.50 s	^{269}Hs
2	145	9.06 (13B)	8.68 (14T)	85.6 s	93 (14T)	4.44 s			^{269}Hs
3	145	9.11 (1B)	8.68 (1B)	2.48 s	67/13 (1T/1B)	7.09 s			^{269}Hs
4	145	8.91 (15B)	8.65 (15B)	6.75 s	29 (15T)	6.69 s			^{269}Hs
5	145	9.03 (18T)	8.60 (18T)	7.70 s	111/26 (18T/19B)	6.42 s			^{269}Hs
6	145	8.92 (19B)	8.72 (19T)	6.82 s	90/101 (19T/19B)	1.29 s			^{269}Hs
7	145	8.35 (22B)	38 (22B)	116 ms					no assignment
8	145	8.85 (14T)	100/74 (14T/13B)	1.62 s					^{270}Hs
9	136	9.08 (15B)	8.71 (15T)	8.70 s	100/74 (15T/16B)	580 ms			^{269}Hs
10	136	9.10 (14T)	80/90 (14T/13B)	96.0 s					^{271}Hs
11	136	8.90 (12T)	89/55 (12T/11B)	49.6 ms					^{270}Hs
12	136	8.92 (5T)	106/82 (5T/5B)	449 ms					^{270}Hs
13	136	8.88 (19T)	96/110 (19T/19B)	444 ms					^{270}Hs
14	136	9.30 (7T)	8.20 (7T)	149 s	89/95 (7T/7B)	12.0 s			^{271}Hs
15	136	8.67 (9T)	117/102 (9T/9B)	306 ms					no assignment

Table 4.1: Correlated decay chains from the first experimental campaign. Given are the number of the chain, the beam energy at which it was observed, energies of individual events (E_1 to E_4), the observed lifetimes of the daughter nuclei (Δt_2–Δt_4), and the assignment of the chain. The detector number in which an event was observed is given in parenthesis, "T" stands for "top detector" and "B" for "bottom detector". Energies are given in MeV, fission fragment energies are not corrected for pulse height defect.

No.	E_{beam}	E_1	E_2	Δt_2	E_3	Δt_3	E_4	Δt_4	Assignment
16	150	9.18 (14B)	8.62 (14T)	10.9 s	8.51 (14B)	4.89 s	8.24 (14T)	20.8 s	^{269}Hs
17	150	9.13 (12B)	8.68 (12T)	7.61 s	79/88 (12T/12B)	2.25 s			^{269}Hs
18	140	8.61 (10B)	83/84 (10T/10B)	3.35 s					^{265}Sg[a]
19	140	9.11 (10T)	8.63 (11B)	52.0 s	75 (10T)	3.04 s			^{269}Hs
20	140	[9.22 (11B)][b]	8.47 (16B)	[12.3 s][b]	84/120 (16T/16B)	128 ms			^{269}Hs
21	140	8.76 (20B)	58/61 (19T/20B)	275 ms					^{270}Hs
22	140	8.81 (16B)	92/111 (16T/16B)	271 ms					^{270}Hs
23	140	9.14 (12T)	69 (12T)	47.9 s					^{271}Hs
24	130	9.16 (24T)	26 (25B)	142 s					^{271}Hs
25	130	9.02 (16B)	89/68 (15T/15B)	30.4 s					^{271}Hs
26	130	9.23 (20T)	15/83 (20T/19B)	264 s					^{271}Hs

[a]Incomplete (α)-α-SF chain from ^{269}Hs.
[b]First α-particle is not position correlated.

Table 4.2: Correlated decay chains from the second experimental campaign. Header symbols are explained in Table 4.1.

isomeric state is known (E_α = 8.28 MeV, $b_{SF} \leq$ 10%, $T_{1/2}$ = 78 s) [57,58]. The 78 s state is denoted as ^{261a}Rf and the 4 s state as ^{261b}Rf in this work. In [2,3], two decay chains were tentatively assigned to ^{270}Hs based on the previously reported decay properties of ^{266}Sg [56,60] and ^{262}Rf [59]. However, this tentative assignment was not conclusive, as the reported ^{270}Hs decay chains consisting of α-α-SF decay sequences were similar to the ones assigned to ^{269}Hs.

Chains No. 1–6, 9, 16, 17 and 19 exhibit decay properties similar to those observed in ref. [2,3,40,41,73] for the decay of ^{269}Hs. Decay chains No. 1–6 were observed at a beam energy of 145 MeV, where the maximum cross section of the $5n$ channel is expected. Chains No. 16 and 17 were detected at a beam energy of 150 MeV, where the $5n$ evaporation channel is expected to be dominant and other channels are significantly suppressed. Chain No. 19 was detected at a beam energy of 140 MeV and chain No. 9 at 136 MeV. No such decay chains were detected at a beam energy of 130 MeV, where the predicted production cross section for the $5n$ channel is lower than the experimental sensitivity. The first α-decay of these chains with energies of 8.95 and 9.13 MeV is attributed to the decay of ^{269}Hs. The energies of the second α-decay, attributed to ^{265}Sg, have a narrow distribution with a mean value of 8.69 ± 0.04 MeV. The α-decay energies and lifetimes, detected in chain No. 1 fit well to the known α-decay energies of ^{261a}Rf and ^{257}No [35], the α-decay energies and lifetimes, detected in chain No. 16 agree well with the known properties of ^{261b}Rf decay. Hence these decay chains are attributed to the decay of ^{269}Hs. It is noteworthy, that this is the first case in which a decay chain from ^{271}112 or ^{269}Hs populated the long-lived isomeric state of ^{261a}Rf.

In chain No. 18, an α-SF correlation was observed. The energy of the α-particle was 8.61 MeV, close to the known α-decay energy of ^{265}Sg. SF followed after 3.35 s, in agreement with the decay properties of the shorter-lived isomeric state of ^{261b}Rf. Because it can be expected to miss one α-particle in one or two chains with 55% probability, this chain is also attributed to the decay of ^{269}Hs.

4.1.2   Decay chains attributed to ^{270}Hs

Chains No. 8, 11–13, 21 and 22 exhibit a narrow distribution of α-particle energies with $E_\alpha = 8.88 \pm 0.05$ MeV. They were terminated by SF with an average lifetime of ~ 0.5 s. This sequence is different from all known decay patterns. As the detection efficiency for an α-particle is 80%, there is a less than 0.1% probability that these observed α-SF chains are incomplete α-α-SF ones, where always the same α-particle was missed.

Three chains (No. 11–13) were detected at the beam energy of 136 MeV at the expected maximum of the $4n$ evaporation channel. Two chains (No. 21 and 22) were detected at 140 MeV and chain No. 8 at 145 MeV, but no similar chains were measured at energies of 150 or 130 MeV, where $5n$ or $3n$ channel are expected to dominate, respectively. Therefore these chains should be attributed to the new isotope ^{270}Hs and its daughter ^{266}Sg, synthesized in the $4n$ evaporation channel. From the measured α-particle energy, $Q_\alpha = 8.99 \pm 0.05$ MeV for ^{270}Hs was derived. Several theoretical calculations of Q_α of ^{270}Hs have been performed and most of them are in agreement with our measured data, e.g., $Q_\alpha = 8.69$ MeV [19]; $Q_\alpha = 8.83$ MeV [39]; $Q_\alpha = 8.87$ MeV [38,33], $Q_\alpha = 8.90$ MeV and $Q_\alpha = 9.54$ MeV [79] (two different models), and $Q_\alpha = 9.13$ MeV [26]. The partial α-decay half-life of ^{266}Sg is predicted as $T_\alpha = 48$ min [39] and $T_\alpha = 4.5$ min [38] while that for SF is predicted as $T_{SF} = 58$ s [80] and $T_{SF} = 100$ μs [81] suggesting SF as the likely decay mode, even if the longest calculated T_{SF} is correct. The assignment of our experimental findings is in contradiction to the interpretation of earlier works, where ^{266}Sg was reported to decay by α-particle emission with a half-life of a few tens of seconds [56,60,82,83,84]. An earlier Hs chemistry experiment [2,3] reported indications for ^{270}Hs based on these decay properties of ^{266}Sg. However, in the experiment [56] it was not possible to measure lifetimes of Sg isotopes and SF of ^{266}Sg could not be distinguished from long-lived SF background. Sg chemistry experiments [60,82,83,84] could only detect isotopes with $T_{1/2} > 1$ s based on α-α and α-SF correlations. Single SF decays could not be unambiguously attributed to Sg isotopes. The α-SF chains assigned to ^{266}Sg in [60,82,83,84] originated most probably from ^{265}Sg – ^{261b}Rf chains. ^{261b}Rf was unknown at that time. Two chains that were tentatively assigned to ^{270}Hs in [2,3] originated with large probability from ^{269}Hs. SF decay of ^{266}Sg with $T_{1/2} = 359$ ms is not in contradiction with the data of any previous experiment.

4.1.3 Decay chains attributed to ^{271}Hs

The decay chains No. 10, 14, and 23–26 are α-SF or α-α-SF correlations, where the decay of the second member follows after tens of seconds. Three of these chains (No. 24–26) were detected at the beam energy of 130 MeV, below the expected maximum of the $4n$ and definitely below the energy where significant contribution of the $5n$ channel is expected. Two decay chains, No. 10 and 14, were detected at 136 MeV and the decay chain No. 23 at 140 MeV. No similar decay chains were detected at 150 or 145 MeV, where the predicted cross section for the $3n$ channel is lower than the sensitivity of the

experiment. Because the decay chains differ from those, attributed to ^{269}Hs and ^{270}Hs, created in the $5n$ and $4n$ channels, respectively, and because the maximum production cross section is at the energy, where the $3n$ channel is expected to dominate, these decay chains should be attributed to the decay of ^{271}Hs created in the $3n$ evaporation channel. The first member of these chains decays via α-decay with energies of 9.02–9.30 MeV. Taking into account our detection efficiency and the high energy of the α-particles, the α-decay in these chains should be attributed to the decay of Hs nuclei. Three of these chains are terminated by SF of the second member, in chain No. 14 an α-decay of the second member with an energy of the α-particle of 8.20 MeV was detected. The measured lifetime for this Sg isotope points to a longer partial lifetime for the α-decay. Such an increased stability and long SF and α-decay lifetimes are expected close to the closed shell at $N = 162$. Taking into account the long α-decay half-life for ^{267}Sg, supported by the low energy of the α-particle detected, SF and α-decay half-lives may become sufficiently similar so that branching into both decay modes can be expected. The large difference of the α-decay energies of ^{271}Hs and ^{267}Sg is due to the crossing of the $N = 162$ neutron shell. Consequently, the daughter nuclide ^{267}Sg exhibits an alpha decay branch. In chain No. 14, ^{263}Rf fissioned spontaneously 12 s after the decay of ^{267}Sg. ^{263}Rf has been reported from previous experiments [85, 86, 87], where SF decays with half-life of ~ 11 minutes were measured. The half-life of 8 s derived from our experiment is significantly lower than 11 m, however, only one event has been observed, which makes the half-life calculation inconclusive.

4.1.4 Decay chains without unambiguous attribution

In chain No. 15 an α-SF correlation was observed similar as in chains No. 8, No. 11–13, but the α-particle energy is lower. This chain can be explained either as the decay of ^{270}Hs (with a low α-particle energy) or as a decay of ^{265}Sg after missing the α-particle from ^{269}Hs. No unambiguous attribution can be made. For cross section calculations this chain was tentatively attributed to ^{270}Hs.

In chain No. 7 an unusually low α-particle energy was detected and only one fragment from SF. This can be explained by the deposition of Hs on or near the nonactive surface on the edge of the detector, where there is a high probability for increased energy loss and to miss α-particle or SF fragments. No definite assignment is possible, for cross section calculations this chain was tentatively attributed to ^{269}Hs.

In chain No. 20, an α-SF correlation was observed in Det. 16. Due to the observation

of an 9.22 MeV α-particle in Det. 11 occurring 12 s earlier, this event is tentatively assigned to a decay of ^{269}Hs assuming that the recoil nucleus ^{265}Sg has been ejected into the fast flowing carrier gas and deposited about 5 cm downstream. Because of low background counting rate, the probability that the first α-particle is not correlated to the following α-SF chain is negligible.

4.1.5   Decay properties of ^{269,270,271}Hs and their daughters

Decay properties calculated from the decay chains observed in both experimental campaigns are summarized in Table 4.3 along with the decay properties derived from previous experiments. Uncertainties correspond to 68 % confidence level. A compilation of decay properties is depicted in Figure 5.1. The half-lives of Hs nuclei are calculated from Q_α values using a phenomenological formula, proposed by Parkhomenko and Sobiczewski (equation (1.4)) [32].
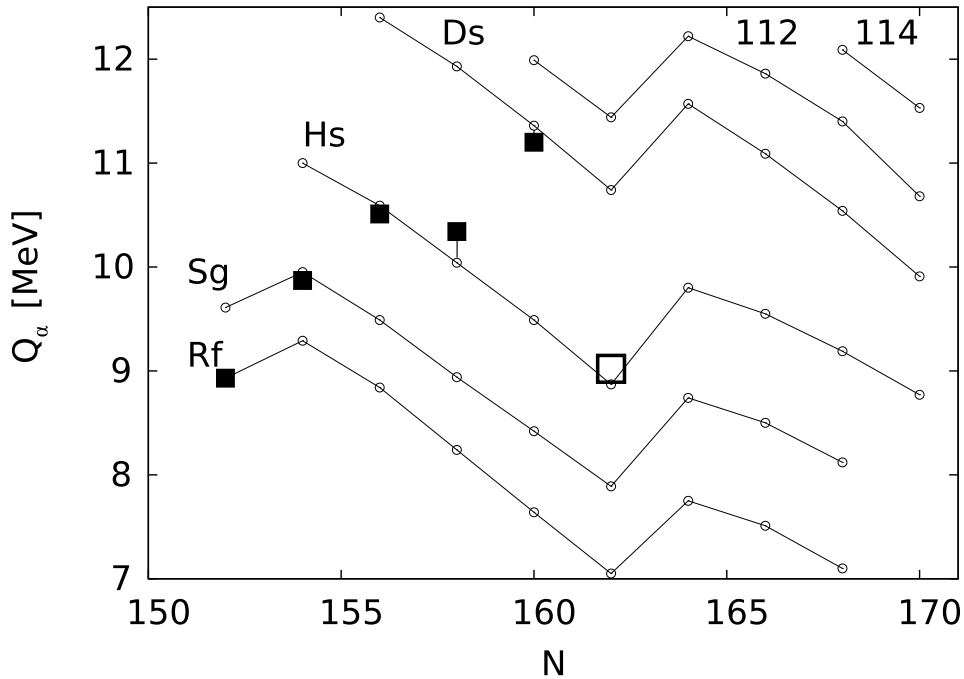
Figure 4.1: Comparison of Q_α values from theoretical calculations [33, 34] and experimental data [35, 36, 37] for even-even nuclei. The Q_α value obtained in this work for ^{270}Hs is depicted with an open square.

For ^{269}Hs and ^{265}Sg the half-lives and the measured α-energies are in good agreement with theoretical predictions [33] and are consistent with results of previous experiments,

Nuclide	Data from previous exp.			Data from TUM Hs chem. exp.		
	Dec. mode, branching[a]	$T_{1/2}$	E_α [MeV]	Dec. mode, branching[a]	$T_{1/2}$	E_α [MeV]
^{269}Hs	α	9.7 s	9.23	α		9.13 ± 0.05
			9.18			8.95 ± 0.05
^{270}Hs	α	~ 3.6 s	9.16	α	~ 23.0 s^b	8.88 ± 0.05
^{271}Hs				α		9.30 ± 0.04
						9.13 ± 0.05
^{265}Sg	α	8 s	8.84	α	$15.3^{+7.1}_{-3.7}$ s	8.69 ± 0.04
			8.76			
			8.94			
			8.69			
^{266}Sg	α	18.8 s	8.77	SF	359^{+248}_{-104} ms	
			8.52			
^{267}Sg				α/SF: 0.17/0.83	$84.3^{+58.1}_{-24.2}$ s	8.20 ± 0.03
^{261b}Rf	α/SF: 0.60/0.40	5 s	8.52	α/SF: 0.09/0.91	$2.5^{+1.1}_{-0.6}$ s	8.51 ± 0.03
^{261a}Rf	α	78 s	8.28	α	22^{+106}_{-10} s^c	8.29 ± 0.03
^{263}Rf	SF	11 m		SF	$8.3^{+39.8}_{-3.8}$ s	

^{a}Branching is not shown, if only one decay mode was observed.
^{b}Half-life calculated from the measured E_α values using phenomenological formula (formula 1.4) [32]
^{c}Derived from 1 event, in agreement with known $T_{1/2} = 78$ s [57,58].

Table 4.3: Decay properties derived from the decay chains detected in TUM experiments on Hs chemistry in comparison with previously known experimental decay properties.

where the decay of ^{269}Hs was observed[2, 3, 40, 41]. Decay properties of the even-even nuclei ^{270}Hs and ^{266}Sg have been unambiguously established for the first time. The α-decay energy of doubly-magic ^{270}Hs is in good agreement with theoretical calculations, which take into account shell stabilization of deformed nuclei. ^{270}Hs is the first experimentally observed even-even nucleus on the predicted $N = 162$ neutron shell. Our experimental data provide an important reference point for theoretical models and clearly show the enhanced nuclear stability at $N = 162$.

In Figure 4.1, calculated α-decay energies (Q_α) of even-even nuclei[33, 34] are plotted along with experimentally measured values [35, 36, 37]. The increased stability leads to local minima at the $N = 162$ neutron shell and a large difference in Q_α values between Ds and Hs isotones. The Q_α of ^{270}Hs, measured for the first time in the TUM Hs chemistry experiments is shown in Figure 4.1 as an open square.

The decay of ^{271}Hs was observed for the first time. The α-particle energy from the decay of ^{271}Hs is higher than from ^{270}Hs, demonstrating the stabilizing effect of the closed shell at $N = 162$. Two α-particle energies were measured, in agreement with the expectation of a complicated scheme of energy levels for decay of this nucleus. Because no definite statement on the energy of the α-decay from the ground state of ^{271}Hs to the ground state of ^{267}Sg can be made, the half-live of ^{271}Hs can be only estimated to ~ 10 s. A relatively long half-life was measured for ^{267}Sg, which is consistent with the observed low α-particle energy, causing α/SF branching in this nucleus.

4.2   Excitation functions of the 3–5n evaporation channels in the fusion reaction ^{26}Mg + ^{248}Cm

Based on the assignment of 26 detected decay chains, the production cross sections for the 3, 4 and 5n evaporation channels of the reaction ^{248}Cm(^{26}Mg, xn)$^{274-\text{x}}$Hs were evaluated for five beam energies. A comparison of the measured cross sections with the values of the HIVAP calculation, using the set of parameters from [49], is shown in Fig. 4.2. Measured cross sections at sub-barrier energies (below the Bass barrier [43] according to a one-dimensional fusion model) are comparable with those, measured at higher energies and suppression of the 3n channel is not evident at sub-barrier energies. This experimental observation indicates, that the real fusion barrier lies lower, or that a multi-dimensional fusion model has to be used. Several theoretical calculations

predicting a significant enhancement of sub-barrier fusion appeared recently [44, 88, 89]. The observed sub-barrier fusion cross sections can be explained by taking into account the deformation of the actinide target nucleus [90]. When the projectile hits the polar side of the deformed target nucleus, a distant configuration is achieved. This lowers the Coulomb barrier, allowing the capture of the projectile nucleus even at sub-barrier energies. A large enhancement of the sub-barrier capture cross sections results, although this is partially compensated by the smaller fusion probability in the case of the distant configuration. The sub-barrier fusion enhancement due to "orientation-effects" was observed in the reactions of ^{16}O and ^{30}Si with ^{238}U targets [91, 92]. Due to the comparable deformation of ^{248}Cm and ^{238}U [27], similar effects are expected also in the case of the reaction ^{26}Mg + ^{248}Cm. The sub-barrier fusion enhancement, demonstrated in our experiment by the observation of the $3n$ channel with a cross section at the same level as the $4n$ and $5n$ channel cross sections, should become even more important in the fusion reactions towards the synthesis of even heavier SHE, because the 4 and $5n$ evaporation channels are more suppressed due to the competition with fission. This opens prospects for the search for the $3n$ evaporation channel products in nuclear reactions with actinide targets, induced with neutron rich projectiles such as ^{18}O, ^{22}Ne, ^{26}Mg, ^{30}Si, ^{36}S. More neutron-rich super-heavy isotopes can be accessible taking advantage of the lowering of the Coulomb barrier in the sub-barrier energy region (or tip collisions) when actinide nuclei are bombarded by rather light of medium-mass projectiles.

4.3   Adsorption enthalpy of HsO$_4$ on Al$_2$O$_3$ and Au surfaces

The distribution of detected Hs and Os decays along the detector channel is depicted in Figure 4.3. The surface of the PIPS diodes, where the activity is adsorbed, was covered with a gold layer in the first experiment and with an oxidized aluminum layer in the second experiment. However, no difference in adsorption positions caused by the two different surfaces was observed. The adsorption enthalpy (ΔH_{ads}) of the compound on the stationary phase is extracted from the measured deposition distribution by using Monte Carlo simulations. These are based on a model of mobile adsorption of single molecules as they move along the column under real experimental conditions [93]. The only free parameter in the simulations is ΔH_{ads}, the half-life of Hs isotopes was estimated as 10 seconds. The best reproduction of the experimental data by the Monte Carlo sim-
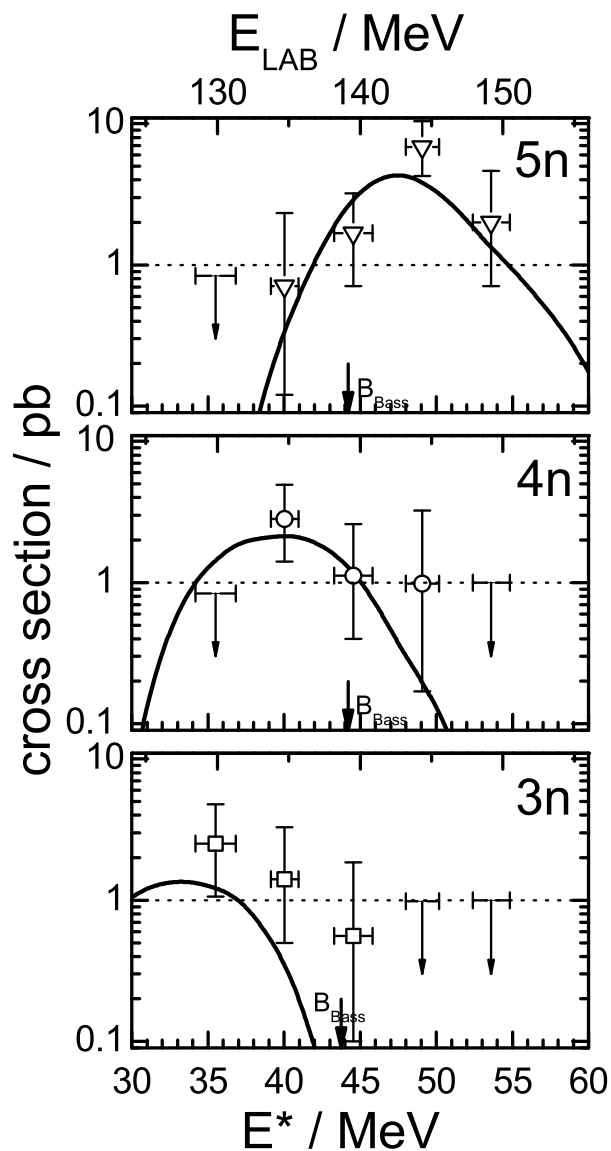
Figure 4.2: Comparison of production cross sections measured for the reaction ^{248}Cm(^{26}Mg,3-5n)$^{269-271}$Hs in [78] and this work along with excitation functions calculated with HIVAP [49]. Cross section limits are indicated by arrows. Error-bars correspond to 68 % confidence level. The location of the Bass barrier [43] is indicated. The most likely attribution was used in case of ambiguously attributed chains. The cross section values changed within the error bars when an alternative attribution was applied.

ulation is achieved at $\Delta H_{ads} = -51$ kJmol^{-1} for HsO$_4$ and $\Delta H_{ads} = -42$ kJmol^{-1} for ^{172}OsO$_4$. Because of the high flow rates in the detector channel in our experiment, the distance between two interactions of volatile species with the wall can be several cm, according to the Monte Carlo simulation. This negatively influences the width of the deposition distribution and consequently the uncertainty of the adsorption enthalpy. The adsorption enthalpy of HsO$_4$ deduced from the TUM chemistry experiment is $\Delta H_{ads} = -51 \pm 5$ kJmol^{-1}. The adsorption enthalpy agrees with the one evaluated in ref. [2] for adsorption on silicon nitride surface (ΔH_{ads}(HsO$_4$) $= -46 \pm 2$ kJmol^{-1} and ΔH_{ads}(OsO$_4$) $= -39 \pm 1$ kJmol^{-1}) within 1σ confidence level. No differences between HsO$_4$ and OsO$_4$ adsorption enthalpy values on Al$_2$O$_3$, gold or silicon nitride surfaces were measured. Hence, it can be deduced, that the HsO$_4$ and OsO$_4$ molecules are interacting only via van der Waals' forces with these surfaces and do not undergo chemisorption.
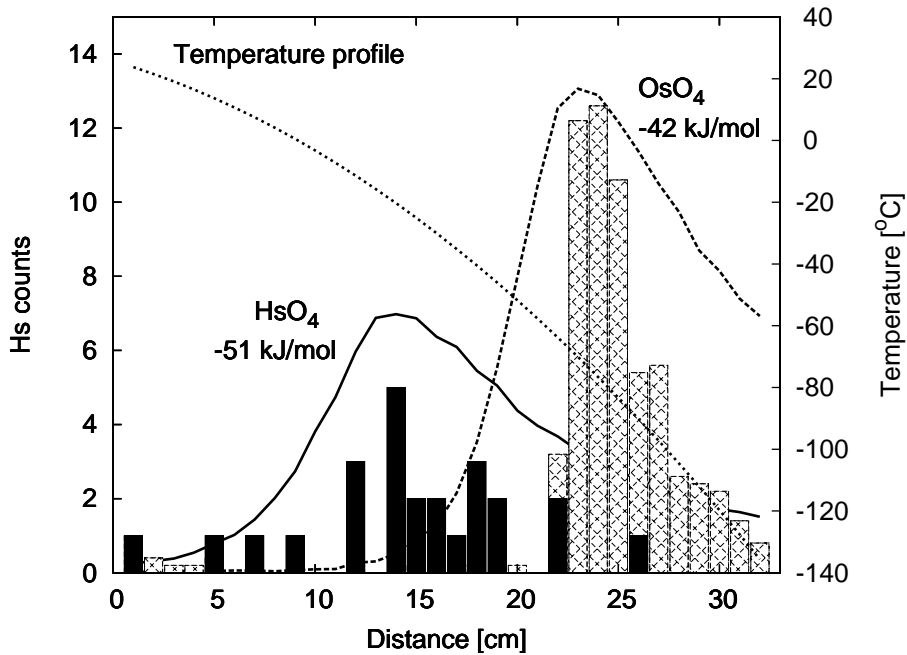
Figure 4.3: Adsorption positions of $^{269-271}$HsO$_4$ and ^{172}OsO$_4$ in the detector channel and comparison with Monte Carlo simulation. OsO$_4$ counts and calculated curves are given in arbitrary units. The temperature profile along the detector channel is shown.

4.4 Results of the experiment on the fusion reaction ^{25}Mg + ^{248}Cm

The laboratory-frame beam energy of 140 MeV in the center of the target was used, for which HIVAP [49] predicts the maximum cross section of 1.3 pb for ^{268}Hs in the $5n$ evaporation channel and 0.4 pb is expected for ^{269}Hs in the $4n$ channel. No correlated events were detected, which could be attributed to the decay of ^{268}Hs or ^{269}Hs. The yield of short-lived α-decaying Os isotopes was monitored during the course of the experiment to ensure, that all experimental conditions are optimized for HsO_4 synthesis and detection. The overall efficiency to detect 9.7 s-isotope ^{269}Hs is 55 % (see Chapter 3), resulting in a one event production cross section limit of 0.4 pb (63.2% c.l. [94]). The so far unknown nuclide ^{268}Hs is expected to decay by α-particle emission, with a half-life 0.1–1 s [19, 28, 38, 39] to 37-ms spontaneously fissioning ^{264}Sg [95]. Because the half-life of ^{268}Hs is comparable with the overall transport time, the overall efficiency to detect ^{268}Hs is a function of the half-life. A mean transport time of ~ 1.4 s was calculated from measurements with short-lived α-decaying Os isotopes. From the known mean transport time a one-event cross section limit for ^{268}Hs was calculated as a function of its half-life, see Figure 4.4. The one event cross section limit of 1 picobarn (63.2% c.l.) has been reached for Hs isotopes with an assumed half-life of one second in this experiment. The experimental sensitivity just reached the cross section values predicted by the HIVAP code [49] for the $4n$ and $5n$ evaporation channels in the reaction ^{25}Mg + ^{248}Cm and no Hs decay was observed.
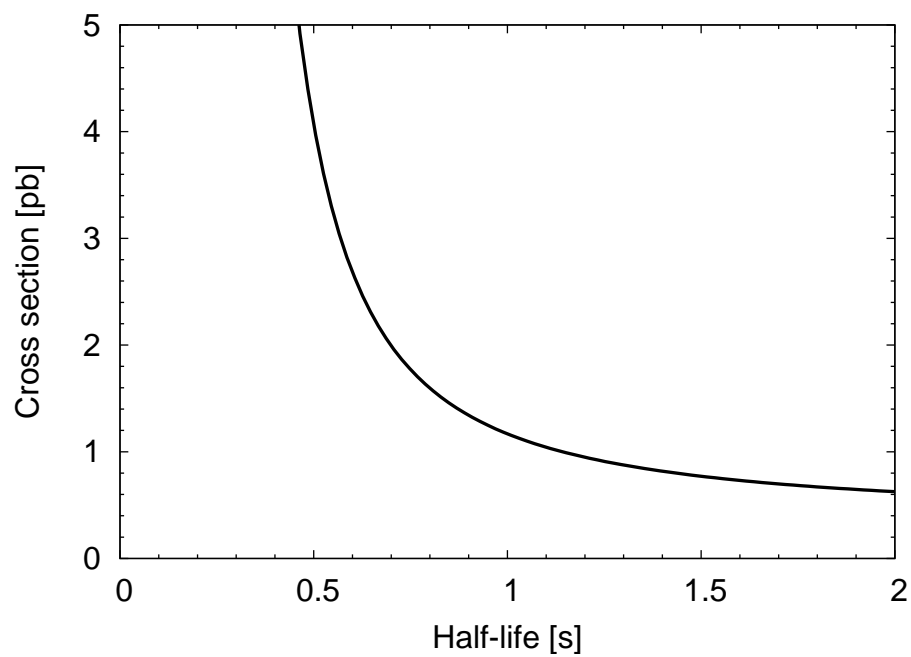
Figure 4.4: One event cross section limit for ^{268}Hs created in the $5n$ evaporation channel in the fusion reaction ^{25}Mg + ^{248}Cm at the beam energy of $E_{LAB} = 140$ MeV. The cross section limit is shown as a function of the half-life of ^{268}Hs, which is unknown.

Chapter 5

Conclusions and outlook

"Experimental confirmation of a prediction is merely a measurement. An experiment disproving a prediction is a discovery."
— Enrico Fermi (1901–1954)

The goal of the research conducted in the frame of this thesis was to investigate the decay properties of the nuclides $^{269-271}$Hs and their daughters using an improved chemical separation and detection system. This goal was accomplished, as these nuclides were successfully synthesized in the nuclear fusion reaction ^{248}Cm(^{26}Mg, xn)$^{274-x}$Hs and detected in the detection system COMPACT and unambiguously identified. An overall efficiency of 55% for the chemical separation and the detection of of Hs decay was reached, better than the efficiency of a kinematic separator for this reaction. This allowed a systematical investigation of the decay properties of Hs nuclei with reasonable statistics, while maximum production cross section of the nuclear reaction ^{26}Mg + ^{248}Cm reaches only a few picobarns. During two experiments, altogether 26 genetically linked nuclear decay chains originating from Hs nuclei have been observed. The known decay chain of ^{269}Hs, the 5n evaporation product, serves as an anchor point, thus allowing the unambiguous assignment of the observed decay chains to the 5n, 4n, and 3n channels, respectively. Decay properties calculated from the decay chains observed in both experiments are summarized in Table 4.3.

The established decay properties bring new information on the decay properties of the involved nuclei, including those, detected in previous experiments. The existence of two isomeric states of ^{261}Rf is confirmed, necessitate to reconsider the decay chain

attributions in previous experiments [56, 60, 3, 2]. Our findings are in contradiction to conclusions from these experiments, but an alternative explanation of the previously detected decay properties is presented. Most likely the nuclides ^{270}Hs and ^{266}Sg were not observed in previous experiments and the decay chains attributed to these nuclides originated from ^{269}Hs and ^{265}Sg, respectively. In our experiments, the decay of ^{270}Hs, as well as ^{271}Hs were measured for the first time. The compiled form of decay properties adopted after the TUM chemistry experiments of Hs chemistry is shown in Figure 5.1.
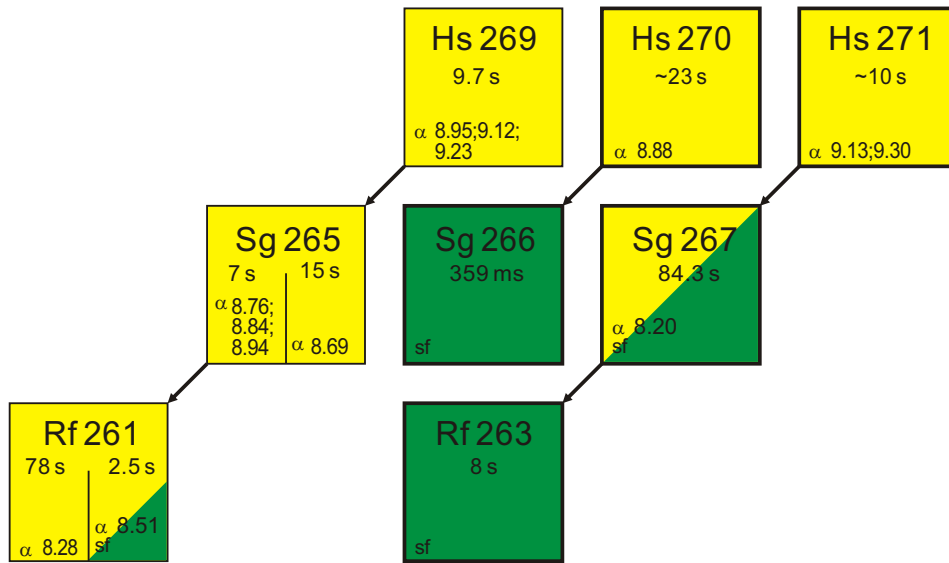
Figure 5.1: Decay properties of nuclei, determined from TUM chemistry experiments of Hs chemistry. Five new nuclides were measured, including the doubly magic nuclide ^{270}Hs.

Decay properties of the even-even nuclei ^{270}Hs and ^{266}Sg have been established. The α-decay energy of doubly-magic ^{270}Hs is in good agreement with theoretical calculations, which take into account shell stabilization of deformed nuclei. ^{270}Hs is therefore the next doubly magic nucleus after the well known ^{208}Pb and the first experimentally observed even-even nucleus on the predicted $N = 162$ neutron shell. Our experimental data provide an important reference point for theoretical models and clearly show the enhanced nuclear stability at $N = 162$.

Decay properties of the even-odd nuclei ^{271}Hs and ^{267}Sg are in good agreement with theoretical predictions. The measured α-decay energy of ^{271}Hs is higher than in the case of ^{270}Hs, supporting the attribution of shell closure to $N = 162$.

The measurement of the production cross sections of the reaction ^{248}Cm(^{26}Mg,xn)$^{274-x}$Hs at five beam energies allowed the evaluation of excitation functions for the 3–5n evap-

oration channels. This measurement is unique, as only a few experimental data on fusion-neutron-evaporation excitation functions, in reactions producing SHE with cross sections at a level of one picobarn, are available so far. The experimental points in this mass region are important for comparison of different theoretical models of fusion reactions. Without a better understanding of the fusion dynamics, the uncertainties of theoretical predictions of cross sections will remain unsatisfactorily high for the experiment preparation.

The measured maximum of the $3n$ channel cross section is comparable with the maximum of the $4n$ channel. Such a ratio between the $3n$ and the $4n$ channel is surprising, as the $3n$ channel is believed to be significantly suppressed in hot fusion reactions. Donets [96] reported two orders of magnitude smaller cross section of the $3n$ channel than that of the $4n$ channel in the reaction ^{18}O + ^{238}U in the year 1966 and interpreted it as "vanishing of the $3n$ channel". Because of this finding, no search for the $3n$ channel products was carried out in experiments on hot fusion reactions, although some models predicted sizable cross sections at sub-barrier energies for the $3n$ channel.

Several theoretical calculations predicting a significant enhancement of sub-barrier fusion cross sections appeared recently [89, 88, 97]. The observed sub-barrier fusion cross sections can be explained, taking into account the deformation of the actinide target nucleus [90]. For instance the HIVAP code, using the set of parameters from [49], predicts substantial cross sections below the Bass barrier [43] for fusion-evaporation reactions with actinide targets. The values of the HIVAP calculation for the reaction ^{248}Cm(^{26}Mg, xn)$^{274-x}$Hs are close to those, observed experimentally (see Figure 4.2). The observed gain in the production cross section at lower excitation energies for this fusion reaction agrees well with those models, which take into account the deformation of the target nucleus. This opens prospects for the search for $3n$ evaporation channel products in nuclear reactions with actinide targets, induced with neutron rich projectiles such as ^{18}O, ^{30}Si, ^{36}S.

In the last experiment performed in the frame of this thesis the detection setup was moved into the irradiation cave and the experiment was carried out with remote control only. This technically demanding experimental setup was designed to reach the shortest possible transport time of the products to the detection system. A transport time of one second or shorter was aimed for, since the goal of this experiment was to detect ^{268}Hs with an expected half-life of 0.1–1 s. The mean transport time of 1.4 s was determined for this improved detection setup in the experiment with short-living Os isotopes. However, the experiment was not sensitive enough to detect Hs decays. An

one event cross section limit of 1 picobarn was reached for Hs isotopes with an assumed half-life of one second in this experiment. From the cross section limit it is clear that the chemical approach allows the investigation of Hs isotopes with a half-life of one second below the one picobarn level.

The adsorption enthalpy of HsO_4 on Au and Al_2O_3 surfaces deduced from the TUM chemistry experiment is $\Delta H_{ads} = -51 \pm 5$ kJmol^{-1}. The adsorption enthalpy agrees with the one evaluated in ref. [2] for adsorption on a silicon nitride surface ($\Delta H_{ads} = -46 \pm 2$ kJmol^{-1}) within an 1σ confidence limit. No difference between the HsO_4 adsorption enthalpy on Al_2O_3, gold or silicon nitride surfaces was found. It can be concluded, that HsO_4 bonds to these surfaces only via van der Waals' forces and does not undergo chemisorption.

The high efficiency of the chemical separation of HsO_4 allows investigation of chemical and physical properties of Hs. The limiting factor to the detection efficiency of chemical experiments is the half-life of the investigated Hs isotopes. Improvements of the experimental setup shortened the transport time to 1.4 s, which allowed examination of Hs isotopes with half-lives of one second or more.

So far, the only hot fusion reactions investigated were ^{25,26}Mg + ^{248}Cm, but Hs nuclei can be produced in various fusion reactions. In ref. [50] a calculation of production cross sections of the fusion reactions ^{26}Mg + ^{248}Cm, ^{30}Si + ^{244}Pu, ^{36}S + ^{238}U, and ^{48}Ca + ^{226}Ra is presented. The $4n$ evaporation channel product of these four fusion reactions is always ^{270}Hs. From Figure 1.14 the most promising reaction is ^{48}Ca + ^{226}Ra with a cross section almost 3 times higher than in the case of the reaction ^{26}Mg + ^{248}Cm, used in our experiment. Cross bombardments would bring new experimental data for comparison of the hot fusion reaction and hence would help in our understanding of the dynamics of hot fusion reactions. The cross section gain of the reaction ^{48}Ca + ^{226}Ra in comparison with the other reactions would help to answer the question of the influence of the projectile magicity (^{48}Ca is doubly magic) and Q-value effect.

In the reactions ^{30}Si + ^{248}Cm, ^{40}Ar + ^{238}U, and ^{48}Ca + ^{230}Th the nuclei $^{275-273}$Ds would be produced in 3–$5n$ channels, which decay via α-decay to $^{271-269}$Hs, nuclei investigated in our experiment. Applying these reactions and chemical separation of Hs would bring new information on the production cross sections of these reactions.

The nuclide ^{271}Hs could be produced in the $1n$ channel of a cold fusion reaction ^{136}Xe + ^{136}Xe. The reaction is particularly interesting, as the $B - Q$ value is smaller than zero according to Audi/Wapstra mass tables [98]. This prohibits CN formation in the

classical model of fusion reaction. In addition, the product $Z_1 \times Z_2$ reaches an extremely high value (2916). This implies, that the fusion reaction should be significantly hindered because of the high probability of re-separation of the incident nuclei. On the other hand, predictions of very high production cross sections also exist (e.g. 170 pb in ref. [99]). In addition the effect of the $B - Q$ parameter discussed in [100] can be investigated.

Both even-even Hs isotopes neighboring to ^{270}Hs are unknown, but their identification would give strong support to the neutron shell closure at $N = 162$. An experiment on the synthesis of ^{268}Hs in the $5n$ channel of the reaction ^{25}Mg + ^{248}Cm did not yield any Hs events, because the experimental sensitivity was too low. However, the irradiation took only 9 days. Repeating the experiment (additional 9 days) would allow reaching a cross section limit of 0.5 pb. The nuclide ^{268}Hs can be alternatively synthesized in the $4n$ channel of the reaction ^{34}S + ^{238}U. The nuclide ^{272}Hs can be produced in the $4n$ channel of the fusion reaction ^{48}Ca + ^{232}Th, after α-decay of ^{276}Ds. However, the predicted half-life for this nuclide ($T_{1/2} = 61$ ms in [38]) makes it not suitable for the investigation with Hs chemistry.

A further development of the detection setup for Hs chemistry is also possible. Covering the detector surface with a thin layer, which is able to reduce the Hs- or Os-tetroxide to nonvolatile mono-, di- or trioxide would allow the construction of a smaller detector system without the need of liquid nitrogen cooling. The smaller dimensions of the detector setup would allow its surrounding by clover gamma detectors and enable measurements of γ-decays of excited isomeric states populated by the α-decays. Detection of α-γ coincidences would give more information on the decay schemes of Hs nuclei and their daughters.

Bibliography

[1] Glenn T. Seaborg and Walter D. Loveland. *The Elements Beyond Uranium*. Wiley, New York, 1990.

[2] C. E. Düllmann, W. Brüchle, R. Dressler, K. Eberhardt, B. Eichler, R. Eichler, H. W. Gäggeler, T. N. Ginter, F. Glaus, K. E. Gregorich, D. C. Hoffman, E. Jäger, D. T. Jost, U. W. Kirbach, D. M. Lee, H. Nitsche, J. B. Patin, V. Pershina, D. Piguet, Z. Qin, M. Schädel, B. Schausten, E. Schimpf, H.-J. Schött, S. Soverna, R. Sudowe, P. Thörle, S. N. Timokhin, N. Trautmann, A. Türler, A. Vahle, G. Wirth, A. B. Yakushev, and P. M. Zielinski. Chemical investigation of hassium (element 108). *Nature*, 418:859–862, August 2002.

[3] A. Türler, C. E. Düllmann, H. W. Gäggeler, U. W. Kirbach, A. B. Yakushev, M. Schädel, W. Brüchle, R. Dressler, K. Eberhardt, B. Eichler, R. Eichler, T. N. Ginter, F. Glaus, K. E. Gregorich, D. C. Hoffman, E. Jäger, D. T. Jost, D. M. Lee, H. Nitsche, J. B. Patin, V. Pershina, D. Piguet, Z. Qin, B. Schausten, E. Schimpf, H.-J. Schött, S. Soverna, R. Sudowe, P. Thörle, S. N. Timokhin, N. Trautmann, A. Vahle, G. Wirth, and P. M. Zielinski. On the decay properties of ^{269}Hs and indications for the new nuclide ^{270}Hs. *European Physical Journal A*, 17:505–508, 2003.

[4] C. F. von Weizsäcker. Zur Theorie der Kernmassen. *Z. Phys. A*, 96(7):431 – 458, 07 1935.

[5] H. A. Bethe and R. F. Bacher. Nuclear Physics A. Stationary States of Nuclei. *Reviews of Modern Physics*, 8:82–229, April 1936.

[6] N. Bohr and J. A. Wheeler. The Mechanism of Nuclear Fission. *Physical Review*, 56:426–450, September 1939.

[7] M. G. Mayer. On Closed Shells in Nuclei. *Physical Review*, 74:235–239, August 1948.

[8] W. D. Myers and W. J. Swiatecki. The Macroscopic Approach to Nuclear Masses and Deformations. *Annual Review of Nuclear and Particle Science*, 32:309–334, 1982.

[9] W. D. Myers. *Droplet Model of Atomic Nuclei.* Plenum, New York, 1977.

[10] M. G. Mayer. Nuclear Configurations in the Spin-Orbit Coupling Model. I. Empirical Evidence. *Physical Review*, 78:16–21, April 1950.

[11] M. G. Mayer. Nuclear Configurations in the Spin-Orbit Coupling Model. II. Theoretical Considerations. *Physical Review*, 78:22–23, April 1950.

[12] M. G. Mayer. On Closed Shells in Nuclei. II. *Physical Review*, 75:1969–1970, June 1949.

[13] O. Haxel, J. H. Jensen, and H. E. Suess. On the "Magic Numbers" in Nuclear Structure. *Physical Review*, 75:1766–1766, June 1949.

[14] V. M. Strutinsky. Shell effects in nuclear masses and deformation energies. *Nuclear Physics A*, 95(952):420–442, April 1967.

[15] V. M. Strutinsky. "Shells" in deformed nuclei. *Nuclear Physics A*, 122(1):1–33, December 1968.

[16] S. G. Nilsson. Binding states of individual nucleons in strongly deformed nuclei. *Kgl. Danske Videnskab. Selskab, Mat.-fys. Medd.*, 29(16), 1955.

[17] J. R. Nix. Calculation of fission barriers for heavy and superheavy nuclei. *Annual Review of Nuclear Science*, 22(1):65–120, 1972.

[18] P. Möller and J. R. Nix. In *Third International Atomic Energy Symposium on Physics and Chemistry of Fission*, volume 1, page 103. Rochester, New York, IAEA, Vienna, 1973. Paper SM-174/202.

[19] P. Möller, J. R. Nix, and K.-L. Kratz. Nuclear Properties for Astrophysical and Radioactive-Ion Beam Applications. *Atomic Data and Nuclear Data Tables*, 66:131, 1997.

[20] Z. Patyk, J. Skalski, A. Sobiczewski, and S. Ćwiok. Potential energy and spontaneous-fission half-lives for heavy and superheavy nuclei. *Nuclear Physics A*, 502:591–600, October 1989.

[21] W. D. Myers and W. J. Swiatecki. Nuclear properties according to the Thomas-Fermi model. *Nuclear Physics A*, 601:141–167, February 1996.

[22] A. Sobiczewski. Structure of Heaviest Nuclei. *Acta Physica Polonica B*, 29:2191, September 1998.

[23] S. Cwiok, J. Dobaczewski, P. H. Heenen, P. Magierski, and W. Nazarewicz. Shell Structure of the Superheavy Elements. *Nucl. Phys.*, A611:211–246, 1996.

[24] K. Rutz, M. Bender, T. Bürvenich, T. Schilling, P.-G. Reinhard, J. A. Maruhn, and W. Greiner. Superheavy nuclei in self-consistent nuclear calculations. *Physical Review C*, 56:238–243, July 1997.

[25] M. Schädel. *The chemistry of the Superheavy Elements*. Kluwer Academic Publishers Dordrecht/Boston/London, 2003.

[26] R. Smolanczuk and A. Sobiczewski. Low energy nuclear dynamics. In Yu. Oganessian, R. Kalpakchieva, and W. von Oertzen, editors, *Proceedings of XV Nuclear Physics Divisional Conference "Low Energy Nuclear Dynamics"*, Singapore, 1995. St. Petersburg, Russia, World Scientific. p. 313.

[27] P. Möller, J. R. Nix, W. D. Myers, and W. J. Swiatecki. Nuclear Ground-State Masses and Deformations. *Atomic Data and Nuclear Data Tables*, 59:185, 1995.

[28] Z. Patyk and A. Sobiczewski. Ground-state properties of the heaviest nuclei analyzed in a multidimensional deformation space. *Nuclear Physics A*, 533:132–152, October 1991.

[29] Michael Bender, Paul-Henri Heenen, and Paul-Gerhard Reinhard. Self-consistent mean-field models for nuclear structure. *Rev. Mod. Phys.*, 75:121–180, 2003.

[30] D. S. Brenner, N. V. Zamfir, and R. F. Casten. Evidence for a spherical subshell at N=164. *Phys. Rev. C*, 50(1):490, July 1994.

[31] A. Sobiczewski, I. Muntian, and Z. Patyk. Problem of "deformed" superheavy nuclei. *Physical Review C*, 63(3):034306, March 2001.

[32] A. Parkhomenko and A. Sobiczewski. Phenomenological Formula for alpha-Decay Half-Lives of Heaviest Nuclei. *Acta Physica Polonica B*, 36:3095, October 2005.

[33] I. Muntian, S. Hofmann, Z. Patyk, and A. Sobiczewski. Properties of Heaviest Nuclei. *Acta Physica Polonica B*, 34:2073, April 2003.

[34] A. Sobiczewski. private communication.

[35] R. B. Firestone and V. S. Shirley. *Table of Isotopes, 2 Volume Set.* Table of Isotopes, 2 Volume Set, by Richard B. Firestone, Virginia S. Shirley (Editor), pp. 3168. ISBN 0-471-33056-6. Wiley-VCH , December 1998., December 1998.

[36] S. Hofmann, F. P. Heßberger, D. Ackermann, S. Antalic, P. Cagarda, S. Ćwiok, B. Kindler, J. Kojouharova, B. Lommel, R. Mann, G. Münzenberg, A. G. Popeko, S. Saro, H. J. Schött, and A. V. Yeremin. The new isotope ^{270}110 and its decay products ^{266}Hs and ^{262}Sg. *European Physical Journal A*, 10:5–10, 2001.

[37] F.P. Hessberger, S. Hofmann, V. Ninov, P. Armbruster, H. Folger, G. Münzenberg, H.J. Schött, A.G. Popeko, A.V. Yeremin, A.N. Andreyev, and S. Saro. Spontaneous fission and alpha-decay properties of neutron deficient isotopes $^{257-253}$104 and ^{258}106. *Zeitschrift fuer Physik A Hadrons and Nuclei*, 359(4):415, 12 1997.

[38] I. Muntian, Z. Patyk, and A. Sobiczewski. Sensitivity of Calculated Properties of Superheavy Nuclei to Various Changes. *Acta Physica Polonica B*, 32:691, March 2001.

[39] D. S. Delion, A. Sandulescu, and W. Greiner. Evidence for α clustering in heavy and superheavy nuclei. *Physical Review C*, 69(4):044318, April 2004.

[40] S. Hofmann, F. P. Heßberger, D. Ackermann, G. Münzenberg, S. Antalic, P. Cagarda, B. Kindler, J. Kojouharova, M. Leino, B. Lommel, R. Mann, A. G. Popeko, S. Reshitko, S. Śaro, J. Uusitalo, and A. V. Yeremin. New results on elements 111 and 112. *European Physical Journal A*, 14:147–157, 2002.

[41] K. Morita, K. Morimoto, D. Kaji, T. Akiyama, S. Goto, H. Haba, E. Ideguchi, H. Koura, H. Kudo, T. Ohnishi, A. Ozawa, T. Suda, K. Sueki, H. Xu, T. Yamaguchi, A. Yoneda, A. Yoshida, and Y.-L. Zhao. Experiments on synthesis of isotope ^{277}112 by ^{208}Pb + ^{70}Zn reaction. *RIKEN Accel. Prog. Rep.*, 38:69, 2005.

[42] W. Loveland. Recent Advances in Understanding Nuclear Reactions. *Journal of Radioanalytical and Nuclear Chemistry*, 243:147–154(8), Jan 2000.

[43] R. Bass. Fusion of heavy nuclei in a classical model. *Nuclear Physics A*, 231:45, 1974.

[44] V.Yu. Denisov. Subbarrier heavy ion fusion enhanced by nucleon transfer. *The European Physical Journal A - Hadrons and Nuclei*, 7(1):87–99, February 2000.

[45] W. J. Swiatecki, K. Siwek-Wilczyńska, and J. Wilczyński. Fusion by diffusion. II. Synthesis of transfermium elements in cold fusion reactions. *Physical Review C*, 71(1):014602, January 2005.

[46] L. Wolfenstein. Conservation of Angular Momentum in the Statistical Theory of Nuclear Reactions. *Phys. Rev.*, 82(5):690, June 1951.

[47] Walter Hauser and Herman Feshbach. The Inelastic Scattering of Neutrons. *Phys. Rev.*, 87(2):366, July 1952.

[48] W. Reisdorf. Analysis of fissionability data at high excitation energies. *Z. Phys. A*, 300(2):227, 06 1981.

[49] W. Reisdorf and M. Schädel. How well do we understand the synthesis of heavy elements by heavy-ion induced fusion? *Z. Phys. A*, 343(1):47, 03 1992.

[50] Z. H. Liu and Jing-Dong Bao. Q-value effects on the production of superheavy nuclei. *Physical Review C (Nuclear Physics)*, 74(5):057602, 2006.

[51] S. Hofmann and G. Münzenberg. The discovery of the heaviest elements. *Rev. Mod. Phys.*, 72:733–767, 2000.

[52] G. Münzenberg. REVIEW ARTICLE: Recent advances in the discovery of transuranium elements. *Reports of Progress in Physics*, 51:57–104, January 1988.

[53] S. Hofmann. New elements - approaching Z=114. *Reports of Progress in Physics*, 61:639–689, June 1998.

[54] G. Münzenberg, P. Armbruster, H. Folger, P. F. Hessberger, S. Hofmann, J. Keller, K. Poppensieker, W. Reisdorf, K. H. Schmidt, H. J. Schött, M. E. Leino, and R. Hingmann. The identification of element 108. *Zeitschrift für Physik A Hadrons and Nuclei*, 317(2):235, 1984.

[55] G. Münzenberg, P. Armbruster, G. Berthes, H. Folger, F. P. Hessberger, S. Hofmann, K. Poppensieker, W. Reisdorf, B. Quint, K. H. Schmidt, H. J. Schött, K. Sümmerer, I. Zychor, M. E. Leino, U. Gollerthan, and E. Hanelt. Evidence for

^{264}108, the heaviest known even-even isotope. *Zeitschrift für Physik A Hadrons and Nuclei*, V324(4):489–490, December 1986.

[56] Y. A. Lazarev, Y. V. Lobanov, Y. T. Oganessian, V. K. Utyonkov, F. S. Abdullin, G. V. Buklanov, B. N. Gikal, S. Iliev, A. N. Mezentsev, A. N. Polyakov, I. M. Sedykh, I. V. Shirokovsky, V. G. Subbotin, A. M. Sukhov, Y. S. Tsyganov, V. E. Zhuchko, R. W. Lougheed, K. J. Moody, J. F. Wild, E. K. Hulet, and J. H. McQuaid. Discovery of enhanced nuclear stability near the deformed shells N=162 and Z=108. *Physical Review Letters*, 73:624–627, August 1994.

[57] B. Kadkhodayan, A. Türler, K. E. Gregorich, P. A. Baisden, K. R. Czerwinski, B. Eichler, H. W. Gäggeler, T. M. Hamilton, D. T. Jost, C. D. Kacher, A. Kovacs, S. A. Kreek, M. R. Lane, M. F. Mohar, M. P. Neu, N. J. Stoyer, E. R. Sylwester, D. M. Lee, M. J. Nurmia, G. T. Seaborg, , and D. C. Hoffman. On-line gas chromatographic studies of chlorides of rutherfordium and homologs Zr and Hf. *Radiochimica Acta*, 72:169, 1996.

[58] A. Ghiorso, M. Nurmia, K. Eskola, and P. Eskola. ^{261}Rf; new isotope of element 104. *Physics Letters B*, 32:95–98, June 1970.

[59] M. R. Lane, K. E. Gregorich, D. M. Lee, M. F. Mohar, M. Hsu, C. D. Kacher, B. Kadkhodayan, M. P. Neu, N. J. Stoyer, E. R. Sylwester, J. C. Yang, and D. C. Hoffman. Spontaneous fission properties of $^{262}_{104}$Rf. *Physical Review C*, 53:2893–2899, June 1996.

[60] A. Türler, R. Dressler, B. Eichler, H. W. Gäggeler, D. T. Jost, M. Schädel, W. Brüchle, K. E. Gregorich, N. Trautmann, and S. Taut. Decay properties of ^{265}Sg (Z=106) and ^{266}Sg (Z=106). *Phys. Rev. C*, 57:1648–1655, April 1998.

[61] Yuri Oganessian. Heaviest nuclei from ^{48}Ca-induced reactions. *Journal of Physics G: Nuclear and Particle Physics*, 34(4):R165–R242, 2007.

[62] R. Eichler, N. V. Aksenov, A. V. Belozerov, G. A. Bozhikov, V. I. Chepigin, S. N. Dmitriev, R. Dressler, H. W. Gäggeler, V. A. Gorshkov, F. Haenssler, M. G. Itkis, A. Laube, V. Ya. Lebedev, O. N. Malyshev, Yu. Ts. Oganessian, O. V. Petrushkin, D. Piguet, P. Rasmussen, S. V. Shishkin, A. V. Shutov, A. I. Svirikhin, E. E. Tereshatov, G. K. Vostokin, M. Wegrzecki, and A. V. Yeremin. Chemical characterization of element 112. *Nature*, 447(7140):72–75, May 2007.

[63] J. P. Desclaux. Relativistic Dirac-Fock Expectation Values for Atoms with Z = 1 to Z = 120. *Atomic Data and Nuclear Data Tables*, 12:311, 1973.

[64] P. Schwerdtfeger and M. Seth. Relativistic effects of the superheavy elements. In *Encyclopedia of Computational Chemistry*, volume 4, pages 2480–2499. Wiley, New York, 1998.

[65] E. Rutherford. Radioactive substance emitted from thorium compounds. *Philosophical Magazine*, 5:1, 1900.

[66] B.L. Zhuikov, H. Kruz, and I. Zvara. Possibilities of chemical identification of short-lived element 108 isotopes. In *Abstract School-Seminar on Heavy Ion Physics 1985*, Report P7-86-322, page 26, JINR, Dubna, 1986.

[67] V.I. Chepigin, B.L. Zhuikov, G.M. Ter-Akopian, and I. Zvara. Search of alpha-active isotopes of element 108 in the reaction ^{249}Cf+^{22}Ne with fast chemical isolation. In *Abstract School-Seminar on Heavy Ion Physics 1985*, Report P7-86-322, page 15. JINR, Dubna, 1986. in Russian.

[68] R. J. Dougan, K. J. Moody, E. K. Hulet, and G. R. Bethune. OSCAR: An apparatus for on-line gas phase separations. Lawrence Livermore National Laboratory, FY87 Annual Report ULAR 10062/87, 1987. pp. 417.

[69] E.K. Hulet, K.J. Moody, R.W. Lougheed, J. F. Wild, R. J. Dougan, and G. R. Bethune. Search for ^{272}109 in a new region of stability. Lawrence Livermore National Laboratory, FY87 Annual Report ULAR 10062/87, 1987. pp. 49.

[70] C. E. Düllmann, B. Eichler, R. Eichler, H. W. Gäggeler, D. T. Jost, D. Piguet, and A. Türler. IVO, a device for In situ Volatilization and On-line detection of products from heavy ion reactions. *Nuclear Instruments and Methods in Physics Research A*, 479:631–639, March 2002.

[71] U. W. Kirbach, C. M. Folden, III, T. N. Ginter, K. E. Gregorich, D. M. Lee, V. Ninov, J. P. Omtvedt, J. B. Patin, N. K. Seward, D. A. Strellis, R. Sudowe, A. Türler, P. A. Wilk, P. M. Zielinski, D. C. Hoffman, and H. Nitsche. The Cryo-Thermochromatographic Separator (CTS): A new rapid separation and α-detection system for on-line chemical studies of highly volatile osmium and hassium (Z=108) tetroxides. *Nuclear Instruments and Methods in Physics Research A*, 484:587–594, May 2002.

[72] C. E. Düllmann. Private communication.

[73] André von Zweidorf, W. Brüchle, S. Bürger, H. Hummrich, Jens Volker Kratz, B. Kuczewski, G. Langrock, U. Rieth, M. Schädel, N. Trautmann, K. Tsukada, and N. Wiehl. Evidence for the formation of sodium hassate(viii). *Radiochimica Acta*, 92:855–861, 2004.

[74] Matthias Schädel. Chemistry of superheavy elements. *Angewandte Chemie International Edition*, 45(3):368–401, 2006.

[75] I. Zvara. Simulation of Thermochromatographic Processes by the Monte Carlo Method. *Radiochimica Acta*, 38:95–101, 1985.

[76] R. Dressler, D. Piguet, A. Serov, and R. Eichler. Transport time optimisation of ivo: Part ii: Model calculations. *PSI Annual Report*, 2006:100, 2006.

[77] K.-H. Schmidt, C.-C. Sahm, K. Pielenz, and H.-G. Clerc. Some remarks on the error analysis in the case of poor statistics. *Zeitschrift für Physik A Hadrons and Nuclei*, 316(1):19, 1984.

[78] J. Dvorak, W. Brüchle, M. Chelnokov, R. Dressler, C. E. Düllmann, K. Eberhardt, V. Gorshkov, E. Jäger, R. Krücken, A. Kuznetsov, Y. Nagame, F. Nebel, Z. Novackova, Z. Qin, M. Schädel, B. Schausten, E. Schimpf, A. Semchenkov, P. Thörle, A. Türler, M. Wegrzecki, B. Wierczinski, A. Yakushev, and A. Yeremin. Doubly Magic Nucleus $^{270}_{108}$Hs$_{162}$. *Physical Review Letters*, 97(24):242501, December 2006.

[79] Z. Ren. Shape coexistence in even-even superheavy nuclei. *Physical Review C*, 65(5):051304, May 2002.

[80] R. Smolanczuk, J. Skalski, and A. Sobiczewski. Spontaneous-fission half-lives of deformed superheavy nuclei. *Physical Review C*, 52:1871–1880, October 1995.

[81] P. Möller and J. R. Nix. Stability of heavy and superheavy elements. *Journal of Physics G Nuclear Physics*, 20:1681–1747, November 1994.

[82] M. Schädel, W. Brüchle, R. Dressler, B. Eichler, H. W. Gäggeler, R. Günther, K. E. Gregorich, D. C. Hoffman, S. Hübener, D. T. Jost, J. V. Kratz, W. Paulus, D. Schumann, S. Timokhin, N. Trautmann, A. Türler, G. Wirth, and A. Yakushev. Chemical properties of element 106 (seaborgium). *Nature*, 388:55, July 1997.

[83] M. Schädel, W. Brüchle, B. Schausten, E. Schimpf, E. Jäger, G. Wirth, R. Günther, J.V. Kratz, W. Paulus, A. Seibert, P. Thörle, N. Trautmann, S. Zauner, D. Schumann, M. Andrassy, R. Misiak, K.E. Gregorich, D.C. Hoffman, D.M. Lee, E.R. Sylwester, Y. Nagame, and Y. Oura. First Aqueous Chemistry with Seaborgium (Element 106). *Radiochimica Acta*, 77:149, 1997.

[84] S. Hübener, S. Taut, A. Vahle, R. Dressler, B. Eichler, H.W. Gäggeler, D.T. Jost, D. Piguet, A. Türler, and W. Brüchle. Physico-chemical characterization of seaborgium as oxide hydroxide. *Radiochimica Acta*, 89:737, 2001.

[85] K. R. Czerwinski. *Studies of fundamental properties of Rutherfordium (element 104) using organic complexing agents.* PhD thesis, UC, Berkeley, Chem. Dept. & LBL, Berkeley, Apr. 1992. LBL-32 233/UC-413.

[86] K. E. Gregorich, C. D. Kacher, M. F. Mohar, D. M. Lee, M. R. Lane, E. Sylwester, D. C. Hoffman, M. Schädel, W. Brüchle, B. Schausten, E. Schimpf, J. V. Kratz, R. Günther, U. Becker, and N. Trautmann. Gsi scientific report. Technical Report 95-1, GSI, 1994. p. 14.

[87] J. V. Kratz, A. Nähler, U. Rieth, A. Kronenberg, B. Kuczewski, E. Strub, W. Brüchle, M. Schädel, B. Schausten, A. Türler, H. W. Gäggeler, D. T. Jost, K. E. Gregorich, H. Nitsche, C. Laue, R. Sudowe, and P. A. Wilk. An EC-branch in the decay of 27-s ^{263}Db: Evidence for the isotope ^{263}Rf. *Radiochimica Acta*, 91:59–62, January 2003.

[88] V. I. Zagrebaev, Y. Aritomo, M. G. Itkis, Y. T. Oganessian, and M. Ohta. Synthesis of superheavy nuclei: How accurately can we describe it and calculate the cross sections? *Physical Review C*, 65(1):014607, January 2002.

[89] S. P. Tretyakova, A. A. Ogloblin, R. N. Sagaidak, S. V. Khlebnikov, and W. Trzaska. Study of nucleus-nucleus potential by combined measurement of deep sub-barrier fusion and cluster decay. *Nuclear Physics A*, 734(Supplement 1):E33–E36, April 2004.

[90] Akira Iwamoto, Peter Moller, J. Rayford Nix, and Hiroyuki Sagawa. Collisions of deformed nuclei: A path to the far side of the superheavy island. *Nuclear Physics A*, 596(2):329–354, January 1996.

[91] K. Nishio, H. Ikezoe, Y. Nagame, M. Asai, K. Tsukada, S. Mitsuoka, K. Tsuruta, K. Satou, C. J. Lin, and T. Ohsawa. Evidence of complete fusion in the sub-barrier o + u reaction. *Phys. Rev. Lett.*, 93(16):162701–4, October 2004.

[92] K. Nishio, S. Hofmann, F. P. Heßberger, D. Ackermann, S. Antalic, V. F. Comas, Z. Gan, S. Heinz, J. A. Heredia, H. Ikezoe, J. Khuyagbaatar, B. Kindler, I. Kojouharov, P. Kuusiniemi, B. Lommel, R. Mann, M. Mazzocco, S. Mitsuoka, Y. Nagame, T. Ohtsuki, A. G. Popeko, S. Saro, H. J. Schött, B. Sulignano, A. Svirikhin, K. Tsukada, K. Tsuruta, and A. V. Yeremin. Measurement of evaporation residue cross-sections of the reaction ^{30}Si + ^{238}U at subbarrier energies. *European Physical Journal A*, 29:281–287, September 2006.

[93] I. Zvara. Thermochromatographic method of separation of chemical elements in nuclear and radiochemistry. *Isotopenpraxis*, 26:251–258, 1990.

[94] K. E. Gregorich. Private communication.

[95] K. E. Gregorich, J. M. Gates, Ch. E. Dullmann, R. Sudowe, S. L. Nelson, M. A. Garcia, I. Dragojevic, C. M. Folden III, S. H. Neumann, D. C. Hoffman, and H. Nitsche. New isotope ^{264}Sg and decay properties of $^{262-264}$Sg. *Physical Review C (Nuclear Physics)*, 74(4):044611, 2006.

[96] E. D. Donets, V. A. Shchegolev, and V. A. Ermakov. Reactions for the evaporation of several neutrons during the irradiation of ^{238}U by accelerated ^{18}O, ^{19}F, and ^{22}Ne ions. *Sov. J. Nucl. Phys.*, 2:723, 1966.

[97] V. Yu. Denisov and S. Hofmann. Formation of superheavy elements in cold fusion reactions. *Phys. Rev. C*, 61(3):034606, February 2000.

[98] G. Audi, A. H. Wapstra, and C. Thibault. The Ame2003 atomic mass evaluation (II). Tables, graphs and references. *Nuclear Physics A*, 729:337–676, December 2003.

[99] Robert Smolanczuk. Formation of superheavy elements in cold fusion reactions. *Phys. Rev. C*, 63(4):044607, Mar 2001.

[100] S. A. Karamian and A. B. Yakushev. Formation of heavy compound nuclei, their survival, and correlation with longtime-scale fission. *Physics of Atomic Nuclei*, 70(2):205–214, February 2007.